UCLA
UCLA Electronic Theses and Dissertations

Title
Synthesis of Silver Sulfide Nanowires and Design of Nanodevices towards Physical Intelligence and Carcinoma Cytology

Permalink
https://escholarship.org/uc/item/32061383

Author
Aguilera, Renato C

Publication Date
2019

Peer reviewed|Thesis/dissertation

eScholarship.org Powered by the California Digital Library
University of California

UNIVERSITY OF CALIFORNIA

Los Angeles

Synthesis of Silver Sulfide Nanowires and Design of Nanodevices towards Physical Intelligence and Carcinoma Cytology

A dissertation submitted in partial satisfaction of the requirements for the degree Doctor of Philosophy in Chemistry

by

Renato Aguilera

2019

© Copyright by

Renato Aguilera

2019

ABSTRACT OF THE DISSERTATION

Synthesis of Silver Sulfide Nanowires and Design of Nanodevices towards Physical Intelligence and Carcinoma Cytology

by

Renato Aguilera

Doctor of Philosophy in Chemistry

University of California, Los Angeles, 2019

Professor James K. Gimzewski, Chair

Presented in this dissertation are designs and characterizations of nanodevices with applications in medical science, information technology, and material design. A broad perspective is taken to facilitate unconventional problem solving and creative thinking in pursuit of producing disruptive technology. At its core, the devices presented here rely on quantum mechanical effects and nanoscale dynamics including the piezoelectric effect, ballistic transport, redox state transitions, and quantum confinement, to name a few. The focus is less on chemical synthesis and more on physical models to manipulate material properties for practical use. In addition, high dimensional materials and complex systems are keenly investigated due to their rich dynamics and indeterminacy. Specifically, Ag_2S atomic switches and conductive polymers

are used in information technology while facile medical devices are developed utilizing nanomaterials for their sensitive but well characterized dynamics. Here, nanotechnology is at forefront of research where the transition from the nanoscale to the mesoscale induces the creative solutions.

Recent advances towards compute-in-memory technology using topological atomic switches allowed for the predictive modeling of traffic flow and fault predicting. The presence of intrinsic nonlinear dynamics in volatile atomic switches enabled for the construction of nonlinear circuits as envisioned for volatile thermodynamic computing. A hardware implemented cognitive computing device using an atomic switch network (ASN) as the processing and memory element is capable of accomplishing tasks such as chaotic time series prediction using < 1 milliWatts of energy per prediction. Tunable volatility in the active layer within a ~10 nm junction switch is paramount and a technique to adaptively control the dynamics through iterative voltammetric control loops is presented.

The dissertation of Renato Aguilera is approved.

William Gelbart

Kang L. Wang

James K. Gimzewski, Committee Chair

University of California, Los Angeles

2019

Table of Contents

LIST OF FIGURES

LIST OF TABLES

ACKNOWLEDGMENTS

This culmination of my work was only possible thanks to all the good people in my life who provided the opportunities to grow. I'd like to thank my teachers and mentors for their inspiration and dedication to empowering future generations—especially the following individuals: Henry O. Sillin, Brian. H. Shieh, Adam Z. Stieg, Paul Wilkinson, Dayan Wickramartne, Greg Pawin, Kang Wang, Masakazu Aono, Tomo Nakayama, and my current advisor James 'Jim' Gimzewski. Jim has been an exemplar scientist during my time at UCLA, a fire that will undoubtedly drive me into the future. To my friends and colleagues, I will always cherish the times we've shared and wish for our mutual success.

Chapter 2 and Chapter 9.2 – Reproduced Figures 1.1 and 9.3 from (Eleanor C. Demis et al 2016 Jpn. J. Appl. Phys. 55 1102B2) with permission from J. Journal of Applied Physics

Chapter 3 – Reproduced Figure 4.1 from (Henry O Sillin et al 2013 Nanotechnology 24 384004) with permission from Nanotechnology Journal

Chapter 5 and 6 – Modified version of Section 2.2 from (Henry O Sillin et al 2013 Nanotechnology 24 384004) with permission from Nanotechnology Journals

Chapter 7 – Reprint Figure 7.1 and modified associated section from (Stieg A.Z. et al. (2019) Self-organization and Emergence of Dynamical Structures in Neuromorphic Atomic Switch Networks. In: Chua L., Sirakoulis G., Adamatzky A. (eds) Handbook of Memristor Networks. Springer, Cham). I credit Dr. Adam Z. Stieg for enhancing the narrative and design of the section. I received permission from Springer Publishing.

Chapter 9 – Reprint Section 3.5 from (Henry O Sillin et al 2013 Nanotechnology 24 384004) with major modifications. I credit H. H. Shieh for the eloquent narrative in the section. I received permission from Nanotechnology Journal.

Chapter 14 – Reprint Figure 14.3 from (Cryst. Growth Des. 2013, 13, 2, 465-469). I credit Dr. Audrius V. Avizienis for his work on synthesizing the nanowires. I have asked permission from ACS Journals.

Chapter 16-19 A modified version of (Sharma, S., Aguilera, R., Rao, J. *et al.* Piezoelectric needle sensor reveals mechanical heterogeneity in human thyroid tissue lesions. *Sci Rep* **9,** 9282 (2019) doi:10.1038/s41598-019-45730-x). I credit Dr Shivani for creating the narrative and basis for the research. I have received permission from Nature journals

VITA

2019	Jim and Barbara Tsay Award, UCLA
2018	Dissertation Year Fellowship Recipient, UCLA
2018	Ecole Polytechnique Fédérale de Lausanne Photothermal AFM Workshop Grant, Lausanne, Switzerland
2017	US-Belgium NSF Workshop on Memristive Networks for Future Computing Innovation Award, Ghent Belgium
2016	Center for NanoScale Science and Technology Conference Best Poster, Adelaide Australia
2015	International Center for Materials Nanoarchitectonics Student Competition Award, Tsukuba Japan
2015	M.S. Chemistry, UCLA
2013	International Center for Materials Nanoarchitectonics Student Competition Award, Tsukuba Japan
2013	Research Associate III, California Nanosystems Institute, Los Angeles
2010	B.S. Physics, University of California Santa Barbara

Selected Publications:

Sillin, H. O.; Aguilera, R.; Shieh, H.-H. H.; Avizienis, A. V.; Aono, M.; Stieg, A. Z.; Gimzewski, J. K., A theoretical and experimental study of neuromorphic atomic switch networks for reservoir computing. Nanotechnology 2013, In press.

Stieg, A. Z.; Avizienis, A. V.; Sillin, H. O.; Aguilera, R.; Shieh, H. H.; Martin-Olmos, C.; Sandouk, E.; Aono, M.; Gimzewski, J. K., Self-organization and Emergence of Dynamical Structures in Neuromorphic Atomic Switch Networks. In Memristor Networks, Springer: Heidelberg, 2014; Vol. XII, p 761.

Aguilera, R; Demis, E; Scharnhorst, K; Stieg; A. Z.; Aono, M.; Gimzewski, J. K, Morphic Atomic Switch Networks for Beyond-Moore Computing Architectures. IEEE IITC Conference Proceedings 2015.

Aguilera, R.; Stieg, A. Z.; Gimzewski, J. K., Short- and Long-term Memory Demonstrated in Atomic Switch Networks Using a Reinforcement Learning Scheme. Neurocomputing 2015.

R. Aguilera, C. Dunham, S Lilak, K Scharnhorst, J. Gimzewski, A Stieg.Atomic Switch Networks for Neuroarchitectonics: Past, Present, Future. In Reservoir Computing: Theory and Physical Implementations, Springer: Heidelberg, 2018.

Renato Aguilera, JianYu Rao, Nagesh Ragavendra, Shivani Sharma, James K. Gimzewski, Medical Implications of Smart Touch Fine Needle Electric (STFN) on Variant Strains Thyroid Carcinoma. Journal of Biomechanics, 2018. In Review

Chapter 1

Overview

A few simple lines on a chalkboard can incite a room into a reverent silence, stop all movement, and its elegance can become part of history as it sheds light on gnostic mysteries using the scientific method. This was the scene in my classroom when we retraced the famous footsteps of Richard Feynman's elementary proof of Kepler's 1st law. Scientific philosophy is the crux of the modern world, owing the Information Technology Era and much of the Green Revolution to its discoveries. From the fabrication of silicon wafers and transistors to energy efficient diodes, chemical sciences produced extraordinary devices for the new age. The prospect of being an engineer of this new age was why I pursued the doctorate of philosophy at the University of California at Los Angeles (UCLA). While pursuing my degree, I decided to specialize in the Chemistry of Nanotechnology as it is able to work in all levels, from nuclear to macroscopic. No other concept thrills me more than applying various techniques of physics to create new materials.

My graduate career has been a platform for converging of multiple fields which offered advance solutions to societal challenges such as poverty, education, and public wellness. The convergence of my past and future fields of study advanced interdisciplinary solutions to grand challenges. The propagation of nanotechnology in the form of electronic devices has allowed networks of people to communicate and react to an ever more dynamic world. The result is a unilateral globalization with problems being resolved using cross-discipline tools. Examples of this within the last decade are the rise in use of biomedical imaging techniques for diagnostics,

Google's biologically inspired neural network algorithm for data mining, and intellectual property driving industry as well as environmental policies persuading voters. This evolution to interdisciplinary solutions is novel and susceptible to mistakes due to miscommunication and misuse of resources. For broad societal solutions utilizing the convergence of technology, healthcare, and industry there must be:

1) Standardization of knowledge using collaborative projects between researchers to facilitate effective communication

2) Open access to institutional resources and facilities to facilitate efficient and in-depth research

3) Educational outreach programs to promote the dissemination of collaborative ideas and philosphies.

From my personal experiences, I have always found society valuing my mixed nature. My Latin and Filipino heritage has often led me to combine Eastern and Western philosophies leading to mixed ideals. Valued and praised for being a convolution of philosophies, my leadership and decisions has allowed me to desegregate my environments by unilateral inclusion of all eccentrics; though, I have been labeled "different." Despite identity ambiguity, it is often the case that a consensus is reached by incorporating mixtures of opinions and goals. Although I have been successful in breaking boundaries, a common difficulty in resolving challenges has been the inability to act cooperatively and unclear communication. The culmination of these lessons leads me to conclude that combining varying views, disciplines, and philosophies will produce unilateral solutions capable of combating poverty. I have attempted to support these goals through hybrid research projects, outreach programs, and collaborative research. I have actively pursued an interdisciplinary career in my graduate program.

1.1 Research Project Overview

1.1.1 Biomimetic Neuromorphic Computing. The bulk of my work endeavored to physically realize brain-like devices utilizing nanotechnology and neuroscience. Nanoscale size limitations and quantum mechanical phenomena enabled the design of fullerenes, low-dimensional materials, and quantum dots, to name a few, for disruptive technological innovations for the past few decades. Utilizing similar phenomena, the designed "atomic switch" derived from crosslinked nanowires introduced an alternative design architecture for Beyond-Moore computing [1-2]. An atomic switch is a 2-terminal metal-insulator-metal device where the insulating region is < 10 nm undergoes transmission tunneling under a voltage bias [3]. Observations of a transition from α-monoclinic to β-argentite phase abruptly increases the tunneling current to an "ON" state. In addition, thermodynamically driven redox reactions modulate the tunneling current due to changes in the surface energy and morphic topology. The simplicity of our processing method enables us to utilize these devices as a Turing B-type unorganized machine for machine learning. This dissertation shows the holistic design, characterization, and implementation of a massively parallel neuromorphic network based on metal chalcogenide atomic switch systems. Our imagined end for neuromorphic hardware go beyond machine learning and encompasses a goal alluded to by Drs. Martin Trefzer and Julian Miller, which is in the scope of artificial life[4]. We should emphasize that we do not aim for artificial life and that our end goal is not machine learning, but neuromorphic hardware and neuromorphic computing which can be described as somewhere between artificial life and reservoir computing/machine learning. Here, we use reservoir computing, a machine learning technique, as a tool to understand our system.

1.1.2 Bioinformatic Medical Devices. Close collaboration with the UCLA Ronald Reagan Medical Center prompted development of smart biopsy needles utilizing the piezoelectric effect and

probe microscopy techniques. Increasing usage of atomic force microscopy for cytological diagnosis and work by Dr. Paul Hansma [5-6] inspired us to apply nanotechnology techniques towards cell type carcinoma diagnosis, specifically human thyroids. The biomechanical properties of tumors are indicators for cancer growth, invasion, and metastasis. While palpable thyroid lesions are common and mostly benign, differentiating malignant nodules can be challenging. We introduce the use of a piezoelectric system called Smart-touch fine needle (or STFN) mounted directly onto conventional biopsy needles, to evaluate abnormal tissues, through quantitative real-time measurements of variations in tissue stiffness as the needle penetrates tissue. Using well-characterized biomaterials of known stiffness and explanted animal tissue models, we first established experimental protocols for STFN measures on biological tissues, as well as optimized device design for high signal-to-noise ratio. Freshly excised patient thyroids with varying fibrotic and malignant potential revealed discrete variations in STFN based tissue stiffness/stiffness heterogeneity and correlated well with final histopathology. Our piezoelectric needle sensor reveals mechanical heterogeneity in thyroid tissue lesions and provides a foundation for the design of hand-held tools for the rapid, mechano-profiling of malignant lesions in vivo while performing fine needle aspiration (FNA).

1.2 Bibliography

[1] ITRS, "International Technology Roadmap for Semiconductors," 2015.

[2] M. M. Waldrop, "The chips are down for Moore's law," *Nature,* vol. 530, pp. 144–147, 2016.

[3] D. B. Strukov*, et al.*, "The missing memristor found," *Nature,* vol. 453, pp. 80-83, 2008.

[4] M. T. T. Kuyucu, J. F. Miller, A. Tyrrell, "On the properties of artificial development and its use in evolvable hardware," presented at the IEEE Symposium onArtificial Life, ALIFE, Nashville, TN, 2009.

[5] e. a. P. Hansma, "The tissue diagnostic instrument," *Rev Sci Instrum,* vol. 80, 2009.

[6] H. G. Hansma*, et al.*, "Progress in Sequencing Deoxyribonucleic-Acid with an Atomic Force Microscope," *Journal of Vacuum Science & Technology B,* vol. 9, pp. 1282-1284, Mar-Apr 1991.

Chapter 2

Neuromorphic Atomic Switch Networks

2.1 Background

Fundamental work by Carver Mead and colleagues [1] in the development of the concept of neuromorphic technology enabled a disruptive paradigm shift in computing technologies. Unlike other conceptions of machine learning, neuromorphic computing attempted to completely emulate neuron functionality within a physically realizable computing hardware. In doing so, the power-efficiency and complexity of neurons can be harnessed without bottlenecking data as in CMOS technology [2]. Additionally, neuron clusters in the brain can recognize patterns and are capable of performing unconventional computing similar to Alan Turing's B-machine [3]. The evolutionary optimization of the brain in both structure and functionality provides an exciting new zeitgeist in a fast stalling technology [4].

Current works using learning dedicated computer hardware provide possible throttling pass the information bottleneck [5-6]. Additionally, developments of beyond-CMOS devices such as magnetic tunneling junctions [7], photoelectronic [8], and memristors [9-11] explored computing architectures outside of typical transistor-based models. In 2000, the International Center for Materials Nanoarchitectonics (MANA) commenced investigation of viable neuromorphic materials utilizing nanowire mechanisms and constraints for material design. Specifically, Professor Masakazu Aono developed the atomic switch as a nano-equivalent neuron operating under quantum mechanical limits at GHz speeds [12-13]. Aono's work on atomic switches developed the underlying principles for integration and development of nanowires for neuromorphic computing elucidating nanowire plasticity and memory capabilities. Single

transistor-like atomic switches were introduced into memory storage devices by Nippon Electric Company [14] using non-dynamic Cu-TiO_2/TaSiO atomic switches for 32 nm CMOS technology. However, the plasticity present in neurological functions are inherently non-static and dynamic [15-16]. Further development of scalable neuromorphic atomic switch devices required a holistic nanoarchitectonic design incorporating dynamic and nonlinear network behaviors.

An emerging mathematical model developed by Leon Chua sought to integrate CMOS technology with nonlinear and chaotic systems [17-18]. In 1971, Chua theorized that, in addition to the 3 fundamental elements in the lumped element circuit model, there was a 4^{th} element he called the *memristor*. Complementing the relations provided by the resistor, capacitor, and inductor, the memristor was able to relate the magnetic flux with electric charge. In order for circuit theory to utilize this 4^{th} element, the model required adaptation of a purely nonlinear circuit theory more akin to Turing's B-machine. Particularly, the model emphasized harnessing emerging behaviors due to coupled circuits similar to the ideals of neuromorphic computing. Here, we present the fabrication of a physical random neural network via growth of memristive atomic switch networks, harnessing phenomenological fractal growth to directly imitate neural evolution for neuromorphic computing.

Unlike conventional neuromorphic platforms which require meticulous design, atomic switch networks (ASN) produced by interconnected nanowires introduce a unique methodology of controlled evolution. Meticulous design of a system required a complete model of understanding such as the CMOS computer architecture modeled by the universal Turing machine. However, it was more practical to develop a scheme of top-down adaptation than by bottom-up selective modification towards the desired function due to hardware limitations. A

combined effort of theoretical predictions and experimental verification is presented here to design a methodology that was physically practical in implementing a computation referred to as *reservoir computing*. A physically realizable recurrent network comprised of gapless-type atomic switches with Ag_2S as the active material previously demonstrated device tenability as functionally compatible neurons [19-21].

An analysis of atomic switch networks at the interface of theory and experiment was accomplished by implementing theoretical paradigms of computation from the perspective of experimental feasibility. Considerations of physical practicality and CMOS compatibility were given priority over an ideal model with microscopic details. Reservoir computing was implemented on the proposed device to accomplish a series of error checking parity tasks and activation control to assess its computational capability. We proposed to answer the following questions:

1. What is the relationship between the dynamical properties of a complex system and its computational capability as a reservoir?
2. How do these dynamical properties emerge in macroscopic tools available to an experimentalist?

2.2 The Atomic Switch

Atomic switches were a class of devices that enabled the use of quantum tunneling for signal transduction. The first experiment to measure the transition from an electron quantum tunneling to single point contact regime was reported in 1987 using a scanning tunneling microscope (STM) in ultra-high-vacuum (UHV) on a silver surface (Möller, 1987). Current-distance characteristics showed an abrupt increase in conductance, $G \sim \frac{e^2}{2h} \approx \frac{1}{13}$ kΩ, at sufficiently

small tip-surface gaps, establishing the quantized unit of conductance. Subsequent theoretical analysis verified that at small gap distance the effective tunnel barrier collapses prior to point contact via ballistic electron injection (Lang, 1986). Later work demonstrated further jumps of $G \sim n\frac{2e^2}{h}$, where $n = 1,2,3$ ..., in the conductance occur as the contact area is increased. Such observations were not limited to STM experiments; even two macroscopic wires brought in contact also displayed this effect, albeit in a less controlled manner. Houten *et al*. provide an excellent review of quantized conduction, which also introduces Landauer's concept of transmission $G = \frac{2e^2}{h}\sum_n t_n$, where the term *t* is the transmission [22].

In 2002, experiments by Terabe *et al.* found that Ag atoms could be transported through a STM tip made of silver coated with silver sulfide and deposited on a surface in a controlled manner [23]. The characteristics of this process also occurred via quantized conduction, however the mechanism involved ion migration under the influence of an electric field, a process called 'electroionics,' meaning that in addition to electron motion, ion motion also occurs simultaneously. Normally, ionic diffusion processes on the macro-scale are considered to be slow, but when they are induced on the nanometer scale, they are actually quite fast and can occur on a (sub-) nanosecond scale depending on the geometry and dimensions of the junction. In 2005, using junctions fabricated using conventional microelectronics, Terabe *et al.* demonstrated atomic switching in silver sulfide junctions with discrete and reversible quantized jumps from n = 1 to 10. This was the birth of the "atomic switch". Since that date, quantized conduction has been observed by a number of researchers in a wide range of materials including sulfide junctions of copper, tungsten sub-oxides as well as various metal-doped polymers.

Aside from the fundamental science of their quantization, the interesting electronic features of atomic switches were hysteresis, on/off conduction ratio, switching speed and volatility characteristics as well as CMOS compatibility because of their potential in digital electronic memory applications. Indeed, NEC recently have incorporated atomic switch technology into field programmable gate arrays (FPGAs) [14, 24] where a reduction in device footprint, speed and energy consumption was achieved by replacing certain memory tasks, normally using transistors, into the circuitry.

Additional atomic switch functionality was reported in 2011 when studying switching near-threshold conditions [25-26]. It was found that atomic switches have an on-off memorization property of past switching events. For instance if switching is performed infrequently, the switches remain in the on-state only briefly whereas if frequent switching events are made in rapid succession then the on-state persists for a longer time. A series of careful experiments were able to relate these physical observations to a psychological model of learning called the Akinson-Schriffin multi-store model [27]. The essence of the model involves sensory memory (SM), short-term memory (STM) and long-term memory (LTM). New information arrives to the brain as sensory memory and that information was passed to short-term memory. In the absence of similar information it was forgotten. However, if the process was repeated many times, the information was moved into long-term memory. In terms of bio-inspiration, the operational characteristics of the atomic switch under threshold switching were also related to characteristics of biological synapses. The atomic switch therefore has also been called a synthetic synapse where memory was represented by conduction state.

The next step in creating a 'brain inspired" device was the fabrication of networks of synthetic synapses (Atomic Switches). Taking the neocortex as a biologically inspiration, self-

assembly was used to incorporate atomic switches into a dense dendritic tangle of silver nanowires resulting in a density of ~10^8 connections/cm^2 [28]. In response to electrical inputs, which inject energy into the network, these networks exhibited self-organization and critical power-law dynamics and spatio-temporal nonlinear outputs at multiple electrodes.

2.3 Neuromorphic Atomic Switch Networks

The clear desire for neuromorphic architectures has led to further investigations and developments of different synthetic synapse models. Establishing specific connections between patterns of electrical activity and brain function was a difficult task that requires studying general features of neuronal structure in order to determine the essential properties required to construct a device capable of learning in a physical sense. These features are believed to include at least synaptic plasticity, allowing physical reconfiguration of the network to enable functional differentiation, and the development of hierarchical structures which all possess correlated memory distributed throughout the dynamically coupled synapses. Therefore, learning and computational capacity in the brain are connected to dynamic activity and functional connectivity. Specifically, a near-critical or "edge of chaos" operational [29] regime has been associated with the fast, correlated response to stimulation necessary for computation and learning. Developing computational machinery whose operation results from intrinsic critical dynamics was a complex task; with Atomic Switch Network (ASN) devices demonstrated such functionality.

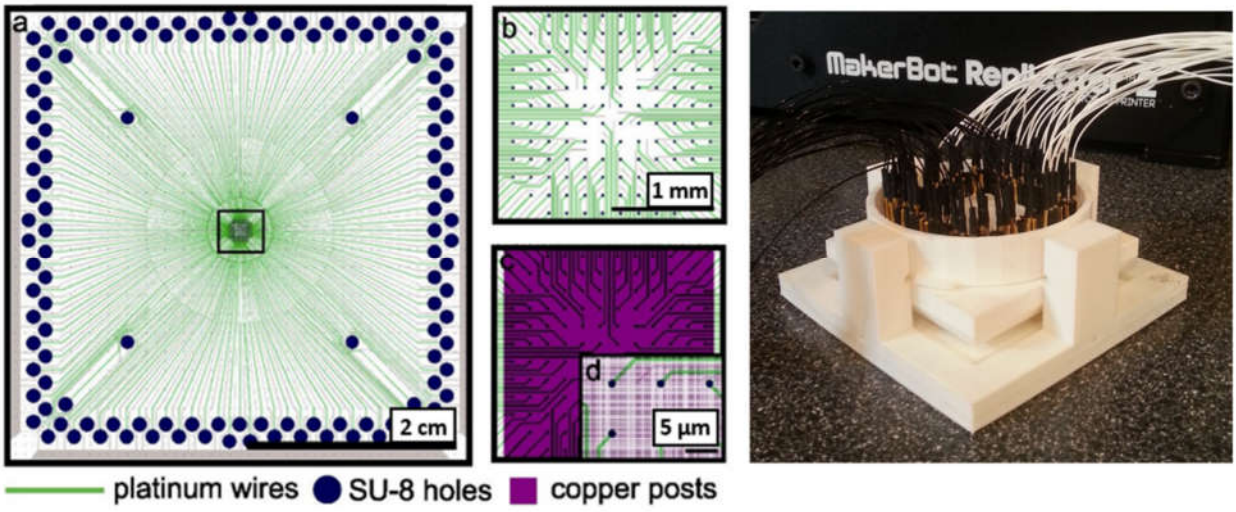

Figure 1.1 Network diagram and analogue interface. A circuit schematic is shown in **a** showing the platinum circuit (green) and readout PC interface (blue). The silver network was placed in the central region (boxed) and a closer inspection of the region wiring is shown in **b**. Pre-patterned posts were lithographically placed within the boxed region in **c** ready for network growth. The device was interfaced to a National Instruments PXI—e using a custom device housing.

Utilizing the theoretical concepts presented in the previous section, we designed a neuromorphic device (Figure 1.1) by incorporating atomic switches in a highly recursive interconnected network. The work of Aono [23, 25-26] established the fundamental principles and design of atomic switches. Observation of plasticity and information retention in atomic switches enabled us to successfully implement them in neuromorphic hardware for reservoir computing [20-21]. A number of materials were available and various functionalities may be tuned depending on the active material. Here, metal-chalcogenides were chosen due to their ready integration into CMOS technology and capability for spontaneous fractal growth.

2.4 Bibliography

[1] C. Mead, "Neuromorphic electronic systems," in *IEEE*, 1990.

[2] J. W. Backus, "Can programming be liberated from the von Neumann style?: a functional style and its algebra of programs," *Communications of the ACM,* vol. 21, 1978.

[3] A. M. Turing, "Computing Machinery and Intelligence," *Mind,* vol. 59, pp. 433-460, 1950.

[4] M. M. Waldrop, "The chips are down for Moore's law," *Nature,* vol. 530, pp. 144–147, 2016.

[5] C. P. H. Husband, S. M.; Daniels, J. S.; Tour, J. M., "Logic and Memory with Nanocell Circuits," *IEEE Transactions on Electron Devices,* vol. 50, 2003.

[6] L. C. James M. Tour, David P. Nackashi,Yuxing Yao,Austen K. Flatt, Sarah K. St. Angelo,Thomas E. Mallouk, andPaul D. Franzon, "NanoCell Electronic Memories," *J. Am. Chem. Soc.,* vol. 125, pp. 13279–13283, 2003.

[7] e. a. Taishi Furuta, "Macromagnetic Simulation for Reservoir Computing Utilizing Spin Dynamics in Magnetic Tunnel Junctions," *Phys. Rev. Applied* vol. 10, 2018.

[8] M. B. Michiel Hermans, Thomas Van Vaerenbergh, Joni Dambre & Peter Bienstman, "Trainable hardware for dynamical computing using error backpropagation through physical media," *NATURE COMMUNICATIONS,* vol. 6, 2015.

[9] R. T. a. L. C. Alon Ascoli, *Continuous and Differentiable Approximation of a TaO Memristor Model for Robust Numerical Simulations* vol. 191: Springer Proceedings in Physics 2017.

[10] F. C. Chao Du, Mohammed A. Zidan, Wen Ma, Seung Hwan Lee & Wei D. Lu, "Reservoir computing using dynamic memristors for temporal information processing," *Nature Communications,* vol. 8, 2017.

[11] S. G. S. Strukov D B, Stewart D R and Williams R S, "The missing memristor found," *Nature,* vol. 453, pp. 80-83, 2008.

[12] M. O. Takashi Tsuchiya, Tohru Higuchi, Kazuya Terabe, and Masakazu Aono, "Effect of Ionic Conductivity on Response Speed of SrTiO3‑Based AllSolid-State Electric-Double-Layer Transistor," *ACS Appl. Mater. Interfaces,* vol. 7, 2015.

[13] T. H. Tohru Tsuruoka, Kazuya Terabe, & Masakazu Aono, "Operating mechanism and resistive switching characteristics of two- and three-terminal atomic switches using a thin metal oxide layer," *J Electroceram,* vol. 39, 2017.

[14] NEC. (2009, NEC Integrates NanoBridge in the Cu Interconnects of Si LSI. Available: https://phys.org/news/2009-12-nec-nanobridge-cu-interconnects-si.html

[15] B. S. a. R. L. Lars Büsing, "Connectivity, Dynamics, and Memory in Reservoir Computing with Binary and Analog Neurons," *Neural Computation,* vol. 22, pp. 1272-1311, 2010.

[16] H. J. Mantas Lukoševičius, "Reservoir computing approaches to recurrent neural network training," *Computer Science Review,* vol. 3, pp. 127-149, 2009.

[17] L. O. Chua, "Device Modeling Via Basic Nonlinear Circuit Elements," *IEEE Transactions on Circuits and Systems* vol. 27, 1980.

[18] M. P. K. a. L. O.Chua, "Neural Networks for Nonlinear Programming," *IEEE Transactions Circuits and Systems,* vol. 35, 1988.

[19] E. C. A. Demis, R.; Sillin, H. O.; Scharnhorst, K.; Sandouk, E. J.; Aono, M.; Stieg, A. Z.; Gimzewski, J. K., "Atomic Switch Networks Nanoarchitectonic Design of a Complex System for Natural Computing," *Nanotechnology,* vol. 26, 2015.

[20] R. A. Eleanor C. Demis, Kelsey Scharnhorst, Masakazu Aono, Adam Z. Stieg and James K. Gimzewski, "Nanoarchitectonic atomic switch networks for unconventional computing," *Japanese Journal of Applied Physics,* vol. 55, 2016.

[21] R. A. Henry O Sillin, Hsien-Hang Shieh, Audrius V Avizienis, Masakazu Aono, Adam Z Stieg and James K Gimzewski, "A theoretical and experimental study of neuromorphic atomic switch networks for reservoir computing," *Nanotechnology,* vol. 24, p. 384004, 2013.

[22] C. B. Henk van Houten, "Quantum Point Contacts," *Physics Today,* vol. 49, 1996.

[23] T. N. K Terabe, T Hasegawa, M Aono, "Formation and disappearance of a nanoscale silver cluster realized by solid electrochemical reaction," *Journal of applied physics,* vol. 91, pp. 10110-10114, 2002.

[24] Y. S. Y. F. N. Aramaki, "A parallel ASIC VLSI neurocomputer for a large number of neurons and billion connections per second speed," presented at the IEEE International Joint Conference on Neural Networks, Singapore, 1991.

[25] T. H. Takeo Ohno, Tohru Tsuruoka, Kazuya Terabe, James K Gimzewski, Masakazu Aono, "Short-term plasticity and long-term potentiation mimicked in single inorganic synapses," *Nature materials,* vol. 10, pp. 591-595, 2011.

[26] A. N. Tsuyoshi Hasegawa, Takeo Ohno, Kazuya Terabe, Tohru Tsuruoka, James K. Gimzewski, Masakazu Aono, "Memristive operations demonstrated by gap-type atomic switches," *Applied Physics A,* vol. 102, pp. 811-815, 2011.

[27] R. M. S. R.C.Atkinson, "Human Memory: A Proposed System and its Control Processes," *Psychology of Learning and Motivation,* vol. 2, pp. 89-195, 1968.

[28] C. M.-O. Audrius V. Avizienis, Henry O. Sillin,Masakazu Aono, James K. Gimzewski, and Adam Z. Stieg, "Morphological Transitions from Dendrites to Nanowires in the Electroless Deposition of Silver," *Crystal Growth & Design,* vol. 13, 2013.

[29] C. G. Langton, "Computation at the Edge of Chaos: Phase Transitions and Emergent Computation," *Physica D,* vol. 42, pp. 12-37, 1990.

Chapter 3

Theoretical Constraints and Consideration of Neuromorphic Computing

The concept of neuromorphic hardware as conceived by Carver Mead [1] intended to emulate the problem-solving capability of biology, which has been evolutionary optimized by nature. Observations of DNA folding and editing [2] demonstrated the capabilities of evolutionary algorithms to enable DNA to execute complex protein interaction and regulation. Natural selection has inherently optimized these systems in their task-specific function, thereby minimizing energy, maximizing information transfer, and encoding fault-tolerant and adaptive behaviors [3]. Neuromorphic hardware attempted to adapt this architectural design within the context of circuit theory and analysis. A premier model for computational design was the human-brain, where complex computation such as speech, multisensory control, and chaotic predictions were commonly executed while operating under relatively simple rules.

3.1 Mathematical Formalism of Neural Networks

Fundamentally, the brain utilized synaptically interconnected neurons to transfer and process information. Each neuron operated under the Hebbian fire-diffuse-fire principal [4-5] which activated neurons with a sigmoidal function profile similar to transistors with voltage replacing ions in the latter case. Unlike contemporary digital transistors, each neuron was heavily coupled to other elements behaving effectively as a history-dependent nonlinear device. Circuit network theory has analogous examples of coupled inductive circuits communicating across devices, but such circuits were typically designed to eliminate coupled cross-talk and the overall

circuit was linearized in its functionality. However, simplification of these interactions invariably destroys emergent behaviors observed in complex systems [6-7], which was capable of accomplishing complex computation. Nonlinear circuit design and analytical models by Chua [8-9] attempted to utilize these complex interactions but have limited integration within information technology. Instead, machine learning algorithms were implemented in software which mimics the design and learning rules of biological systems. Here, a combination of machine learning architecture and nonlinear circuit design is briefly presented and discussion was restricted within a feed forward network for brevity; however, a formal and comprehensive discussion has been previously published [10-11].

The neural network machine learning paradigm traditionally attempted to achieve learning by modification of network topology and connectivity via adjustments to neuronal coupling strength. The general architecture of a neural network was designed similar to the human brain - a collection of nodes or neurons interconnected with synapses to other neurons in a hierarchal layered structure [12-17]. Neuronal nodes were typically designed to integrate incoming signals and transform them using a sigmoidal transfer function. The integration was the weighted sum of all signals received by the neuron from a predetermined set of input neurons from the previous layer:

$$I^0(t) = \widehat{N}_0 I^D(t) f^0\left(I^D(t)\right), \tag{3.1}$$

where $I^0(t)$ was a vector with elements of the transduced signal of each neuron in layer 0, $\widehat{N}_0$ was a matrix representing the transformation of the driving signal, $I^D(t)$ the driving signal, and f^0 was a vector whose elements are the transfer functions of each neuron . The neuron activated

according to its designed transfer function, then propagated the signal to its pre-designated output neurons in the next layer, *i.e.* layer 1:

$$I^1(t) = \widehat{N}_1 I^0(t) \equiv f^1\left(\widehat{w}_1 \;\; I^D(t)\right). \tag{3.2}$$

Here, $\bar{w}_i^1$ was the coupling strength between neuron i in layer 1 and all other neurons. This process was repeated from neuron to neuron in a hierarchal structure composed of layers or networks of neurons until it arrives at an output neuron layer, represented by $I^T(t)$, where the user observes and process the final signal $I^F(t)$:

$$I^T(t) = \prod_k^{\forall} \widehat{N}_k I^D(t) \equiv \hat{O}\, I^D(t) \tag{3.3}$$

$$I^F(t) = \widehat{w}_D \;\; I^T(t). \tag{3.4}$$

The operator $\hat{O}$ represented the overall transformation by the network, and $\widehat{w}_D$ was the design matrix in the output layer whose rows were the number of observable parameters and columns were the coupling strength to the sensors. While the above assumed a feed forward architecture, equations (3.3) and onwards may be generalized for any network if one allows $\hat{O}$ to represent any network transformation. Learning was achieved by designing the network connections in such a way that the output signal was transformed into a desired target signal. Each desired computational process corresponded to a desired signal, $I_{desired}^{test}$, for a given input signal, $I^D(t)$, and network transformation, $I^F(t)$. The synaptic strength of individual connections were adjusted in incremental corrective steps according to a learning rule using a training data set until the network's effective function was the desired mathematical operation. Various learning techniques exist and depend on network type, connectivity structure, neuronal transfer function,

I/O implementation, task complexity, and computational constraints [18-21]. Here, we focused on the linear-regression learning rule as it was the typical and simplest learning rule:

$$\widehat{w}_D\widehat{O} = \left(\left[I^T(t)\right]^\dagger \left[I^T(t)\right]\right)^{1} \left[I^T(t)\right]^\dagger I_{desired}^{training}(t). \tag{3.5}$$

The process was done recursively by using a number of controlled training data sets to determine error propagation and correction. Defining a metric for error was nontrivial and clever designs and calculations of error existed that can drastically determine learning performance. However, we focused on the most commonly used and simplest definition of signal error which was the normalized mean squared error (NMSE) and adopted accuracy as a more intuitive measure of performance.

$$error \equiv \frac{E\left[\left(I_{desired}^{test} - I^F(t)\right)^2\right]}{E\left[\left(I_{desired}^{test} - E\left[I_{desired}^{test}\right]\right)^2\right]} \quad ; \quad accuracy \equiv 1 \quad error \tag{3.6}$$

A network's computational capability was nearly defined by its network size, size of $\widehat{O}$, while simultaneously increasing the complexity in learning. Unfortunately, implementing such a model using traditional photolithography manufacturing inevitably approached the Abbe diffraction limit [22], which was incapable of physically addressing elements on similar scale as current software implemented neural networks. Reservoir computing [11, 15] was a distinguished computational model for scalable neuromorphic hardware as it does not require comprehensive control of the network, omitting the $\widehat{O}$ in (3.5). Learning algorithms only required training on the output layer of neurons, $\widehat{w}_D$, while the inner "reservoir" neurons, $\widehat{O}$, are unattended and replaced $I^T(t)$ with $I^F(t)$ in (3.5) [10-11, 15]. Here, we utilized the reservoir computing paradigm as the functional model for computation in our ASN experiments.

3.2 Nonlinear Circuits

Regardless of the network construction or stimulation, a neural network was not capable of performing complex calculations if individual neurons behaved linearly [23]. A brief proof of the desire for nonlinearity was by *contra positive* and to logically investigate the behavior of a network with purely linear elements. We constrained discussion using the above mathematical formalism where systems were represented only by neurons, and any post-processing or contributions from instrumentation were represented as an appropriate neuron layer. Let individual neurons be defined by the gain of an op-amp circuit to simulate linearity, which simply rescales the amplitude of the input signal as in equation (3.7). Suppose the neurons were fully connected to every other neuron by a fully populated network, maximizing the rank of the transformation matrix $\hat{O}$. Inevitably, a linear combination and convolution of such neurons only resulted in a linearly behaving network, regardless of network connectivity:

$$let\ I^T(t) = \hat{O}\ I^D(t) = \hat{\lambda}\ I^D(t), \tag{3.7}$$

$$I^F(t) = \widehat{w}_D \quad I^T(t) = \widehat{w}_D \quad \hat{\lambda}\ I^D(t) = \bar{w}_{Deff} \quad I^D(t), \tag{3.8}$$

where the transformation in equation (3.7) was replaced by a linear function, while the final signal in equation (3.8) was a linear combination of the driving signal with $\bar{w}_{Deff} = \sum_i^N w_{Di}\,\lambda_i$. The above demonstrated linear neurons' limited computational capability and be completely defined by the input signal from equation (3.8), while the design matrix $\bar{w}_{Deff}$ merely scales the input. To enable the network to implement complex computation, a neuronal behavior with nonlinear characteristics and robust mathematical formalism was adopted. Chua's nonlinear circuit analysis [24] introduced the concept of memristive systems as a neuron-like two-terminal element with characteristic nonlinear and memory qualities. The memristor

nonlinearly related the integrated voltage (magnetic flux, φ) with charge and acts similar to a charge dependent resistor:

$$d\varphi = M\, dq \quad or \quad M(q) = \frac{d\varphi}{dt}/\frac{dq}{dt} = V/I. \tag{3.9}$$

The relation was strictly nonlinear and solved differentially, which required holistic circuit analysis when the element was incorporated within a network [25]. A memory attribute was readily illustrated in the memristor's dependency on charge accumulation, which was desirable to any learning system. Discovery of physical memristor devices [26] and complex circuit oscillations depicting chaotic trajectories [27-28] has enabled the construction of nonlinear circuits capable of harnessing emergent chaotic behaviors. Observations of neurons physically adapted to environmental changes through a recurrent feedback mechanism [23] paralleled the oscillatory behavior found in Chua circuits. Likewise, incorporation of a continuous feedback enabled adaptive and responsive computing [29].

3.3 Bibliography

[1] C. Mead, "Neuromorphic electronic systems," in *IEEE*, 1990.

[2] e. a. A. Romero, "Diet Networks: Thin Parameters for Fat Genomics," *arXiv,* 2017.

[3] K.-H. H. a. J.-H. Kim, "Quantum-Inspired Evolutionary Algorithm for a Class of Combinatorial Optimization," *IEEE TRANSACTIONS ON EVOLUTIONARY COMPUTATION,* vol. 6, pp. 580 - 593, 2002.

[4] D. O. Hebb, *Organization of behavior*, 1 ed. New York: Wiley, 1950.

[5] S. C. a. Y. Timofeeva, "Sparks and waves in a stochastic fire-diffuse-fire model of Ca2 release," *PHYSICAL REVIEW E,* vol. 68, 2003.

[6] X. F. W. G. Chen, "Complex networks: small-world, scale-free and beyond," *IEEE Circuits and Systems Magazine,* vol. 3, pp. 6-20, 2003.

[7] C. T. Alireza Goudarzi, Natali Gulbahce, and Thimo Rohlf, "Emergent Criticality through Adaptive Information Processing in Boolean Networks," *PHYSICAL REVIEW LETTERS,* vol. 108, 2012.

[8] R. T. a. L. C. Alon Ascoli, *Continuous and Differentiable Approximation of a TaO Memristor Model for Robust Numerical Simulations* vol. 191: Springer Proceedings in Physics 2017.

[9] C. W. W. a. L. O. Chua, "Synchronization in an Array of Linearly Coupled Dynamical Systems," *IEEE TRANSACTIONS ON CIRCUITS AND SYSTEMS-I FUNDAMENTALTHEORY AND APPLICATION,* vol. 42, 1995.

[10] H. J. Mantas Lukoševičius, "Reservoir computing approaches to recurrent neural network training," *Computer Science Review,* vol. 3, pp. 127-149, 2009.

[11] D. Verstraeten, "Reservoir Computing: computation with dynamical systems," PhD PhD thesis, Electronics and Information Systems, Ghent University, Gent, 2009.

[12] A. M. A. Graves, G. Hinton, "Speech Recognition with Deep Recurrent Neural Networks," *arXiv,* 2013.

[13] I. S. A. Krizhevsky, G. E. Hinton, "Imagenet classification with deep convolutional neural networks," presented at the Advances in neural information processing systems, 2012.

[14] A. Abraham, "Artificial Neural Networks," in *Handbook of Measuring System Design*, P. H. S. a. R. Thorn, Ed., ed: John Wiley & Sons, 2005, pp. 901-908.

[15] D. V. Benjamin Schrauwen, Jan Van Campenhout, "An overview of reservoir computing: theory, applications and implementations," in *15th European Symposium on Artificial Neural Networks*, 2007, pp. 471-482.

[16] M. H. Hassoun, *Fundamentals of Artificial Neural Networks*, 1 ed.: MIT Press, 1995.

[17] J. J. Hopfield, "Artificial neural networks," *IEEE Circuits and Devices Magazine,* vol. 4, pp. 3-10 1988.

[18] B. S. a. R. L. Lars Büsing, "Connectivity, Dynamics, and Memory in Reservoir Computing with Binary and Analog Neurons," *Neural Computation,* vol. 22, pp. 1272-1311, 2010.

[19] E. T. Ariel Haimovici, Pablo Balenzuela, and Dante R. Chialvo, "Brain Organization into Resting State Networks Emerges at Criticality on a Model of the Human Connectome," *Phys. Rev. Lett.,* vol. 110, 2013.

[20] E. S. Nedaaee Oskoee, M, "Electric Currents in Networks of Interconnected Memristors," *Phys. Rev. E,* vol. 83, 2011.

[21] O. Sporns, "Small-world connectivity, motif composition, and complexity of fractal neuronal connections," *Biosystems,* vol. 85, pp. 55-64, 2006.

[22] E. Abbe, *Contributions to the theory of the microscope and the microscopic perception*: Springer, 1873.

[23] J. D. Juan Pablo Carbajal, Michiel Hermans, Benjamin Schrauwen, "Memristor models for machine learning," *Neural Computation,* vol. 27, pp. 725-747, 2015.

[24] M. P. K. a. L. O.Chua, "Neural Networks for Nonlinear Programming," *IEEE Transactions Circuits and Systems,* vol. 35, 1988.

[25] L. O. Chua, "Device Modeling Via Basic Nonlinear Circuit Elements," *IEEE Transactions on Circuits and Systems* vol. 27, 1980.

[26] S. G. S. Strukov D B, Stewart D R and Williams R S, "The missing memristor found," *Nature,* vol. 453, pp. 80-83, 2008.

[27] M. I. a. L. O. CHUA, "MEMRISTOR OSCILLATORS," *International Journal of Bifurcation and Chaos,* vol. 18, 2008.

[28] C. W. W. Leon O. Chua, Anshan Huang, and Guo-Qun Zhong, "A Universal Circuit for Studying and Generating Chaos-Part I: Routes to Chaos," *IEEE TRANSACTIONS ON CIRCUITS AND SYSTEMS-I: FUNDAMENTAL THEORY AND APPLICATIONS,* vol. 40, 1993.

[29] M. B. Michiel Hermans, Thomas Van Vaerenbergh, Joni Dambre & Peter Bienstman, "Trainable hardware for dynamical computing using error backpropagation through physical media," *NATURE COMMUNICATIONS,* vol. 6, 2015.

Chapter 4

Characterization of Nonlinearity

4.1 Power-Law Dynamics

The above mathematical construct illustrated the importance and central role of the network connectivity and functional topology described by the transformation $\hat{O}$ within the machine learning platform (Chapter 3). As described by Maass [1-2], neuroscience concluded that a small-world network maximized information transfer while minimizing energy usage. This phenomenon was observed throughout the natural world - occurring in cases such as complex geological formations, flock behavior, and disease proliferation - and continues to be a central topic within chaos and network theory. Heuristic evidence concluded that network design ascribed with such features enable optimal performance. A defining characteristic of a small-world topology was the length distribution of interacting elements to behave as a power-law, *i.e.* the strength of $\bar{w}_i^n$ scales as $d^{-\beta}$ where *d* is the interneuron distance:

$$\left|\langle \bar{w}_j^m | d | \bar{w}_i^n \rangle\right| \propto d^{-\beta} \qquad or \qquad \left|\langle fft(\bar{w}_j^m) | t | fft(\bar{w}_i^n) \rangle\right| \propto f^{-\beta}\,, \tag{4.1}$$

where the second relation utilized Pontryagin duality, $d \rightarrow c \times t$ with c as the speed of light, and the Fourier transform of the first. A network adhering to these constraints was capable of sustained persistent activity even due to small perturbations [3-5] and was in a 'critical' state which allowed for maximal information transfer.

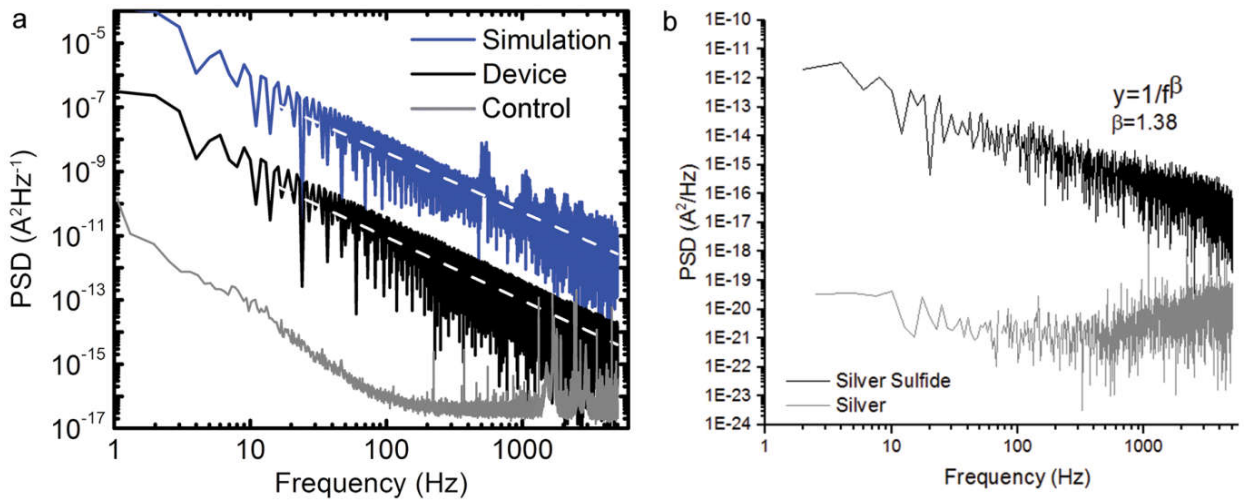

Figure 4.1 D**issipative power-law behavior indicative of self-organized criticality**. The electrical current response of a physical and simulated ASN device (see Chapter 5) in **a** under constant external voltage bias was used to characterize network activity. Network switching/activity timescales showed a dissipative power-law response **b** indicative of a scale-free network.

We examined the device for emergent nonlinear properties considered fundamental to brain function, which were not observed for individual atomic switches operating in simpler geometries - namely recurrent dynamics and the activation of feed forward sub networks. The presence of small-world dynamics within the ASN devices were demonstrated by applying a constant DC bias (Figure 4.1a) across a particular region of the network. This produced persistent, bidirectional fluctuations—both increases and decreases—in network conductivity. In the absence of complex structures within the network, conductivity would increase monotonically under constant DC bias, as in the case of a single atomic switch. Previously reported [6] current fluctuations of this kind are ascribed to recurrent loops in the network that create complex couplings between switches, resulting in network dynamics that chaotically converge to a semi-steady state even under constant bias. A single switch turning ON did not simply lead to an increased potential drop across the next junction in a serial chain, but entropically redistributed voltage across many recurrent connections that can ultimately perturb the system into a new equilibrium as a net change in network conductivity. These fluctuations

were not attributable to uncorrelated flicker noise, as shown by comparing the Fourier transformed current responses in Figure 4.1b of the devices to constant voltage before and after sulfurization. The formation of atomic switch junctions expanded the degree of correlation in current fluctuations, producing small-world 1/f-like behavior across the entire sampled range. This behavior was distinct from that of control devices which flattens to white noise and some high energy, high frequency fluctuations attributed to arcing between neighboring wires.

4.2 Lissajous plots

Lissajous plots are powerful tools to understand the input-output behavior of systems excited with periodic signals. A Lissajous plot allows quick identification of relative harmonic motion between inputs and outputs such as: phase delays, frequency changes, and other nonlinearities. The detailed mathematics of Lissajous plots are described elsewhere[7], but the implementation of this analytical technique is straightforward: the output signal is plotted versus the periodic input signal. If the resulting plot shows a diagonal line, the signals are proportional. An elliptical plot indicates a phase delay between the two signals; the particular case of the circle indicates that the signals are in quadrature (a phase delay of pi rads.). Any deformation from these shapes indicate that the frequency spectrum of the output does not match the one of the input. The strength of the deformation indicates the amplitude of these extra frequencies. For sufficiently strong frequencies, that are not present in the input, the curves will intersect themselves [8].

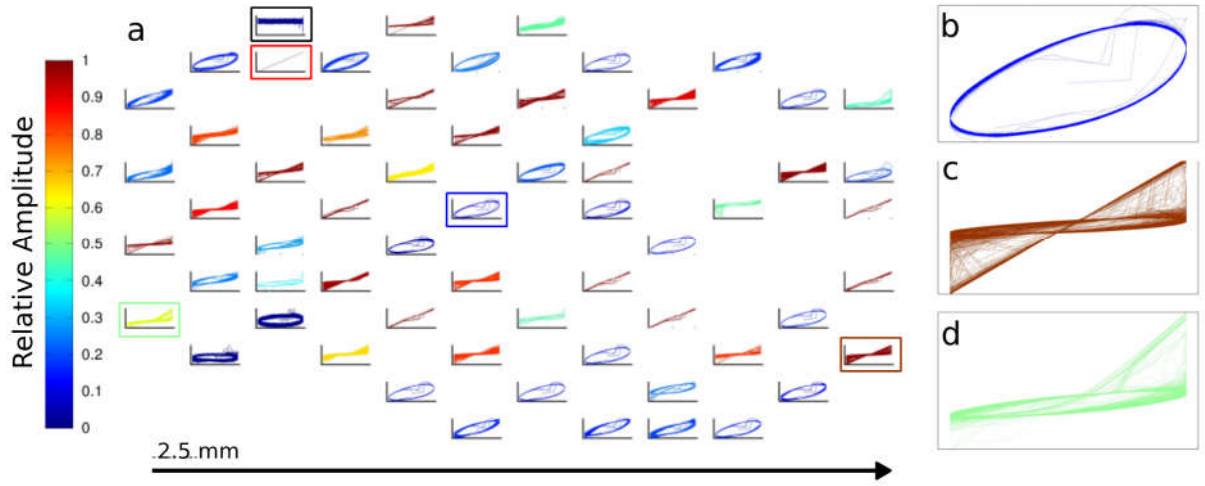

Figure 4.2. Normalized Lissajous. Each subplot in panel **(a)** is a Lissajous figure displaying one minute of the ASN's response to an 11 Hz sine wave vs. the input at 64 spatially distributed measurement points. The signal was input at the electrode marked with the red box, and the device was grounded at the electrode marked with the black box in the upper left of panel **(a)**. Specific classes of relationships are featured in panels **(b-d)** and are color coded to match their location in the network in panel **(a)**. The relationships are: **(a)** initial non-linearity, **(b)** bipolar switching activity, and **(c)** unipolar switching activity. All channels eventually converged and proportionally followed the input signal, resulting in the embedded elliptical shape in all.

The responses of the ASN in Figure 4.2 show non-elliptical Lissajous plots due to the inherent non-linear transformations. Each individual plot shows the input voltage plotted on the x-axis of all plots versus the corresponding channel output on each y-axis. The plots in Figure 4.2a are spatially mapped with respect to the physical electrode locations on the device. Here. a bipolar 11 Hz sine wave was input at the electrode marked with the red box (Figure 4.2a, upper left corner), and the device was grounded at the electrode marked with the black box (Figure 4.2a, above input, upper left corner). As expected, the input signal channel displays a direct linear relationship. The ground electrode displays no significant relationship with respect to the reference signal and only shows white noise behavior. The data presented spans approximately one minute of recorded voltages. The color of the line on each plot corresponds to the relative amplitude with respect to the input amplitude (see colorbar, Figure 4.2a).

Several channels show an ellipsoidal shape (Figure 4.2, panel b-d) indicating that their phase is shifted respect to the input phase. These curves are not a perfect ellipses; the

deformations are due to the non-linear processing of the ASN discussed in the previous section. Slight distortions in the elliptical shape are a consequence of steady dynamical changes to the signal's harmonic motion, but the predominant elliptical shape indicates that the system eventually settles into a proportional response at a mean signal value ~0 V. Other channels present a bowtie plot (Figure 4.2, panel c) that indicates that this channel is undergoing a symmetric resistance change in response to the formation and annihilation of atomic switches across the network, with a 2.2×10^{-3} V mean amplitude. Interestingly, yet another set of channels present a lopsided bowtie plot (Figure 4.2, panel d) suggesting that the network in the neighborhood of those electrodes has a polarity-dependent response, and is undergoing rectification. The mean of this channel is the highest of the three at 0.132 V. Careful examination of Figure 4.2, panels c and d yields an embedded elliptical shape, which suggests that there were two classes of network behavior recorded at that location: non-linearity and proportionality. Examination of the raw voltage traces supports this assumption (Figure 4.3): an initial non-linear response due to large magnitude switching events eventually converged to a proportional response.

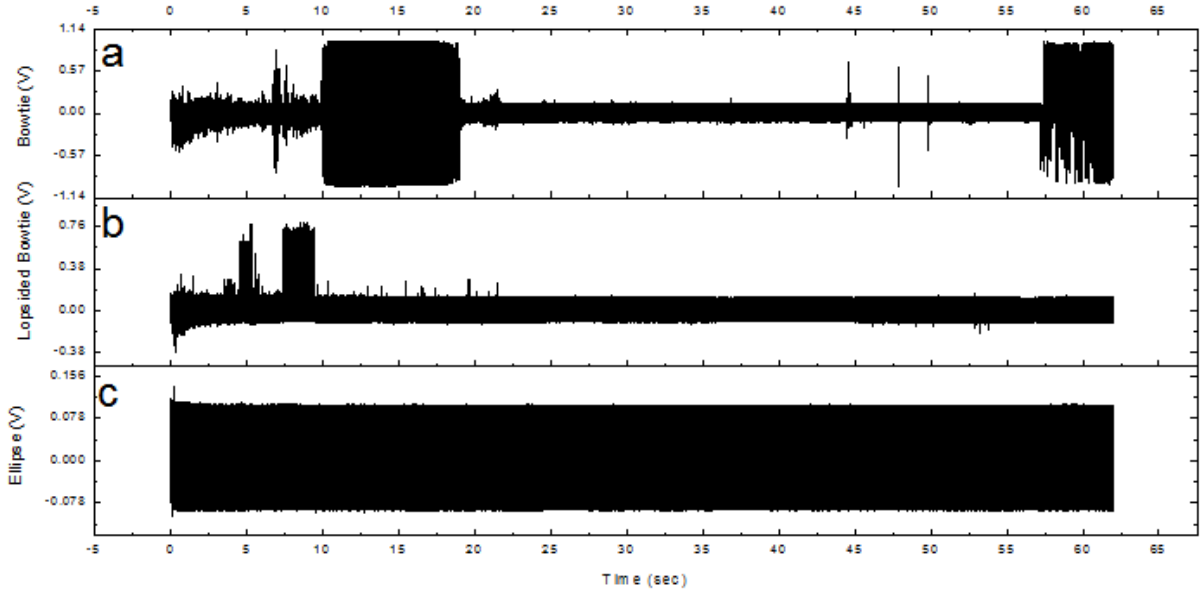

Figure 4.3 Raw Voltage traces recorded from ASN support the assertions put forth by the Lissajous plots, highlighting a variety of dynamic behaviors present in the network.

The variety of behaviors displayed in the Lissajous plots indicate that the ASN is a good approximation of a dynamical system [9]. The localized regions of varying activities and behaviors are reminiscent of "edge of chaos" dynamics represented in well-known dynamical systems like the brain [4]. The "edge" happens at the transition between random/disordered and ordered states. It is suggested that operating in this dynamical regime leads to maximum information processing and therefore computational capacity [1].

4.3 Bibliography

[1] R. L. a. W. Maass, "What makes a dynamical system computationally powerful?," presented at the New Directions in Statistical Signal Processing: From Systems to Brain, 2005.

[2] T. N. Wolfgang Maass, Henry Markram, "Real-time computing without stable states: A new framework for neural computation based on perturbations," *Neural Computation,* vol. 14, pp. 2531-2560, 2002.

[3] C. T. Alireza Goudarzi, Natali Gulbahce, and Thimo Rohlf, "Emergent Criticality through Adaptive Information Processing in Boolean Networks," *PHYSICAL REVIEW LETTERS,* vol. 108, 2012.

[4] E. T. Ariel Haimovici, Pablo Balenzuela, and Dante R. Chialvo, "Brain Organization into Resting State Networks Emerges at Criticality on a Model of the Human Connectome," *Phys. Rev. Lett.,* vol. 110, 2013.

[5] A. L. Sussillo D, "Generating coherent patterns of activity from chaotic neural networks.," *Neuron,* vol. 63, 2009.

[6] A. Z. Stieg*, et al.*, "Emergent Criticality in Complex Turing B-Type Atomic Switch Networks," *Adv. Mater.,* vol. 24, pp. 286-293, 2012.

[7] M. R. A. H. A. H. Al-Khazali, "Geometrical and Graphical Representations Analysis of Lissajous Figures in Rotor Dynamic System," *IOSR Journal of Engineering,* vol. 2, 2012.

[8] E. Y. C. Tong, "Lissajous figures," *The Physics Teacher,* vol. 35, 1997.

[9] S. H. Strogatz, "Exploring complex networks," *Nature,* vol. 410, 2001.

Chapter 5

Simulation of Atomic Switch Network

A complementary study on the effects of global stimulation was done in simulation to form a microscopic understanding of the device dynamics. The simulated network was comprised of interconnected atomic switches using a modified state equation [1-2]. A current controlled memristor model was adopted undergoing ionic drift dynamics at the $Ag|Ag_2S|Ag$ interface based on previously published works [3-5]. The state variable, $w(t)$, represented the doped region produced by migration of Ag^+ mobile ions from pure Ag into the Ag_2S layer. Reduction of Ag^+ at the cathode precipitated Ag nanowire formation with its physical dimensions determining its impedance and characteristic memristive behavior. The atomic switch was observed to have at least two operational regimes characterized by a low and high resistance state, ON/OFF respectively. Simple linear super positioning of the two states captured memristive behavior eloquently and a state variable $w(t)$ was defined:

$$V(t) = \left[R_{on}\frac{w(t)}{w_0} + R_{off}\left(1 \quad \frac{w(t)}{w_0}\right)\right] I(t). \tag{5.1}$$

Above is the classical Ohm's law equation with $w(t)$, the characteristic filament length, capturing filament formation, and determined using the ionic drift model:

$$\frac{dw(t)}{dt} = \left[\mu_v \frac{R_{on}}{w_0} I(t)\right] \Omega(w). \tag{5.2}$$

A physical restraint was imposed on $w(t)$ to account for finite dimensions through the use of a window function Ω:

$$\Omega(w) = \frac{w(w_0 - w)}{w_0^2} \tag{5.3}$$

Modifications were made to the above model to account for nanowires forming Ag|Ag_2S|Ag interfaces. The formulation for voltage induced α/β phase transition of the Ag_2S from monoclinic acanthite to the more conductive body centered cubic argentite was introduced as well as formation/dissolution of conductive filaments [6]. Applied voltage triggers the α/β phase transition creating a more conductive Ag|β-Ag_2S|Ag junction and, more importantly, allowed for Ag cation migration within the Ag_2S in the direction of the electric field. Reduction of Ag cations into Ag^0 occurs at the cathode thereby creating substructures within the β-Ag_2S to ultimately form conductive filaments. The removal of the applied voltage no longer induced Ag cation migration and the system was allowed to return to its thermodynamically favored equilibrium state. A stochastic term and dissolution term incorporated this thermodynamic behavior to the system. The term further modeled any variability among the nanowires and the structural stability of the Ag filament. Stratonovich integrals were employed to solve for the stochastic differential equations. The network was numerically solved as an ordinary differential equation using standard Kirchhoff's current laws with each node-node connection considered as a single atomic switch. The rate of change in filament length was modeled according to:

$$\frac{dw(t)}{dt} = \left[\mu_v \frac{R_{on}}{w_0} I(t)\right] \Omega \quad \tau(w(t) \quad w_0) + \eta(t) \tag{5.4}$$

where μ_v signifies the ionic mobility [7-8]. The window function, given by:

$$\Omega = \left[\frac{w(t)(w_0 - w(t))}{w_0^2}\right] \tag{5.5}$$

was included in (5.2) to incorporate the behavior of elements with state variables at the extreme limits due to ionic drift [8-9]. The term $\left[\mu_v \frac{R_{on}}{w_0} I(t)\right] \Omega$ provided the dependence of filament growth rate on the electronic flux, while $\tau(w(t) \quad w_0)$ operated as a dissolution term that served

to return the filament length to its original value w_0 due to the thermodynamic stability of the high resistance state. Although the dissolution rate constant (τ) has not been extensively investigated in the network setting, a numerical survey over three orders of magnitude (1 to $1000\ s^{-1}$) determined the value that best reproduced the prior experimental results for the size of the simulated network. Lastly, a stochastic term $\eta(t)$ accounted for fluctuations in the density of available silver ions and the stochastic nature of the filament formation/dissolution process in physical ASNs. This term, defined by:

$$\eta(t) = \alpha(t)\Delta w(t) \tag{5.6}$$

governed the growth rate of filament sizes, where $\Delta w(t)$ represented the change in filament length at time t reflecting the amount of electric flux through the switch junction. Here, the random variable $\alpha(t)$ introduced a noise factor to the term $\eta(t)$ that was distributed across the network following a random distribution centered at zero with a standard deviation σ_α. The probability distributions for both w_0 and α were examined using simulated network sizes ranging from 3x3 to 10x10 arrays with varying degrees of connectivity densities.

Finally, the connectivity in the simulation was modeled after the known interconnectivity of ASNs [10]. Physical networks are grown from copper seeds spatially distributed on the substrate, which serve as nucleation sites for the electroless deposition of silver metal under diffusion-limited conditions. This directed self-assembly process generates networks with a large distribution of wire lengths, characterized by SEM in the range of 100 nm to over 1 mm. The network contains elements of a nearest neighbor network, since the wires are likely to connect to those grown from nearby copper seeds (Figure 1.1c-d). They also exhibit characteristics of a random network as long wires extend across the entire network, connecting distant nodes, and also connecting many nodes at once (Figure 1.1b).

Connectivity in the simulation was created by starting with a square lattice of nodes mimicking the copper posts in the hardware design. Links connecting nearest neighbors as well as distant nodes were then assigned randomly with the total number of connections ranging from N=50 to 400. The simulation results reported here represent the typical network response observed with connections reassigned for each run.

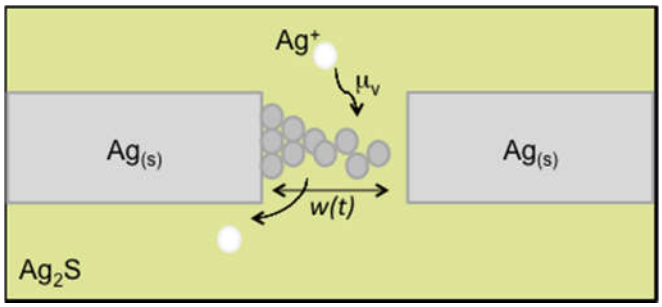

Figure 5.1. Atomic Switch Mechanism Atomic switches are comprised of a Ag|Ag_2S|Ag junction. Applied electrical bias causes Ag cation migration to the cathode where it is reduced, forming a stable metallic filament, resulting in resistance change. This migration is modeled by the filament length w(t), Ag cation mobility μ_v, and additional stochastic terms.

Finally, the values of the physical parameters such as ionic mobility, R_{ON}/R_{OFF} ratio, and average gap size were chosen according to experimental literature values as schematically illustrated in Figure 5.1 [11-13], leaving the only the network size and wiring density as free parameters. Table 5.1 summarizes the range of the values of the parameters explored to produce the results in this report.

w_0 (nm)	$\mu_v(m^2s^{-1}V^{-1})$	R_{on}/R_{off}	$\tau(s^{-1})$	α	N
Ave: 5 σ_{w_0} : 0 - 40%	0.5×10^{-12}	Ave: 10^{-1} to 10^{-3} $\sigma_{on/off}$: 0 - 40%	1 to 10^3	Ave: 0 σ_α: 0 - 30% of $\Delta w(t)$	50 to 400

Table 5.1. Parameters used in the simulation were tested over ranges that are physically relevant to the Atomic Switch Network system: total gap width (w_0); ionic mobility (μ_v) of Ag^+ in Ag_2S; ratio of resistances (R_{on}/R_{off}) at w = 0 and w = w_0; filament dissolution rate constant (τ); modulation (α) level of noise in the w(t) term with each time step; and total number of connections (N).

Network simulations were executed in MATLAB through a graphical user interface (GUI) that provides control over these parameters in addition to the locations and numbers of sources/drains, structure of input waveforms, and magnitude of input signals. The GUI also provides direct monitoring of simulated I-V statistics as well as the current, power dissipation and conductivity of each link within the simulated network (Figure 5.2).

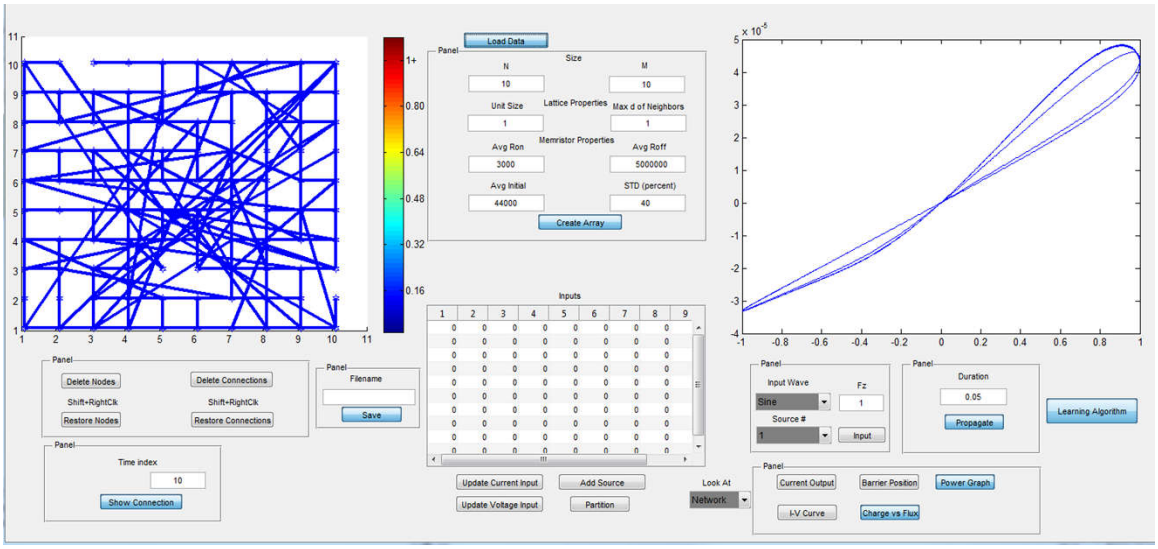

Figure 5.2 Schematic layout of the MATLAB graphical user interface (GUI) used for ASN simulations. The user interface provides control parameters including: network connectivity (N), distribution of w0, RON/ROFF ratio, locations and numbers of sources/drains, as well as the input waveforms and strength of input signals. From the panels at the top right corner one can monitor the simulated I-V statistics, current, power dissipation and conductivity of each link.

5.1 Bibliography

[1] D. B. S. a. D. R. S. J. Joshua Yang, "Memristive devices for computing," *Nature Nanotechnology,* vol. 8, pp. 13-24, 2013.

[2] S. G. S. Strukov D B, Stewart D R and Williams R S, "The missing memristor found," *Nature,* vol. 453, pp. 80-83, 2008.

[3] E. C. A. Demis, R.; Sillin, H. O.; Scharnhorst, K.; Sandouk, E. J.; Aono, M.; Stieg, A. Z.; Gimzewski, J. K., "Atomic Switch Networks Nanoarchitectonic Design of a Complex System for Natural Computing," *Nanotechnology,* vol. 26, 2015.

[4] R. A. Henry O Sillin, Hsien-Hang Shieh, Audrius V Avizienis, Masakazu Aono, Adam Z Stieg and James K Gimzewski, "A theoretical and experimental study of neuromorphic atomic switch networks for reservoir computing," *Nanotechnology,* vol. 24, p. 384004, 2013.

[5] D. B. Z. Biolek, V. Biolkova, "SPICE Model of Memristor with Nonlinear Dopant Drift " *Radioengineering,* vol. 18, 2009.

[6] S. I. S. A.I. Gusev, "Effect of small size of particles on thermal expansion and heat capacity of Ag2S silver sulfide," *Thermochimica Acta,* vol. 660, 2018.

[7] L. Chua, "Memristor-The missing circuit element," *IEEE T. Circuits Syst.,* vol. 18, pp. 507-519, 1971.

[8] D. B. Strukov*, et al.*, "The missing memristor found," *Nature,* vol. 453, pp. 80-83, 2008.

[9] E. N. Oskoee and M. Sahimi, "Electric currents in networks of interconnected memristors," *Phy. Rev. E,* vol. 83, p. 031105, 2011.

[10] A. Z. Stieg*, et al.*, "Emergent Criticality in Complex Turing B-Type Atomic Switch Networks," *Adv. Mater.,* vol. 24, pp. 286-293, 2012.

[11] T. Hasegawa*, et al.*, "Learning Abilities Achieved by a Single Solid-State Atomic Switch," *Adv. Mater.,* vol. 22, pp. 1831-1834, 2010.

[12] T. Ohno*, et al.*, "Short-term plasticity and long-term potentiation mimicked in single inorganic synapses," *Nat. Mater.,* vol. 10, pp. 591-595, 2011.

[13] K. Terabe*, et al.*, "Quantized conductance atomic switch," *Nature,* vol. 433, pp. 47-50, 2005.

Chapter 6

Device activation

Robust, hysteretic switching in ASN devices requires device activation by a symmetric triangle wave ramp applied across the network. As net flux through the network increased, connections became increasingly polarized and conductive, resulting different behavioral regimes (insets of Figure 6.1a-c). A lack of completed metal filaments characterizes the initial state in Figure 6.1a (inset) as the 'soft switching' regime. Continued sweeping causes the formation of a continuously conductive path across the network, with intermediate connections operating in a higher conductance state. This transition is observed as a dramatic change in conductance, shown in the inset of Figure 6.1b, where network response changes from soft to 'hard switching' as the fraction of strongly memristive elements increases past the percolation threshold [1]. Continuous sweeping of the applied bias is known to encourage thickening and stabilization of as-formed nanofilaments [2-4], producing behavior that is robust to fluctuations in silver ion deposition/dissolution (Figure 6.1c inset). As a result, there is an increased likelihood for an element in the network to operate in the strongly memristive regime.

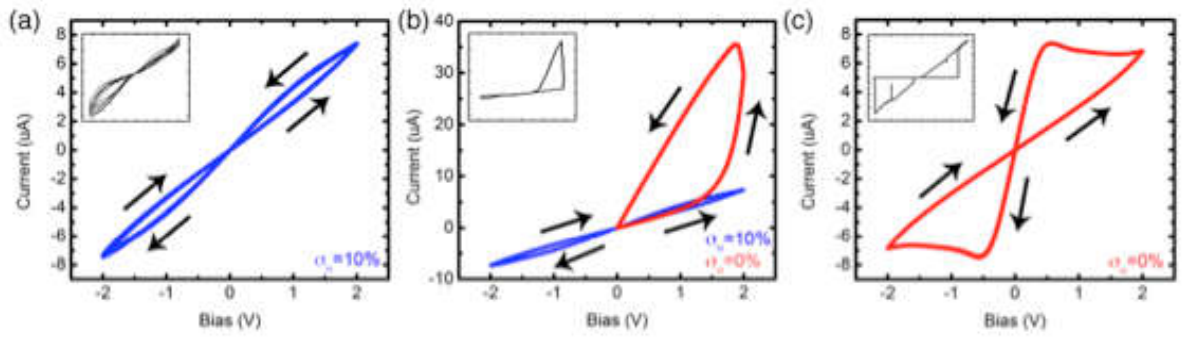

Figure 6.1. Simulation of device activation using a 10x10 network with N=126, average R_{on}/R_{off}=10^{-2} and τ=10 s^{-1} under a triangle wave input bias of ±2 V at 10 Hz demonstrating a) an initial soft switching (σ_α =10%) repeated indefinitely until b) a transition in behavior from soft (blue, σ_α =10%) to hard (red, σ_α =0%) switching. c) Hard switching persists indefinitely with σ_α=0%. This behavior was ubiquitous across all configurations with discrepancies in the bias amplitude/frequency. Experimental device activation curves shown as insets for comparison.

To reproduce this activation process, the simulation included the effects of filament stability on network response by tuning the distribution of noise factor $\alpha(t)$ while holding input bias amplitude and frequency constant. A high noise level (σ_α >7%) was found to inhibit stable transitions, or w(t) from crossing the interfacial barrier in the window function, which enforced the soft switching state (Figure 6.1a). Lowering σ_α enables w(t) to increase past the barrier without interruption, inducing the transition from soft to hard switching at the network level (Figure 6.1 b-c). Consequently, the noise level serves as a control parameter for the number of strongly memristive elements and the soft/hard switching behavior, supporting the conjecture on the mechanism behind the different switching behaviors.

Selecting the appropriate strength of the stochastic term enabled the ASN simulation to agree qualitatively with the experimental memristive behavior. While simulation and experiment show a quantitative difference in the hard switching regime (Figure 6.1c and inset), specifically in the rate of change between the high and low resistance states, stronger agreement with respect to R_{on}/R_{off} ratio (Figure 6.2) and the rate of resistance state change (Figure 6.1c) was observed in a more densely connected simulated network.

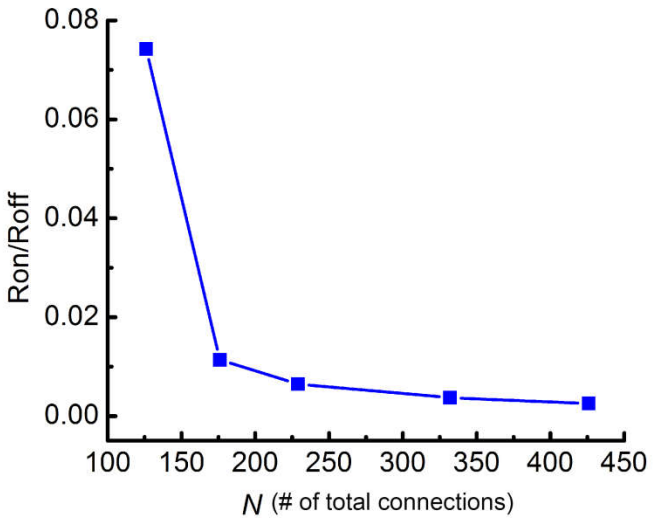

Figure 6.2 Effect of network connectivity density. Increasing the number of connections (N) results in decreased R_{ON}/R_{OFF} ratios in networks with the hard switching response. The sparse connectivity of the network used in Figure 3(c) with respect to physical ASN devices (inset of 3c) generates a comparatively high R_{ON}/R_{OFF} ratio, producing the qualitative difference in appearance between the results of simulation and experiment.

To elucidate the underlying dynamics of the activation process, internal conductance maps of a sparse network reveal the conductive pathways responsible for maximum current flow when operating in the soft switching, transitional, and hard switching states (Figure 6.3). A single, dominant pathway emerged at the transitional state and was destroyed in the subsequent input bias sweeps that drove the network into the hard switching state.

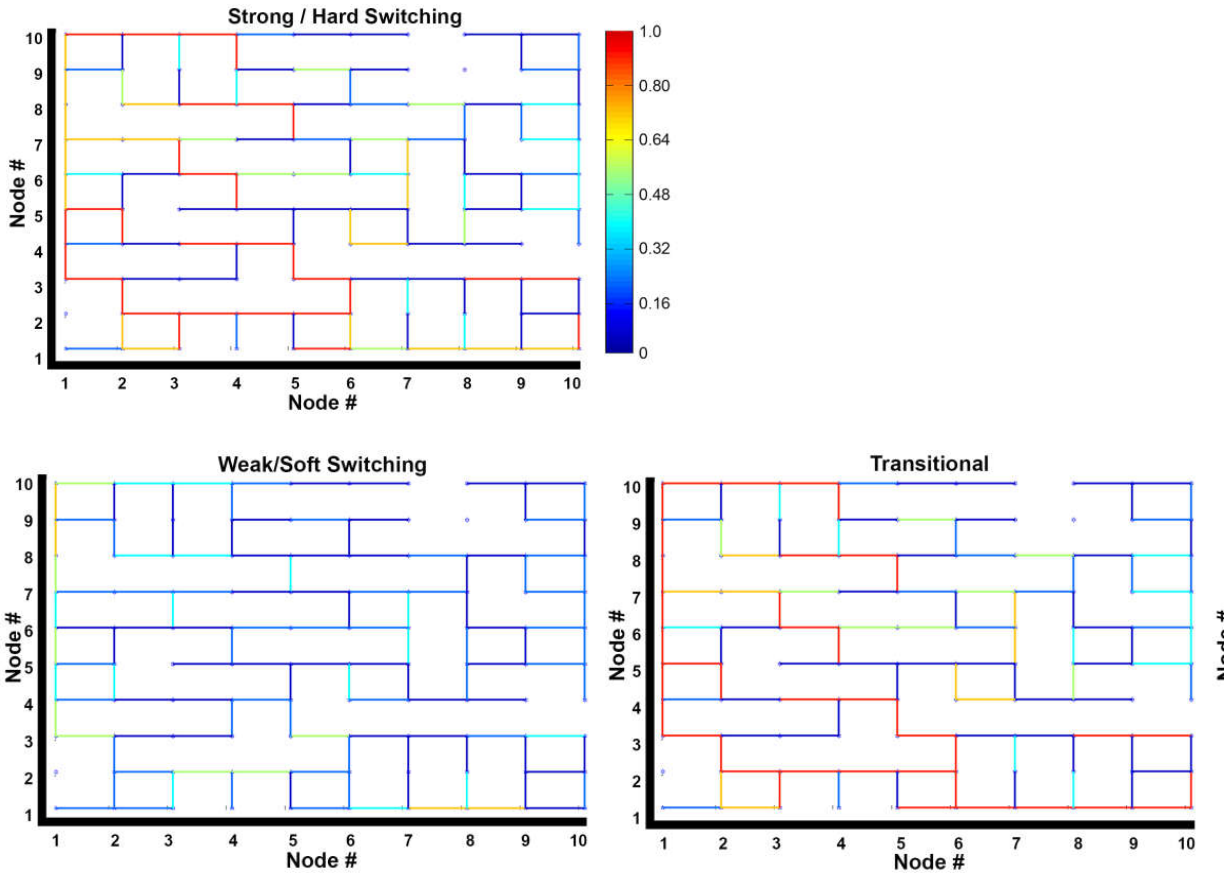

Figure 6.3 Network connectivity maps. Simulated internal connectivity at the point where of maximum current passing through a network (N=106) without long range connections to clearly reveal conductive pathways in the soft switching, transitional, and hard switching state. Warmer color (red) corresponds to higher conductivity/closer to maximum filament growth. In the soft switching state the network is made of switches with low conductances, whereas a single dominating pathway is responsible for the high current through the system in the transitional state. In the subsequent cycle, the network is in the hard switching regime where the dominant pathway seen in the transitional state has destroyed and distributed connections with increased conductance are observed.

Further examination of functional connectivity over the entire activation process (Figure 6.4) enabled identification of equivalent regions of network conductance for the transitional and hard switching states.

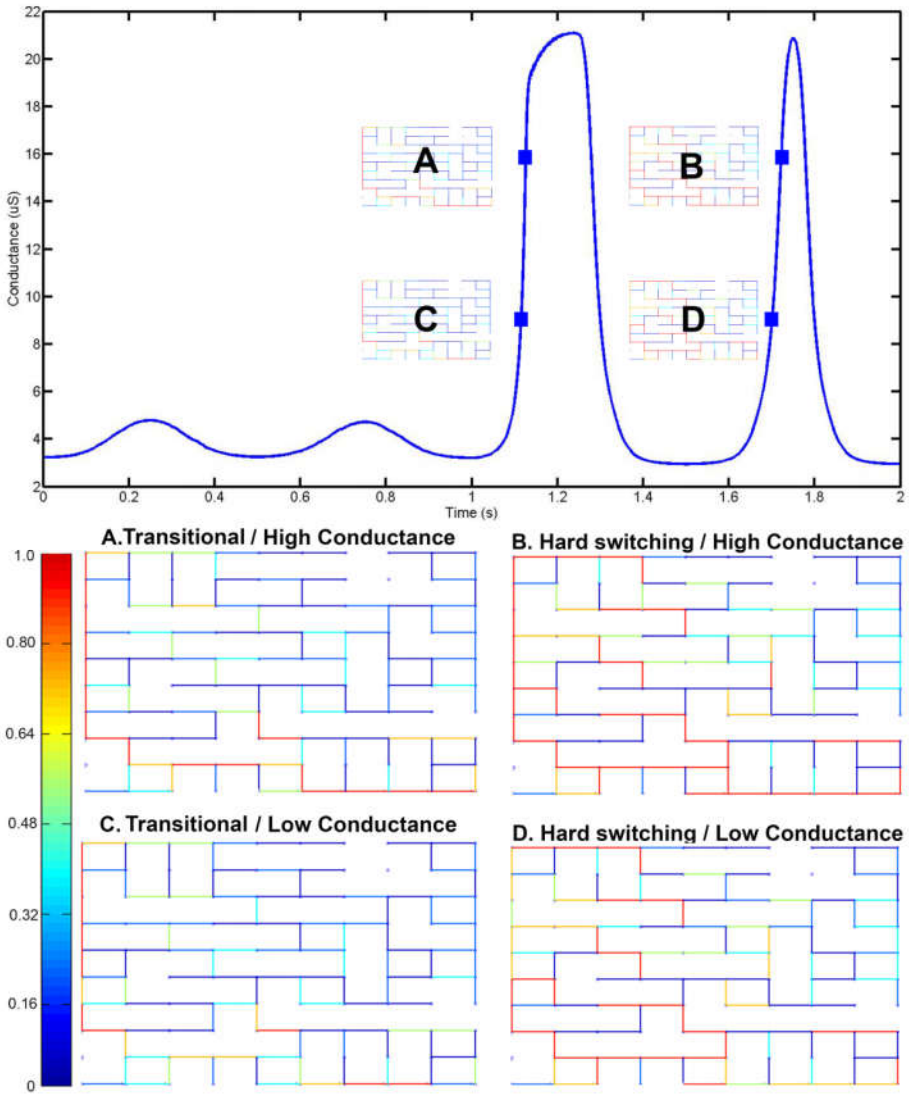

Figure 6.4 Network connectivity maps. Simulated internal connectivity of a network (N=106) without long-range connections to clearly reveal conductive pathways at multiple points along the activation timeline. Network conductance (blue line) over the entire activation sweeps is shown. The maximum conductance observed when the network is transitioning (A) and in the hard switching state (B) are the shown to be the same. However, simulation snapshots of the internal connectivity at each point show the network taking different routes through phase space in order to reach the highest conductance state. In addition, the conductance pathways are more distributed in the hard switching state.

In particular, the network followed different trajectories to achieve values of maximum conductance, whereby network conductance was increasingly distributed in nature for the hard switching case. In the results described below, both w_0 and $\alpha(t)$ were sampled from Gaussian distributions. Parameters of the distribution of w_0 were selected to reproduce the experimental I-V curves by matching the bias voltage used in the simulation to our experiment.

6.1 Bibliography

[1] A. Z. Stieg*, et al.*, "Emergent Criticality in Complex Turing B-Type Atomic Switch Networks," *Adv. Mater.,* vol. 24, pp. 286-293, 2012.

[2] T. Hasegawa*, et al.*, "Learning Abilities Achieved by a Single Solid-State Atomic Switch," *Adv. Mater.,* vol. 22, pp. 1831-1834, 2010.

[3] T. Ohno*, et al.*, "Short-term plasticity and long-term potentiation mimicked in single inorganic synapses," *Nat. Mater.,* vol. 10, pp. 591-595, 2011.

[4] K. Terabe*, et al.*, "Quantized conductance atomic switch," *Nature,* vol. 433, pp. 47-50, 2005.

Chapter 7

Atomic Switch Plasticity

In conjunction with optimizing the reservoir's transformation capability in $\hat{O}$, reservoir learning inherently required a memory quality and plasticity for selective information storing [1]. A powerful feature of atomic switches and memristive-like devices was the observation of a brain-like physical phenomena known as *Long-Term Potentiation* (LTP) and *Short-Term Potentiation* (STP). Both function and memory has been ascribed to STP and LTP dynamics in neurological studies [2-3]. Neuron signal transduction through potentiation spikes showed timing dependencies which directly encoded information within the spike's line shape. Simultaneously, brain functionality and behaviors developed as neuron ensembles cooperatively spiked to adopt specific emergent behaviors.

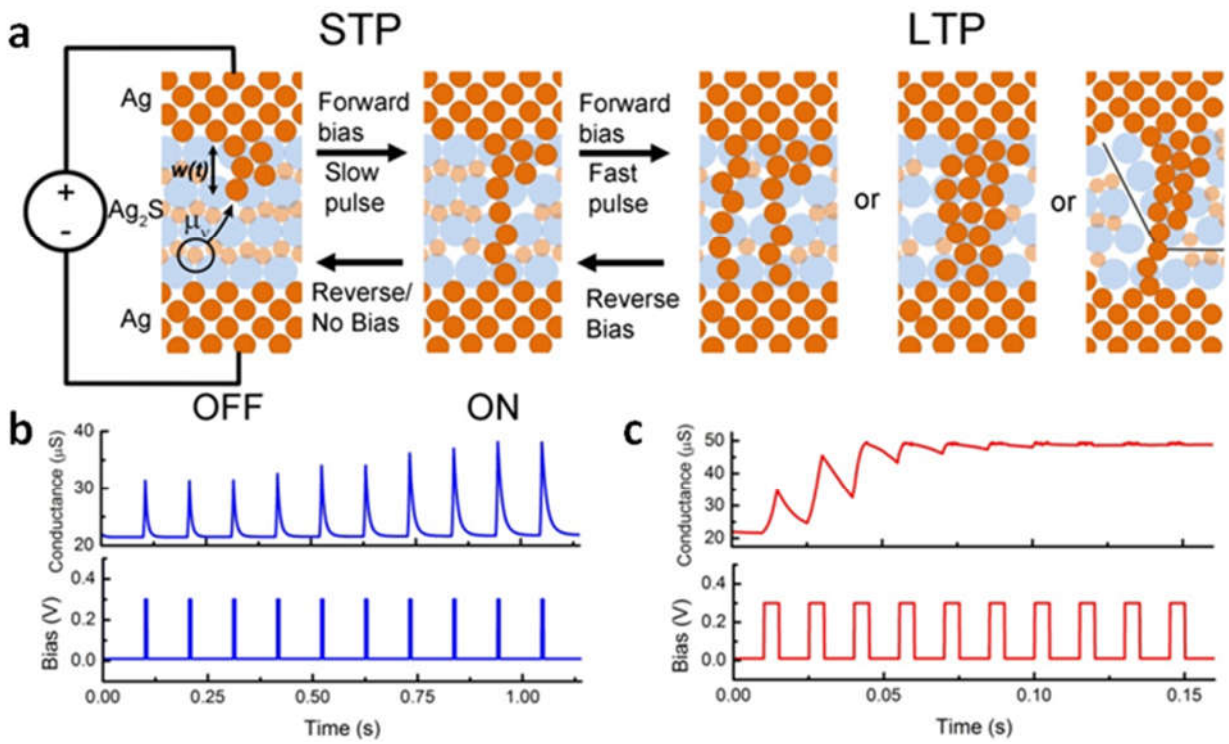

Figure 7.1 Spike-time dependent plasticity in a single atomic switch. Continued stimulation of the atomic switch caused formation of metallic filaments across the gap/active layer in **a**. The electrical response became increasingly dominated by tunneling mechanisms derived from single atom "contact". A 300 mV spike 5 ms width voltage train at a period of 100 ms in **b** stimulated the atomic switch to form a single Ag filament. Single atom contact increased conductance to the ON state during stimulation while thermodynamic dissolution drove the system back to the OFF state. In **c**, the pulse train period was shortened to 10 ms allowing multiple filament formations. Measured conductance monotonically increased before reaching a stable conductance state. Filament structure and stability modulated the electrical response and emerges as empirically determined as Short-Term Potentiation (STP) in **b** and Long-Term Potentiation (LTP) in **c**.

These neurological phenomena was observed [4-5] within the active Ag_2S region in the atomic switch as aggregations of Ag^+ cations. Observation of a large impedance change in the atomic switch under an external voltage was attributed to a crystal transition of the active material Ag_2S [6]. This transition gave rise to a weakly memristive behavior prior to the formation of Ag filaments across the interface. In the absence of continued applied bias, the conductive filaments eventually returned to their stoichiometric, thermodynamically favored equilibrium state, reverting the atomic switch to its initial high OFF resistance (Figure 7.1a). Continued application of bias voltage resulted in a concurrent increase in electric current through the device, which then further drove migration of silver cations toward the cathode. At the

cathode mobile silver cations were subsequently reduced to Ag^0, forming a highly conductive Ag nanofilamentary wire. The completion of this filament resulted in a strong transition to an ON state (Figure 7.1a) with a dramatic increase in conductivity (Figure 7.1b). Removal of the applied bias resulted in filament dissolution as the device again returns its thermodynamic equilibrium state (Figure 7.1b). The completion and dissolution of this filament characterized strongly memristive behavior. Continuous application of a bias voltage served to increase filament thickness as additional silver cations was reduced, causing thickening of the metallic filament (Figure 7.1c). This dynamic process has been shown to alter the dissolution time constant, and can be externally controlled by changing the input bias pattern (e.g. pulse frequency). Such changes in volatility can be interpreted as short-term or long-term potentiation (STP and LTP).

7.1 Feedforward Subassemblies

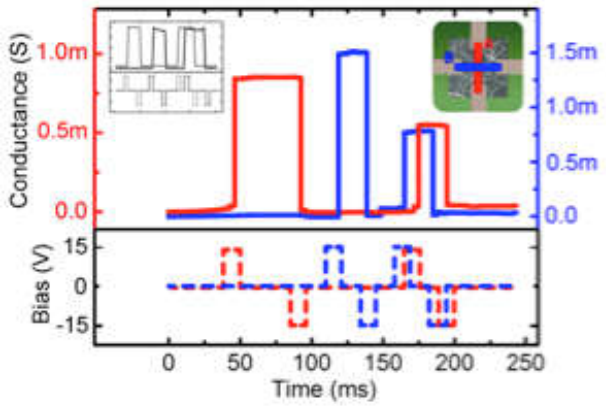

Figure 7.2 Bi-Stable Switching Spatially overlapping channels A and B can be modified independently by write/rewrite pulses, emulating the 2-bit switching functionality of actual device behavior (inset). This simulated 10x10 network (N=219, average $R_{on}/R_{off} = 10^{-3}$, σ_α=2.5%) was partitioned with 4 separate 4x4 blocks to serve as electrodes. Spatially defined ON/OFF switching was induced by applying write/rewrite voltage pulses (15 V, 10 ms duration) across the channels specified in the figure. Measurements of conductance across all 6 possible channels were conducted with 1 V read pulses of negligible period.

Network plasticity was investigated as a mechanism for the formation of feedforward pathways within ASNs, as though they have an inherently recurrent architecture. Previous

studies on physical ASNs have demonstrated their functionality as a two-bit memory storage device with spatially controlled, independent switching channels using pulsed electrical stimulation [7]. This experimental result, which used macroscopic electrodes in contact with a large area of the network to apply bias voltage stimulation, was also successfully simulated as illustrated in Figure 7.2. To comply with the experimental setup, a 10x10 network simulation was partitioned such that in each corner, a 4x4 block of nodes served the same purpose as a physical device electrode. A channel was defined by selection of one block as the source and another as the drain for application of an input bias voltage, with 4 blocks allowing for 6 possible channels. As shown in Figure 7.2, suprathreshold training pulses applied across 2 channels altered their respective conductances independently, even though the pathways were physically overlapping. By monitoring simulated connectivity maps of the other 4 conductance channels during this process, dynamical reconfigurations of the network connectivity were observed (Figure 7.3).

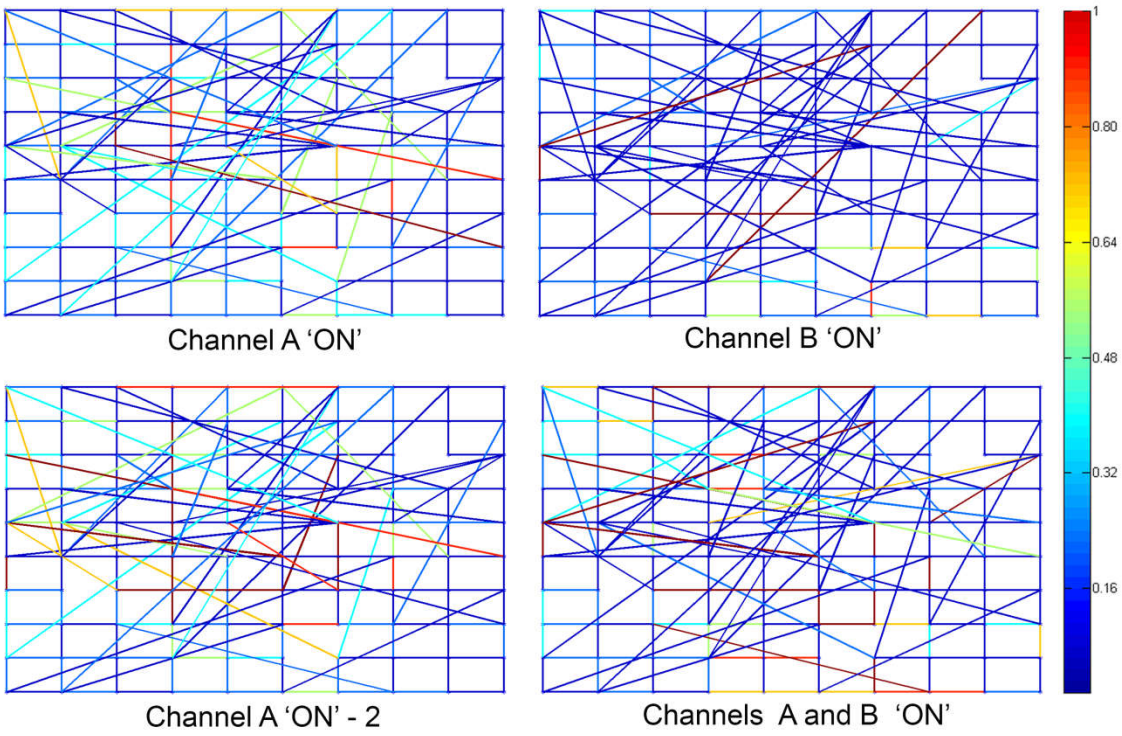

Figure 7.3 - Network connectivity maps. Simulated internal network configurations (N = 219) at different ON/OFF configurations corresponding to results in section 3.3 and Figure 5 describing the formation of feedforward assemblies. In ON states of the network, conductances do not distribute uniformly. In fact, the simulation shows that several different configurations may correspond to the same ON/OFF channel configuration depending on the history of channel switching. For example, the internal configurations responsible for the ON of channel A (red in Figure 5) at the two time points when it is activated, before/after the activation/deactivation of channel B (blue), is shown.

Thus, nonvolatile memory write/rewrite steps occur concurrently with nontrivial changes elsewhere in the network. Different write/rewrite pulse combinations can store information while simultaneously allowing the network to evolve through new configurations. Investigations of structures and stability of feedforward subassemblies may be conducted by carrying out random or targeted deletion of links belonging to a given channel in relation to the strength and duration of the external pulses that induced its formation. Scaling the network size increases the number of distinguishable network states, allowing for increased memory storage and diversity of nonlinear interactions.

7.2 Bibliography

[1] H. Jaeger, "The ``echo state" approach to analysing and training recurrent neural networks - with an Erratum note," German National Research Center for Information Technology2001.

[2] R. L. a. W. Maass, "What makes a dynamical system computationally powerful?," presented at the New Directions in Statistical Signal Processing: From Systems to Brain, 2005.

[3] T. N. Wolfgang Maass, Henry Markram, "Real-time computing without stable states: A new framework for neural computation based on perturbations," *Neural Computation,* vol. 14, pp. 2531-2560, 2002.

[4] L. F. A. S. B. Nelson, "Synaptic plasticity: taming the beast," *Nature Neuroscience,* vol. 3, p. 1178, 2000.

[5] A. L. Sussillo D, "Generating coherent patterns of activity from chaotic neural networks.," *Neuron,* vol. 63, 2009.

[6] S. I. S. A.I. Gusev, "Effect of small size of particles on thermal expansion and heat capacity of Ag2S silver sulfide," *Thermochimica Acta,* vol. 660, 2018.

[7] A. Z. Stieg*, et al.*, "Emergent Criticality in Complex Turing B-Type Atomic Switch Networks," *Adv. Mater.,* vol. 24, pp. 286-293, 2012.

Chapter 8

Resistance Training

The network's ability to physically encode information within the filament led us to develop a resistance training algorithm to control the network's memory capabilities. The dependency of filament formation on voltage history and charge accumulation illustrated memristive behavior within the atomic switch. Circuits utilizing memristive behavior tend to have complex trajectories with nondeterministic solutions and classified as Chua circuits [1]. Initial conditions and stochastic fluctuations helped determine the circuit's trajectories and operational regime, thereby having statistical control on its operation. The circuit parameters of impedance, inductance, and capacitance were used to determine the trajectories of Chua circuits, but other driven systems have included filters, op-amps, and other sources for noise. Though the atomic switches' equivalent parameters evolved with operation, impedance change dominated most of the activity while periphery parameters were treated using thermodynamic approximations [2]. A resistance training algorithm was constructed to tune the network operational regime, while using resistance stability as a thermodynamic approximation of the periphery parameters in simulated models, see Chapter 5.

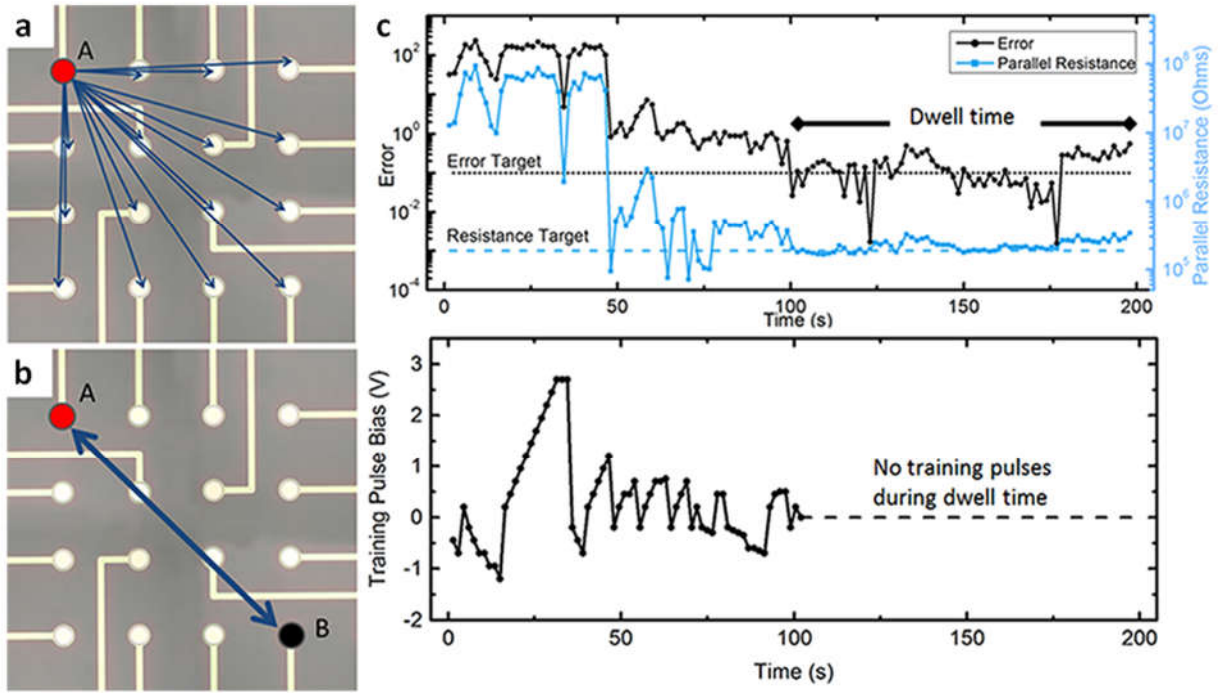

Figure 8.1 Resistance learning algorithm. Determination of network wide stability/activity under operating conditions was conducted using a target resistance learning algorithm. A schematic of the write and verify training scheme, and typical results for an individual training trial. a) Sub-threshold measurement pulses establish the parallel resistance of A, followed by b) a larger training/write pulse between A and B. c) The parallel resistance of A is recorded and compared to the target after each training pulse, when error is minimized the training ceases and the duration of the achieved target state is recorded as the dwell time.

The resistance training experiments were performed using a precision source measure unit (National Instruments 4132) and a high-speed switch matrix (National Instruments 2532) within a PXIe unit (National Instruments 8108), enabling rapid resistance measurements between any combinations of 16 chosen electrodes. Resistance training was implemented through repetition of a two-step process as shown in Figure 8.1. In the first step, an electrode A was selected randomly and the resistance between this reference and every other electrode was measured using a small (200 mV, 10 ms) bipolar pulse in order to minimize influence on network resistances, as shown in Figure 13a. The individual resistances of electrode A with each of the other 15 electrodes, R_{Aj}, defined the network state by calculating the total resistance between electrode A and the rest of the network, as though the paths from electrode A to every other electrode were resistors in parallel:

$$R(i) = \left(\sum_{\substack{j=0 \\ j \neq A}}^{15} \frac{1}{R_{Aj}} \right)^{-1}. \quad (8.1)$$

This quantity is hereafter referred to as the 'parallel resistance'. In the second step, a second electrode B was selected randomly, and a large unipolar training pulse (100 ms, >±200 mV) was applied to influence the parallel resistance of electrode A, as shown in Figure 8.1b. Using the same electrode I/O scheme, the measure/training cycle was repeated until the parallel resistance of A reached the target resistance. For all trials the target resistance was predetermined, irrespective of the initial network resistance.

In order to achieve training, an error function and rule set was devised. This system was designed to create sensible and consistent voltage adjustments even when both target resistance and parallel resistance error could vary by several orders of magnitude. The error function and rule set also correctly accounted for events in which the parallel resistance overshot the target. Convergence of the parallel resistance to the target resistance was evaluated using an error function:

$$E(i) = \frac{1}{2}\left(\frac{R(i)}{R_g} \quad \frac{R_g}{R(i)}\right). \quad (8.2)$$

Where R_g was the target resistance, and *R(i)* was the parallel resistance. The error *E(i)* was calculated after each pulse/measure cycle, and adjustments to the training pulse bias were made by evaluating the relative change in error $C(i) = \frac{E(i)}{E(i-1)}$ from one cycle to the next using equations (8.3) and (8.4), which are described below.

Equation (13) concerned changes in the absolute magnitude of *C(i)* to evaluate changes in the absolute magnitude of the training pulse, *V(i)*. If the previous training pulse resulted in a

large decrease in error, $|C(i)|$ would be less than 1. If significantly less than 1, as determined by an empirically determined threshold, C_m=0.6, then the training pulse $V(i)$ was considered productive and no changes were made. If the previous pulse produced a significant increase in error, $|C(i)|$ would be greater than 1. If $|C(i)|$ was greater than $\frac{1}{C_m}$, the pulse was considered counterproductive and the training pulse magnitude was reset to a minimum value, V_{min}. If $|C(i)|$ was between C_m and $\frac{1}{C_m}$ (i.e. approximately equal to 1) then the error had not significantly changed as a result of the previous pulse, indicating little influence on the parallel resistance. The pulse magnitude was then increased by V_{inc}.

$$V(i+1) = \begin{matrix} V(i), & \text{if } |C(i)| < C_m \\ V_{min}, & \text{if } |C(i)| > \frac{1}{C_m} \\ V(i) + V_{inc}, & \text{if } C_m < |C(i)| < \frac{1}{C_m} \end{matrix} \quad (8.3)$$

Next, equation (14) was used to determine the need for changes to the polarity of the training pulse. If $R(i)$ and $R(i-1)$ were both greater or both less than R_g then there was no overshoot and no need to reverse the bias, which is reflected by positive value for $C(i)$. However if $R(i)$ changed enough with respect to $R(i-1)$ that it overshot R_g, $C(i)$ would be negative. In this case the training pulse voltage $V(i)$ was reversed in sign, and its magnitude was automatically reset to the minimum pulse bias V_{min}.

$$sgn(V(i+1) = \begin{Bmatrix} sgn(V(i)), & if\ C(i) > 0 \\ sgn(V(i)), & if\ C(i) < 0 \end{Bmatrix} \quad (8.4)$$

A single pulse/measurement cycle lasted 1.5 s, and the time required to reach the target resistance state was defined as the 'convergence time'. Upon reaching the target resistance, training pulses ceased and network resistances were measured every 0.5 s until the parallel

resistance decayed away from the target and the error exceeded 0.5 (roughly equivalent to 50% error). This duration was defined as the 'dwell time.' The entire convergence/dwell time sequence constituted a single resistance training trial, an example of which is presented in Figure 8.1c. When a trial completed, new electrodes would be randomly selected and the training process was repeated after a 30 s delay.

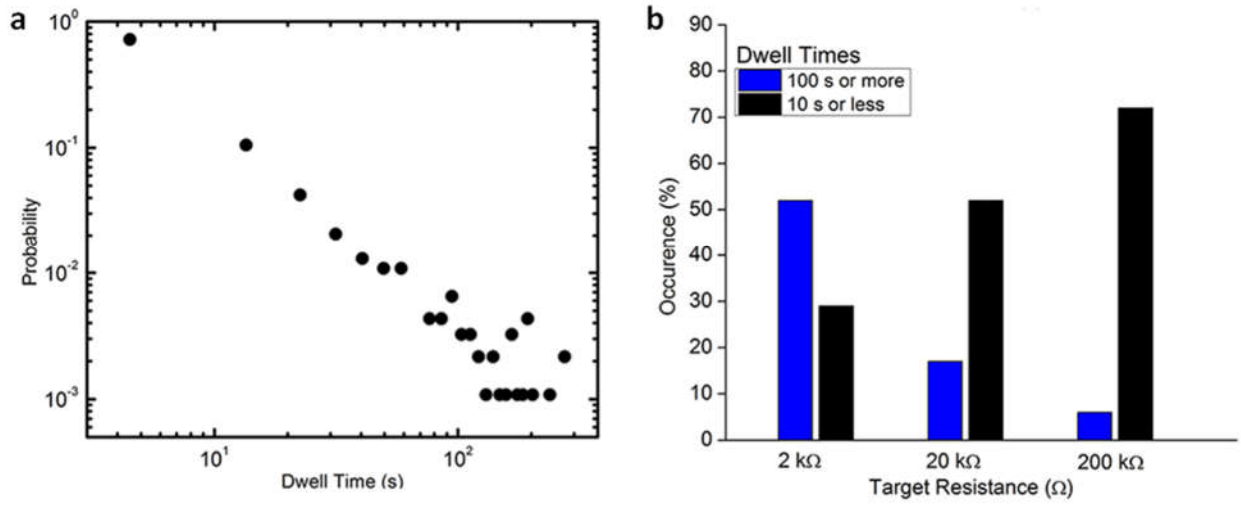

Figure 8.2 Dwell times vary widely, but depend on the target resistance. In **a,** networks are repeatedly trained to 200 kΩ and their dwell times are recorded. By repeating the training program many times on different networks, statistical distributions suggest that the probability *P(D)* of a dwell time lasting for duration *D* follows a power law relationship. Dwell times are generally 10 s or less, with occasional states lasting 100 s or more. As inn **b,** at low target resistances, the final configurations are stable, with over 50% of trials resulting in a final state lifetime of 100 s or more. As target resistance increases, the final states are proportionately less stable

Individual resistance states were the result of conductive silver filaments which bridge the Ag|Ag_2S|Ag gaps, and each filament was vulnerable to thermodynamically driven dissolution. Not surprisingly, a deterministic model of interacting thermodynamic variables was not available, and stability of target resistance was hard to predict. Figure 8.2a shows the distribution of dwell times for networks at the target resistance (R_g=200 kΩ). The distribution suggests a power-law dependency, with dwell times of less than 10 s being most common and occasionally lasting 10 times longer. This distribution was found to depend heavily on the target resistance value, as shown in Figure 8.2b. When R_g=200 kΩ, <10 s dwell times accounted for

72% of trials, but at 2 kΩ, dwell times of 100 s occur in more than 50% of trials. This is the expected result given the underlying operational mechanism of individual atomic switches. Lower resistances were achieved when an individual switch has a thicker conductive filament across the insulating layer, making them more resistant to thermodynamically driven dissolution. In the ASN, lower network resistances are more likely to have an abundance of parallel filamentary pathways, making the target state more resilient against changes from an individual filament. These factors of solved state stability outweigh any effects from repeatedly training the network.

8.1 Simulation Resistance Training

A numerical simulation was constructed based on experimentally determined parameters to model and verify resistance training. Emulating the construction of the device, voltage nodes/electrodes were arranged in a square grid and subsequent node-node connections were introduced to represent nanowires (Figure 8.3b). Connections were categorized either as short-range, within a lattice constant, or long-range and randomly assigned to produce characteristics of nearest neighbor or random network topologies [2]. The initial strength of each atomic switch was randomly sampled following a power-law distribution in equation (4.1) [3] with $\beta = 1.38$.

Resistance training was successfully conducted using the simulated ASN device. Network connectivity was created by randomly distributing 250 connections with 10% of the links within constrained to a length of a lattice constant within a 5x5 grid. The grid size was increased as previously published SEM images showed connections outside the 4x4 area [4-6]. Training pulses were administered between two nodes using the scheme described in equations (8.1-8.4). Resistance training in the simulated network proceeded as observed in the device (Figure 8.1), and could involve a direct approach to the target, or through a series of overshoots.

The simulation allowed a complete analysis of every change in resistance in each link, and Figure 8.3b showed the net change that occurred in each link during the training process. The changes were widespread rather than localized along a single conductive pathway, which supports the hypothesis that network training was achieved by global interactions.

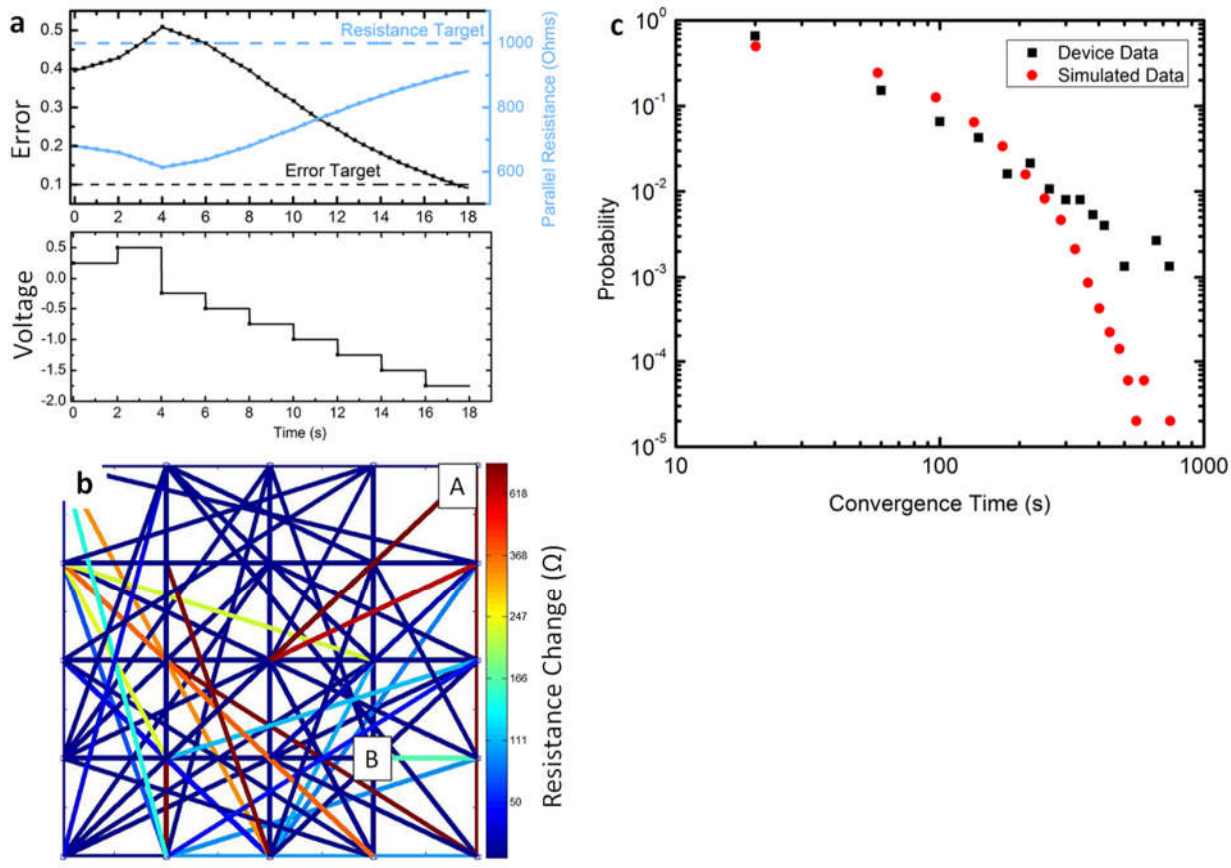

Figure 8.3 Resistance learning algorithm convergence of models. A simulated ASN shows similar behavior in resistance training, and network-wide changes in resistance. A parallel resistance training program identical to the experimental one was used to successfully train parallel resistance. **a)** Target resistance was 1000 Ω, error target was 0.1, training pulses were 100 ms in 250 mV increments, measurement pulses are not necessary in simulation. The effects of resistance training are presented in **b)**, which shows the net resistance change in each link from start to finish. The simulation shows network-wide changes in resistance even though training pulses were applied exclusively from *A* to *B*.

8.2 Bibliography

[1] C. W. W. Leon O. Chua, Anshan Huang, and Guo-Qun Zhong, "A Universal Circuit for Studying and Generating Chaos-Part I: Routes to Chaos," *IEEE TRANSACTIONS ON CIRCUITS AND SYSTEMS-I: FUNDAMENTAL THEORY AND APPLICATIONS,* vol. 40, 1993.

[2] R. A. Henry O Sillin, Hsien-Hang Shieh, Audrius V Avizienis, Masakazu Aono, Adam Z Stieg and James K Gimzewski, "A theoretical and experimental study of neuromorphic atomic switch networks for reservoir computing," *Nanotechnology,* vol. 24, p. 384004, 2013.

[3] R. L. a. W. Maass, "What makes a dynamical system computationally powerful?," presented at the New Directions in Statistical Signal Processing: From Systems to Brain, 2005.

[4] A. V. S. Avizienis, H. O.; Martin-Olmos, C.; Shieh, H. H.; Aono, M.; Stieg, A. Z.; Gimzewski, J. K., "Neuromorphic Atomic Switch Networks," *PLoS ONE,* vol. 2012, 2012.

[5] E. C. A. Demis, R.; Sillin, H. O.; Scharnhorst, K.; Sandouk, E. J.; Aono, M.; Stieg, A. Z.; Gimzewski, J. K., "Atomic Switch Networks Nanoarchitectonic Design of a Complex System for Natural Computing," *Nanotechnology,* vol. 26, 2015.

[6] A. Z. Stieg*, et al.*, "Emergent Criticality in Complex Turing B-Type Atomic Switch Networks," *Adv. Mater.,* vol. 24, pp. 286-293, 2012.

Chapter 9

Harmonic Generation Task

Resistive switches have recently attracted attention for higher harmonic generation (HHG), presented in both single switches and networks [1-2]. Experimental atomic switch networks show HHG to be a function of applied input bias amplitude [3]. Here, numerical simulation was employed to explore HHG by stimulating a network with a sinusoidal input (10Hz) while varying the input amplitude and network connection density (connectivity). For each simulated network of a given connectivity, the HHG analysis was performed on data collected over 10 cycles of the input signal. The network was then reset to the same initial state for the next level of input amplitude. A sharp rise in the ratio of higher harmonic amplitudes to the fundamental at a threshold voltage was found in both experiment and simulation (Figure 9.1a).

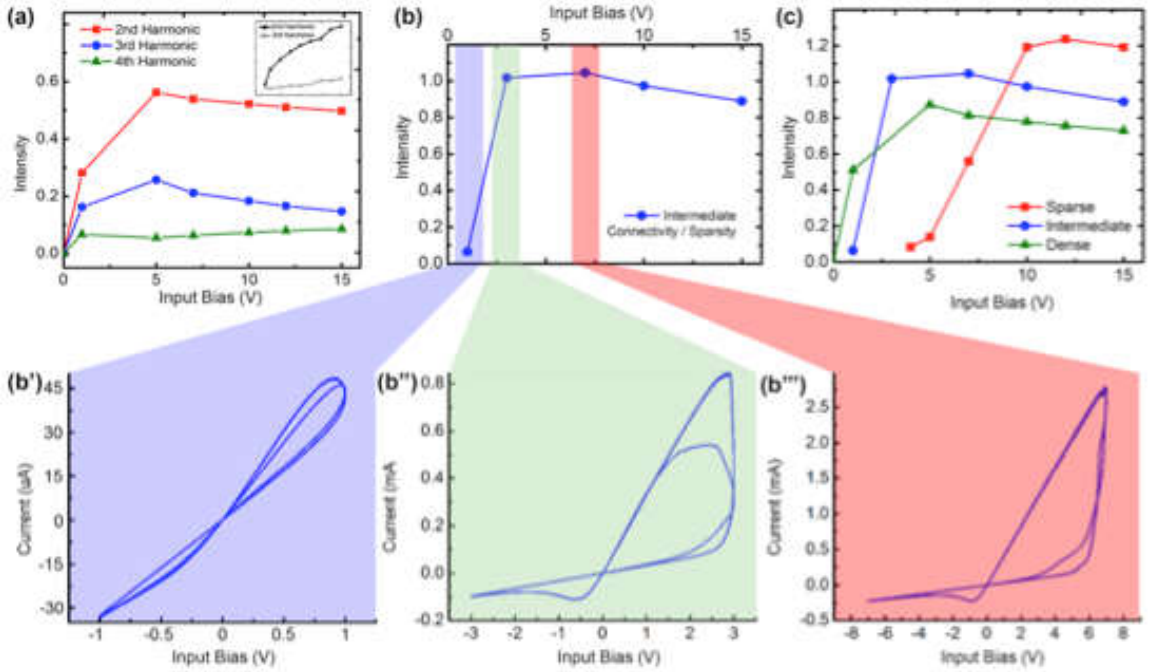

Figure 9.1. Higher harmonic generation can be influenced by network connectivity and input amplitude. Harmonic overtones of several simulated 10x10 networks with average R_{on}/R_{off} = 10^{-2}, σ_α=2.5%, and τ =10 s^{-1}. **a)** The first 3 harmonic overtones of a network with N = 332 showed a threshold voltage for higher harmonic generation. Experimental device curves shown as an inset for comparison. **b)** Harmonic generation as a function of input bias amplitude for a network of intermediate connectivity (N = 229). **b', b'', b'''**) The network I-V characteristics tend towards hard switching behavior and increased higher harmonic generation as a function of input bias amplitude. **c)** The sum of the first 3 harmonic overtones of several simulated of networks with N = (126; 229, 332) indicated a shift toward lower threshold voltages with increasing connectivity ascribed to an increasingly complex network.

The network I-V response curves at increasing levels of input bias amplitude (Figure 9.1b'- b''') illustrate the onset of nonlinearity as characterized by HHG in Figure 9.1a-c. As the voltage increased past the threshold magnitude, the switching behavior moved progressively toward the hard switching regime. The threshold voltage decreased with increased density of connections as shown in Figure 9.1c. An increase in connectivity provides more recurrent substructures in the network and can be related to the nonlinearity in the integration of electrical responses within the system. The decrease in the magnitude of the threshold voltage can be

attributed to an enhanced nonlinearity in the network dynamics where even at lower bias voltage levels, the system tends to reside outside of a linear regime. These changes in the behavior of HHG suggest a way toward quantitative characterization of functional connectivity within ASNs based on their dynamics. As illustrated in Figure 1 and described in Chapter 14, fabrication conditions for ASNs allow substantial control over the size, morphology and density of interconnects. Simulations may therefore be used to optimize physical networks for specific applications.

9.2 Reservoir computing

Higher harmonic generation is potentially of great usefulness in a modern computational paradigm utilizing recurrent complex networks, called reservoir computing (RC). The amplitude and frequency characteristics of produced higher harmonics may be used to quantitatively evaluate the efficiency of a reservoir in different dynamical regimes by accounting for the accessible degrees of freedom in higher dimensional representation space. Using voltage time traces as outputs, it is shown here that the ASN can effectively serve as a nonlinear reservoir capable of performing the waveform generation task (Figure 9.2) considered as a prerequisite to perform reservoir computing [5].

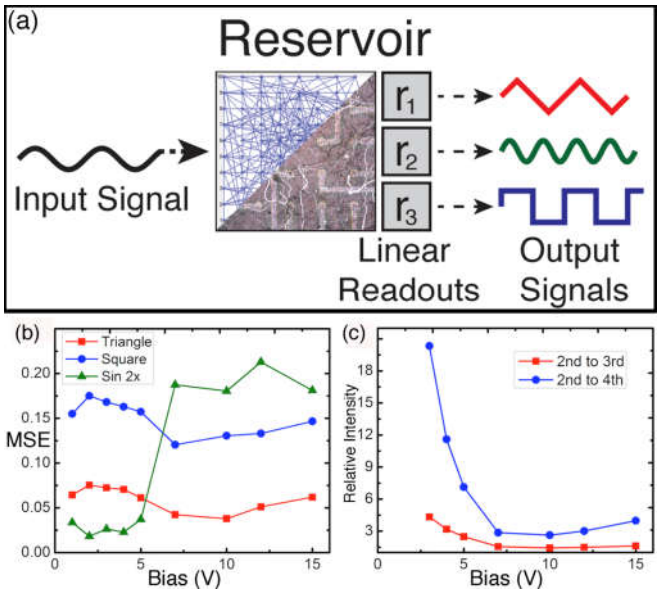

Figure 9.2. Schematic of network simulation used in the waveform generation RC task **a)**, with specific electrodes chosen as inputs/outputs (16 output electrodes). RC was implemented using a 10x10 network (N=126, σ_α=2.5%) with a 5 V, 10 Hz sinusoidal input signal and tasked to produce 10 Hz triangle/square and 20 Hz sinusoidal waveforms. b) Mean-squared error (MSE) for each task with respect to driving amplitude showed minimal error in triangle/square waveform generation task at 10 V, corresponding to the onset of higher harmonic generation, see red curve in **b)**. Performance in the 20 Hz sinusoidal waveform generation task decreased when **c)** the relative amplitude of the average 2nd harmonic intensities of the readouts becomes increasingly diminutive. These results correspond to a strong dependence on the 2nd harmonic for 20 Hz sine generation and the need for HHG in triangle/square generation as expected by Fourier analysis.

Maximizing the number of output signals is advantageous in the context of RC training. Each network node was therefore chosen to serve as an output electrode. By subjecting the network to a sinusoidal input at one corner electrode in the form of an input bias voltage, multiple waveforms including triangle, square and frequency doubling sinusoidal waveforms were constructed through superposition of voltage outputs at each electrode in the simulation. The generated waveform r_q $(q = 1,2,3)$ was then a weighted sum of the voltage outputs from the electrodes with the weights W_q^i calculated by linear regression.

$$r_q = \sum_{i=1}^{m} W_q^i V_i , \quad q = 1,2,3 \tag{9.1}$$

where V_i are the output electrode voltages. Reservoir performance was assessed by the quality of waveform generation and compared across networks with different parameters by calculating the

mean square error (MSE), which quantifies the differences between the target and the generated waveforms:

$$\mathrm{MSE} = \frac{\sum_{n=1}^{P}\left(y_{target}(t_n) - \sum_{i=1}^{m} W^i V_i(t_n)\right)^2}{P} \qquad (9.2)$$

where y_{target} is the target waveform. W^i represent the weight coefficients to be trained with maximum number of outputs $(m = 16)$ at discrete time indices (t_n) over a total length (P) from $n = 1$ to 9000. To see whether the diverse dynamical regimes of ASN may affect the efficiency of RC training, the input gain was varied to access the different characteristics generated of the higher harmonics. The weights were calculated independently using the output responses from the network at each input voltage amplitude. As the magnitude of the applied input voltage was increased, an abrupt onset of HHG (Figure 9.2 b) was observed to influence the associated error for the waveform generation tasks. Specifically, the ratio of the second to higher harmonics (calculated with unweighted average of network outputs) dropped rapidly with increasing voltage (≈8V) as seen in Figure 9.2 c. This bias-dependent reduction in second harmonic amplitude was found to correlate directly with the critical voltage where MSE increased dramatically in the task of generating a sine wave exhibiting frequency doubling of the input signal. As the 2nd harmonic becomes less pronounced compared to the higher harmonics it becomes more difficult to isolate in a linear combination of the output signals through linear regression. In contrast, an increased ratio of higher harmonics to the second harmonics resulted in better performance for the generation of waveforms containing higher harmonic components such as square and triangular waveform. While HHG is not a universal parameter designed to indicate increased computational performances, it does faithfully explain computational performances on specific RC tasks.

The results clearly demonstrate that an ASN can be used as a pattern-generating kernel in RC where it can be optimized by adjusting input gain and network connectivity. Training ASNs to carry out more complex tasks requiring multiple, simultaneous inputs/outputs as well as real-time feedback are currently under investigation [6].

9.3 ASN Device Waveform Regression

Simulations of ASNs have indicated that the system has the fundamental capacity to perform waveform regression [7]. From simulation results, performance depended on the level of higher harmonics produced and the harmonic distortion (Figure 9.2) required for the specific task. For example, the cosine task only requires a shift in its periodicity and, therefore, does not require extensive higher harmonic generation. Conversely, the square wave task requires infinitely distributed harmonics to produce a straight line through wave interference. Further, voltage dependent simulations showed increasing device activation controlled these harmonic generation. Here, the device was expected to perform in a similar way with task difficulty increasing from cosine, triangle, sawtooth, and square due to increasing harmonic requirements. Device initialization and activation to achieve the best performance is described in the previous section.

Experimental performance of various waveform regression tasks using ASN devices are presented in Figure 9.3. To implement waveform regression the ASN was stimulated with a bipolar sinusoidal voltage, inducing switching activity and placing the network in an active state. The output potentials measured at each electrode were then combined using the Moore-Penrose linear regression and optimized during a training period [8-10]. Two-second epochs of data were used to evaluate the ASN's computational capability, where one second of data was allocated each for training and testing. Performance was measured during a one-second period after

training where the ASN accomplished various tasks (Fig. 9.3). The performance of the ASN was quantified by calculating the normalized mean squared error between the target and generated waveforms [11]. Here, the difference between error and unity was used to calculate accuracy.

The ASN was capable in achieving up to ~90% accuracy using 62 of the 64 measurement electrodes for each task. Task complexity increased from cosine to square wave due to increasing mismatch between the sinusoidal input and the target waveform. In the case of cosine generation, the overall waveform of the input is preserved save for a shift in its periodicity. The cosine generation was the simplest task where the ASN performed with the highest accuracy, ~90%. Note that the cosine regression shown in Fig. 9.3a would not be possible using a grid of regular resistors due to their intrinsic linear response. Because individual atomic switches have a non-linear memristive response, it is possible to harness that state function into the highly recurrent structure of the ASN. The highly recurrent structure allowed higher levels of coupled interactions that cannot be captured by a single atomic switch resulting in emergent behaviors. Particularly, the network was capable of producing delayed responses and enabled the network to shift the phase of the input signal by a half-wavelength, producing a cosine. Figure 9.3b shows hardly any mismatch in the triangle generation, achieving a similar ~ 90% accuracy and visually validates the performance metric used throughout our analysis. A similar argument is used to explain the high performance of the triangle wave when compared to the cosine task. The determining factor for reservoir performance is the level of similarity between the target and input signal, where the reservoir acts as a transformational operator to minimize dissimilarities. In both cases, the target waveform is aesthetically similar to a sinusoidal wave and maintains the overall shape of the input signal. Despite steeper edges in the triangle task, the algorithm is able

to correct any differences by selectively combining different representations produced by the ASN.

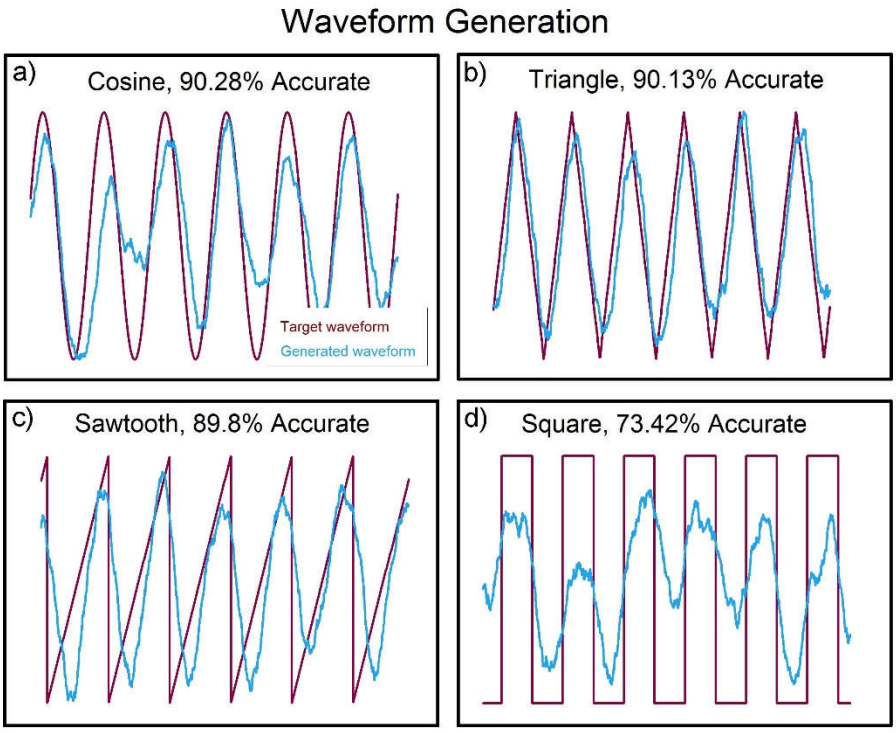

Figure 9.3. Computation of a sinusoidal wave into various waveforms. The above figure shows several waveforms (sawtooth, square, triangle, and cosine) produced using the ASN as a computational device. Each plot contains the desired signal (red) and the computed signal (blue) with their accuracy w.r.t. the desired signal shown above the curves. All tasks share an 11 Hz frequency for their waveforms and share the same dataset with only differences in the target task. The dataset was approximately 1 minute long, divided into 2 seconds epochs, and 1 second within each interval was allocated for training and testing. A 1 second excerpt which best represents device behavior during testing are shown above.

The ASN generated sawtooth (Fig. 9.3c) waveforms with similar accuracy to previously reported simulations of memristive networks at a roughly 90% accuracy [12]. Despite the requirement to produce an instantaneous drop, the ASN delivered the sawtooth waveform with astounding accuracy. Figure 6c illustrates significant mismatch between target and generated waveform at the turning point leading to a minor drop in accuracy. Basic visual inspection shows the sawtooth task retains the overall shape of the sinusoidal input while the square wave task requires complete transformation of the input signal into a two-valued function.

Figure 9.3d, on the other hand, shows significant mismatch throughout the series. The square wave generation was carried out with roughly a 78% accuracy, which was much lower than the accuracy of the other tasks. To recreate a straight horizontal line, an infinite series of higher harmonics is necessary in order to satisfy the spectral theorem in the algorithm [13]. Fourier analysis showed that the square wave task was relatively selective in utilizing the higher harmonics to construct the waveform. While the sawtooth and square wave both require an infinite series of sinusoidal harmonics, the square wave requires continuous constructive interference patterns to produce a horizontal line, which limits it to odd or even harmonics and drastically diminishes the regression algorithm. In this case, the ASN was only capable of producing a finite number of higher harmonics. However, further post-processing such as setting a threshold on the voltage to binarize the data can be performed to expand the device's response to a square wave input, a necessity for reliable Boolean logic computing [14].

It was found that the ASN was capable of replicating computing performances typical of reservoirs with 10^3 output signals [15]. Theoretical studies predicts the performance to scale with an increasing number of output signals due to the dependence on the regression algorithm [16]. However, how can a reservoir with much fewer output signals outperform reservoirs with output signals orders of magnitude higher than the ASN? Further inspection of the mathematical formalism [16] show that performance is additionally characterized by the uniqueness of each output signal. Obtaining a set of unique signals allows us to linearly combine the output signals into a number of unique solutions, where the number of unique solutions scales with the number of unique output signals. The larger set of solutions increases the size of the "net" we cast which increases the probability and approximation of producing the correct solution.

9.3 Bibliography

[1] E. N. Oskoee and M. Sahimi, "Electric currents in networks of interconnected memristors," *Phy. Rev. E,* vol. 83, p. 031105, 2011.

[2] G. Z. Cohen*, et al.*, "Second and Higher harmonics generation with memristive systems," *Appl. Phys. Lett.,* vol. 100, p. 133109, 2012.

[3] A. Z. Stieg*, et al.*, "Emergent Criticality in Complex Turing B-Type Atomic Switch Networks," *Adv. Mater.,* vol. 24, pp. 286-293, 2012.

[4] A. V. Avizienis*, et al.*, "Morphological Transitions from Dendrites to Nanowires in the Electroless Deposition of Silver," *Crystal Growth and Design,* vol. 13, pp. 465-9, 2013.

[5] H. Jaeger, *Tutorial on training recurrent neural networks, covering BPPT, RTRL, EKF and the" echo state network" approach*: GMD-Forschungszentrum Informationstechnik, 2002.

[6] B. V. Schrauwen, David; Van Campenhout, Jan, "An overview of reservoir computing: theory, applications and implementations," in *Proceedings of the 15th European Symposium on Artificial Neural Networks.* , 2007.

[7] B. S. F. Wyffels "A comparative study of Reservoir Computing strategies for monthly time series prediction," *Neurocomputing,* vol. 73, pp. 1958–1964, 2010.

[8] L. N. d. Castro, "Fundamentals of natural computing: an overview," *Physics of Life Reviews,* vol. 4, pp. 1-36, 2007.

[9] D. K. Shimeng Yu, H. S Philip Wong, "Design considerations of synaptic device for neuromorphic computing," in *IEEE International Symposium on Circuits and Systems*, Melbourne, VIC, 2014, pp. 1062-1065.

[10] R. A. Dharmendra S. Modha, Steven K. Esser, Anthony Ndirango, Anthony J. Sherbondy, and Raghavendra Singh, "Cognitive Computing," *Communications of the ACM,* vol. 54, pp. 62-71, 2011.

[11] D. V. Benjamin Schrauwen, Jan Van Campenhout, "An overview of reservoir computing: theory, applications and implementations," in *15th European Symposium on Artificial Neural Networks*, 2007, pp. 471-482.

[12] A. G. Jens Bürger, Darko Stefanovic, Christof Teuscher, "Hierarchical composition of memristive networks for real-time computing," presented at the IEEE/ACM International Symposium on Nanoscale Architectures (NANOARCH), 2015.

[13] R. A. Henry O Sillin, Hsien-Hang Shieh, Audrius V Avizienis, Masakazu Aono, Adam Z Stieg and James K Gimzewski, "A theoretical and experimental study of neuromorphic atomic switch networks for reservoir computing," *Nanotechnology,* vol. 24, p. 384004, 2013.

[14] J.-M. R. Karim Gacem, Djaafar Chabi, Arianna Filoramo, Weisheng Zhao, Jacques-Olivier Klein and Vincent Derycke, "Neuromorphic function learning with carbon nanotube based synapses," *Nanotechnology,* vol. 24, p. 384013, 2013.

[15] A. G. David Snyder, and Christof Teuscher, "Computational capabilities of random automata networks for reservoir computing," *PHYSICAL REVIEW E,* vol. 87, p. 042808, 2013.

[16] J. D. Juan Pablo Carbajal, Michiel Hermans, Benjamin Schrauwen, "Memristor models for machine learning," *Neural computation,* vol. 27, pp. 725-747, 2015.

Chapter 10

Parity test for Digital Error Checking

As an illustration of the ASN's utility as a reservoir, the benchmark task of determining bit parity was taken to both measure memory quality and network tenability. As outlined in Furuta [1-2], the task was a fundamental algorithm in signal processing and error checking. Typical data streams of bytes of bits required one bit, the parity bit, to record the parity of the overall byte. Information transfer across multiple servers can corrupt data by inverting one bit thereby changing the overall parity of the data byte. The parity bit ensured identification of corrupted bytes and subsequent repairing to allow for reliable data transfers. Typical data bytes are 8 bits long, which our experiment adapted as time-separated binary pulse sequences.

As such, the reservoir and task needs to be tailored for optimal utility in performing the parity test. Simulations of the ASN was highly leveraged for this purpose for its ease of use, device editing, and high throughput despite statistically underperforming w.r.t. the ASN device. A number of simulations were conducted to determine optimal signal encoding, activation regime, and processing time scales.

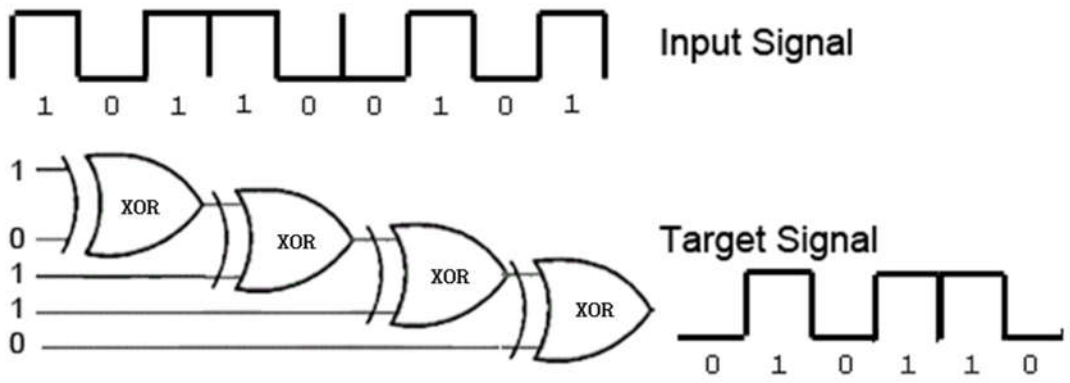

Figure 10.1 Error checking task. Presented is an illustration of the parity check used in data transmission for error checking process. The parity of the number of 1's within a 5 bit byte is evaluated with a sliding window 5 bits wide to generate multiple tasks. The initial input show an odd parity and evaluated as 0 for the desired target signal. As the 5 bit window moves across the signal, the parity changes and reflected in the target signal. The above task was encoded as a voltage pulse sequence into the ASN device where each bit was represented by V_0 or V_1 voltages in a time-separated series. Task complexity increased with increasing number of bits per bytes rather than number of bytes as the check was only executed once per byte.

10.1 Simulated ASN Error-Checking Results

Implementation of machine learning tasks required the design of an encoding technique such that signal transduction stimulates the network into an excited state with the proper mathematical transformation. As outlined in Chapter 3, reservoir computation can be represented into a mathematical design matrix $\hat{O}$ through spectral analysis where its rank and eigenvalue determine the complexity of the transformation [3]. However, reservoir size limits the reservoir's computational capability as the rank of the design matrix cannot exceed the readout layer. This limitation is typically overcome by ensuring overlap of the design matrix within the desired mathematical operating regime by applying constraints to network activity. However, signal transduction can perturb the reservoir outside desired activity and clever design of transduction was required such that the signal can both encode information while maintaining the reservoir at a specific state.

Encoding of digital information was explored by modulating the signal in either the amplitude, frequency, or phase space. For the parity test, digital information was spread among 8

bits with each bit in a binary state of either 0 or 1. Bytes of digital information were represented as pulse voltages, Gaussian wave packets, and phase shifted sine waves for amplitude, frequency, and phase modulation respectively. The binary states 0 and 1 were assigned to preset voltage amplitudes (V_0, V_1), wave packet frequency shifts (f_0, f_1), and phase shifts (φ_0, φ_1) and the Euclidean distance between the binary states empirically optimized. Inspection of the state equation in (3.9) and (5.5) reveals the dependencies of these parameters w.r.t. network activity. Indeed, simulation results concluded that the total voltage was the deterministic factor on reservoir activity while changes in frequency and phase negligibly perturbed the reservoir. An amplitude modulated encoding procedure was adopted for all subsequent experiments with voltages ranging from 0.1 to 7.0 V.

Reservoir activity was initialized in simulations using the resistance training algorithm in Chapter 8 [4]. Resistance values with short convergence times were desired as the resistance training algorithm invariably encoded unnecessary information from the procedure which limited the reservoir's memory capacity. These states coincided with resistance values within R_{ON} or R_{OFF} as well as states that had been thermodynamically stable after repeated approaches. Introducing a highly stochastic signal while maintaining the resistance state was capable of cleansing any information encoded by the resistance training algorithm and was incorporated into a post-experiment protocol. Optimal network activity was determined heuristically while prioritizing reliability over performance.

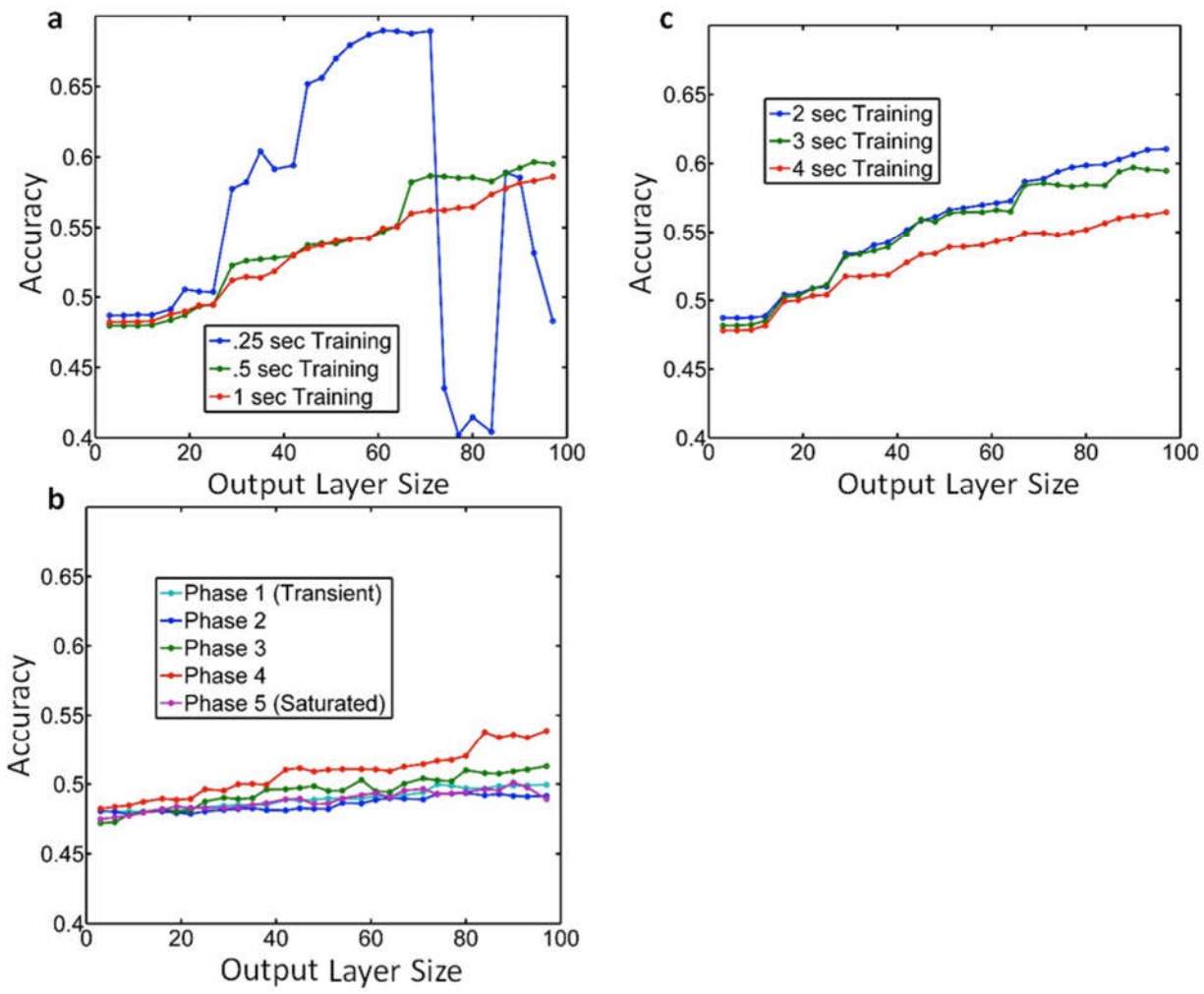

Figure 10.2 Encoding optimization using ASN simulation platform. A simulation of the ASN device performing the parity check task was conducted to determine optimal operating parameters. Temporal memory quality was evaluated w.r.t. the size of the output layer, length of the learning sequence used a, b, and operating time c. Under-learning was observed in a at 0.25 s (blue) length data sets as chaotic performance were measured regardless of network size. Over-learning in b at 4.00 s (red) as continued increase in the data set length reduced reservoir performance. Subsequent phases of operation c each 1.00 s in duration determined optimal operating time. Omitting the transient phase (light blue), subsequent phases monotonically increased performance and peaked at 4.00 s (red) while further operation in phase 5 decreased performance.

A typical proportional–integral–derivative (PID) loop algorithm provided a constant feedback voltage which maintained target reservoir activity. Constant stimulation by application of the driving signal eventually accumulated charge and excited the reservoir outside the target resistance state, observed as LTP in Chapter 7. Conversely, STP dynamics concluded that inactivity or sub threshold voltages unable to counterbalance the thermodynamic inhibitive processes relaxed the system. Stability of the target resistance state was controlled by a PID

feedback loop by dedicating one of the I/O nodes for this purpose. The feedback applied a constant DC signal for an integral time equal to the training time. Maintenance of the resistance state followed identical trends as the resistance training algorithm in section Chapter 7.

Optimal training times were determined by maximizing the dwell times at target resistances and empirically investigated in simulation. Learning was implemented on the reservoir using a number of training data sets, following the mathematics in Chapter 3 and details found in Chapter 13. Each training set was followed by a testing data set to determine the effectiveness of the learning algorithm using the accuracy in equation (3.6) as a metric of success. The procedure of providing a training data set for the learning algorithm and subsequent testing of performance was repeated, while constraining reservoir activity using the PID feedback loop.

The ASN's performance dependencies w.r.t. data set size and number of learning repetition was investigated in simulation to determine optimal dwell times. Simulations of the ASN device revealed an occurrence of under-learning at 0.250 s (Figure 10.2a) and over-learning at 4.000 s (Figure 10.2b). This was observed as drastic increases in the NMSE at these time scales as well as a deterioration of signal propagation. The occurrence of over-learning was theoretically predicted as we approached the network's memory capacity by saturating it with training data. Under-learning manifested as fluctuations in performance across various reservoir sizes due to limited memory retention times. The over-learning occurred as the learning algorithm became ill-posed and over-determined with excessive training sets. Optimum data set lengths were discovered to be 1.000 s while optimal total operating time to be 4.000 s (Figure 10.2c). Subsequent experiments were thus encoded as amplitude modulated data sets 1.000 s in length with 0.250 s pulse width and learning applied within a 2.000 s window.

10.2 Neuromorphic ASN Device Error Checking Results

The optimal parameters found from simulation were implemented on the ASN device and investigated for routes of optimization. Identical instrumentations were used as the resistance training algorithm while incorporating a PID feedback mechanism for sustaining reservoir activity (Figure 10.3a). The error-checking task was implemented over a population 5 devices using all possible permutations of the 16 I/O electrodes and followed similar trends as depicted in Figure 10.3. Initial experimentation on individual ASN devices were performed to determine relevant optimal amplitude and time scales using identical procedures as in simulation. The simulation's predicted optimal parameters were corrected to include amplitude scales of 0.01 – 7.0 V while other parameters were retained.

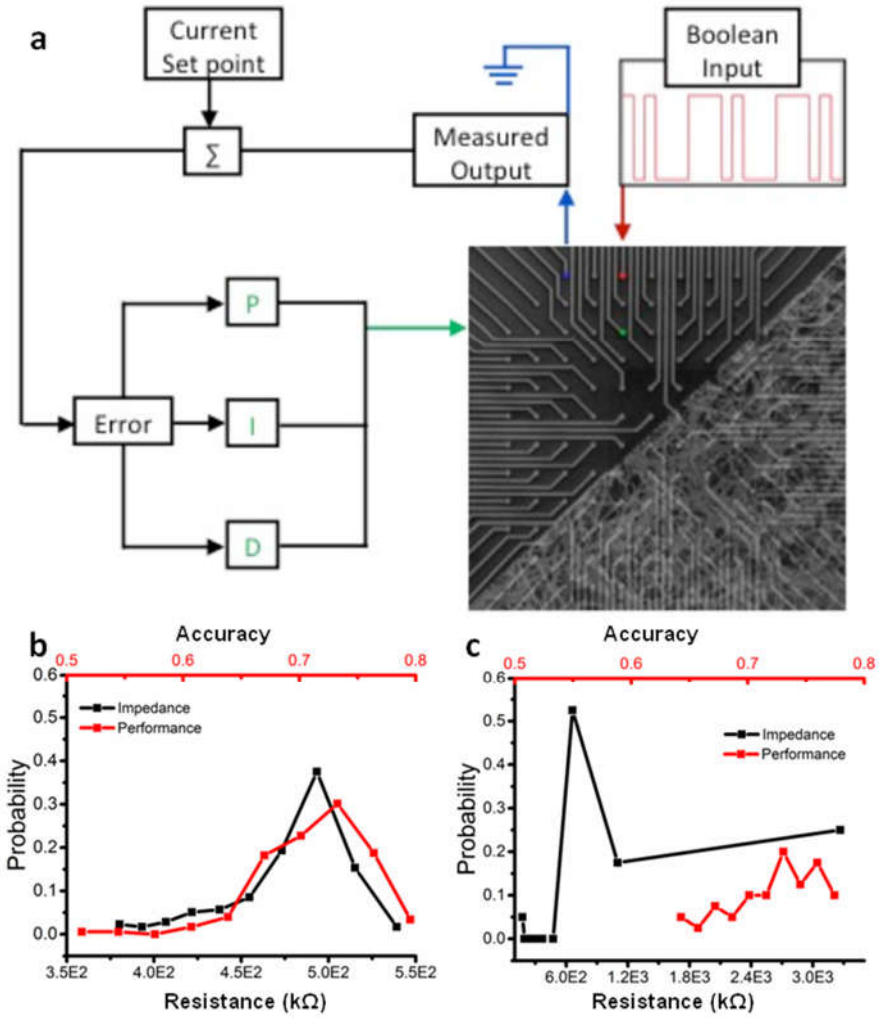

Figure 10.3 Error checking of ASN platform. Schematic of RC using ASN devices: Three I/O electrodes are selected to form the stimulus/control loop for RC: Boolean input streams are delivered to an individual I/O electrode underlying the ASN network (red); a system ground (blue) enables real-time monitoring of current flowing through the network controlled by a feedback-driven bias voltage delivered to (green) a nearby location. The ASN was stimulated with a statistical survey of pulse widths (nΔt) and pulse heights (nΔV) ranging from 250 ms and 0.01 – 7.00 V. Testing occurred immediately after resistance training with a fixed weight configuration. The datasets above achieved accuracies **a,b** between 65% and 78% from ~5,000 trials compared to ~50% from a purely stochastic reservoir.

Device performance and reliability was heavily dependent on the device's resistance state following their description in Chapter 8. Shorter dwell time devices at correspondingly higher resistance states performed with increasing reliability and accuracy, despite implementing similar training and operating times with devices at lower resistance states. A bimodal distribution of metastable resistance states was found with dwell times that exceeded 100 s for 3

different devices that followed similar dynamics to Figure 8.2a. The presence of these metastable states and similar power-law behavior indicated the device activating towards a self-organized critical state [5-6] with the two resistance states centered at 500 kΩ and 600 kΩ possible chaotic attractor states. However, true verification of device criticality required statistical experimentation using exact and identical parameters which proved impractical.

Continued trials revealed devices initialized outside of the near-critical resistance states performed poorly with accuracies below 50%, which prompted subsequent device testing to operate within the bimodal states to explore device optimization. Devices initialized below 500 kΩ (Figure 10.3b) performed at 71.35% ± 6.38% accuracy while those initialized above 600 kΩ attained a similar and maximized performance of 73% ± 5%. Despite seemingly small differences, this trend manifested throughout all trials alongside a characteristic high dispersion in the distribution with kurtosis values of 2.73 and 5.94 for devices at 600 kΩ and 500 kΩ respectively. Kurtosis values beyond 3 indicated a non-Gaussian distribution and increasingly became dominant below 500 kΩ. Rapid bipolar switching manifesting as abrupt changes in current supply was observed below this range and simulation experiments revealed increased filaments forming under similar conditions. The non-Gaussian statistics and filament completion events indicated a shift in the operational characteristics of atomic switches and decreased performance metrics. Consequently, network resistance state became increasingly complex and divergent thereby driving network dynamics towards increasingly nonlinear behaviors and outside target functionality. Past results [7-8] and similar experiments [9-10] clearly indicated the requirement for task-specific network design. Diverging resistance states, dynamic changes in atomic switch behaviors, and poor performance concluded the network was being driven outside of its error-checking design.

Further experimentation evaluating other device parameters such as stimulation amplitude, size, and learning time-scales resulted in minor changes to network performance, highlighting the importance of network dynamics. The stability of the network resistance state was an evident metric in controlling computational capability and network state. Spontaneous organization of 2 convergent resistance states highlights the underlying critical dynamics which maximized device performance. Controlling such device dynamics through the use of mechanisms such as a feedback loop [10] seems evident for further progress.

10. Bibliography

[1] e. a. Taishi Furuta, "Macromagnetic Simulation for Reservoir Computing Utilizing Spin Dynamics in Magnetic Tunnel Junctions," *Phys. Rev. Applied* vol. 10, 2018.

[2] N. B. a. T. Natschl, "Real-time computation at the edge of chaos in recurrent neural networks," *Neural Comput.,* vol. 16, 2004.

[3] D. Verstraeten, "Reservoir Computing: computation with dynamical systems," PhD PhD thesis, Electronics and Information Systems, Ghent University, Gent, 2009.

[4] D. Sellers. (2007, An Overview of Proportional plus Integral plus Derivative Control and Suggestions for Its Successful Application and Implementation Available: https://web.archive.org/web/20070307161741/http://www.peci.org/library/PECI_ControlOverview1_1002.pdf

[5] C. T. Alireza Goudarzi, Natali Gulbahce, and Thimo Rohlf, "Emergent Criticality through Adaptive Information Processing in Boolean Networks," *PHYSICAL REVIEW LETTERS,* vol. 108, 2012.

[6] A. Z. Stieg*, et al.*, "Emergent Criticality in Complex Turing B-Type Atomic Switch Networks," *Adv. Mater.,* vol. 24, pp. 286-293, 2012.

[7] R. A. Eleanor C. Demis, Kelsey Scharnhorst, Masakazu Aono, Adam Z. Stieg and James K. Gimzewski, "Nanoarchitectonic atomic switch networks for unconventional computing," *Japanese Journal of Applied Physics,* vol. 55, 2016.

[8] R. A. Henry O Sillin, Hsien-Hang Shieh, Audrius V Avizienis, Masakazu Aono, Adam Z Stieg and James K Gimzewski, "A theoretical and experimental study of neuromorphic atomic switch networks for reservoir computing," *Nanotechnology,* vol. 24, p. 384004, 2013.

[9] J. D. Juan Pablo Carbajal, Michiel Hermans, Benjamin Schrauwen, "Memristor models for machine learning," *Neural Computation,* vol. 27, pp. 725-747, 2015.

[10] M. B. Michiel Hermans, Thomas Van Vaerenbergh, Joni Dambre & Peter Bienstman, "Trainable hardware for dynamical computing using error backpropagation through physical media," *NATURE COMMUNICATIONS,* vol. 6, 2015.

Chapter 11

T-maze Decision Making

The utility of ASNs was further explored through implementation of the well-known T-maze [1] task described in Figure 11.1. This delayed choice task involves a cue and trigger signal delivered to the ASN, where the cue represents a signal representing 'left' or 'right' that must be remembered and acted upon following the receipt of a subsequent trigger signal. Successful performance of the T-maze task revealed an ability to integrate, segregate, store and respond to external stimulus. These successful implementations indicate great promise for future application of the ASN as a physical platform for RC. Of particular interest are the speed, density, and scalability of the ASN, which in concert serve to overcome major hurdles in the RC paradigm.

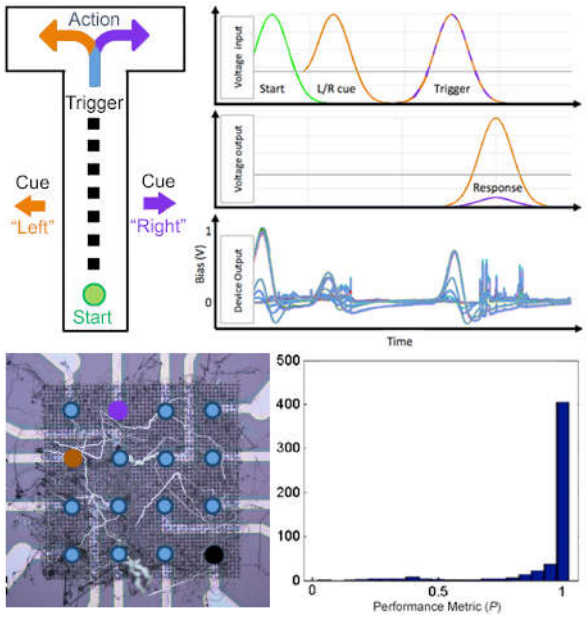

Figure 11.1. T-maze Task. (top) Schematic of the T-maze task alongside a representative sequence of start, cue, and trigger signals delivered to the ASN device during implementation. (bottom) Graphical overlay electrode channel assignments and performance for 500 runs of the T-maze task, where over 93% of L/R decisions were correct.

This RC task, the most challenging of those addressed, represents an extension of those previously described that involved a capacity for integration of information and memory storage by adding a requisite recall function alongside production of an action signal. Initial simulation results exposed a continued trend of maximal performance with increasing number of network nodes presented in Figure 11.1(top). The reconstructed signal successfully reproduced the target with reasonable levels of performance given the limited network size, un-optimized kernel and basic regression method employed as seen in Figure 11.1 (bottom).

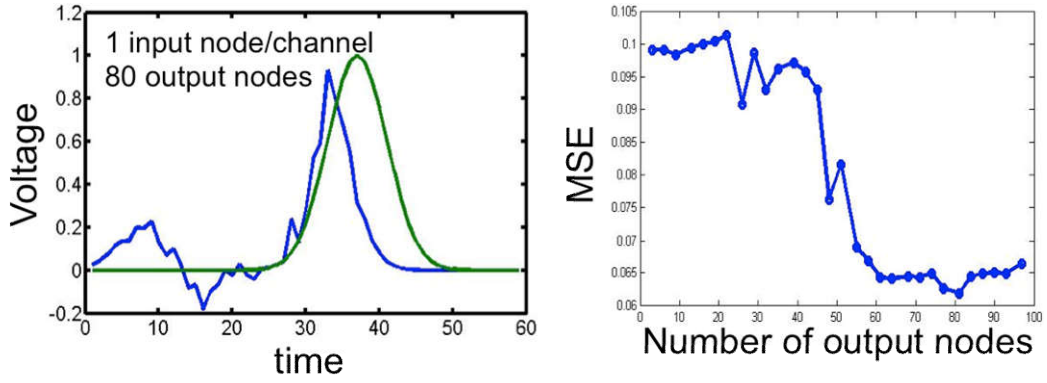

Figure 11.2 T-maze Simulated Results. Mean squared error of task performance decreases with increasing network size. Using the maximum number of nodes achievable, target waveforms were faithfully reproduced in response to a temporally shifted cue/trigger signal.

Implementation of the T-maze task using hardware ASN device was achieved in a 16-electrode configuration as seen in Figure 11.3. Two electrodes were selected to serve as inputs for the left and right signals, delivered in the form of sigmoidal bias pulses in a sequence comprising start/cue/trigger and tested using the simulator. An additional electrode was assigned as ground, or current collector while the remaining 13 electrodes served as nodes/voltage probes to monitor the real-time dynamical response of the network. As a result, output signals represent the linear combination of voltage readings from all 13 nodes/readouts into 2 channels (left/right). Initial success was achieved in the observation of large fluctuations in voltage at the distributed voltage probes following delivery of the trigger signal and in the absence of additional

stimulation, shown at bottom of Figure 11.3. This result indicated energy storage in the ASN device capable of producing the dynamical/echo state property required to execute the T-maze task.

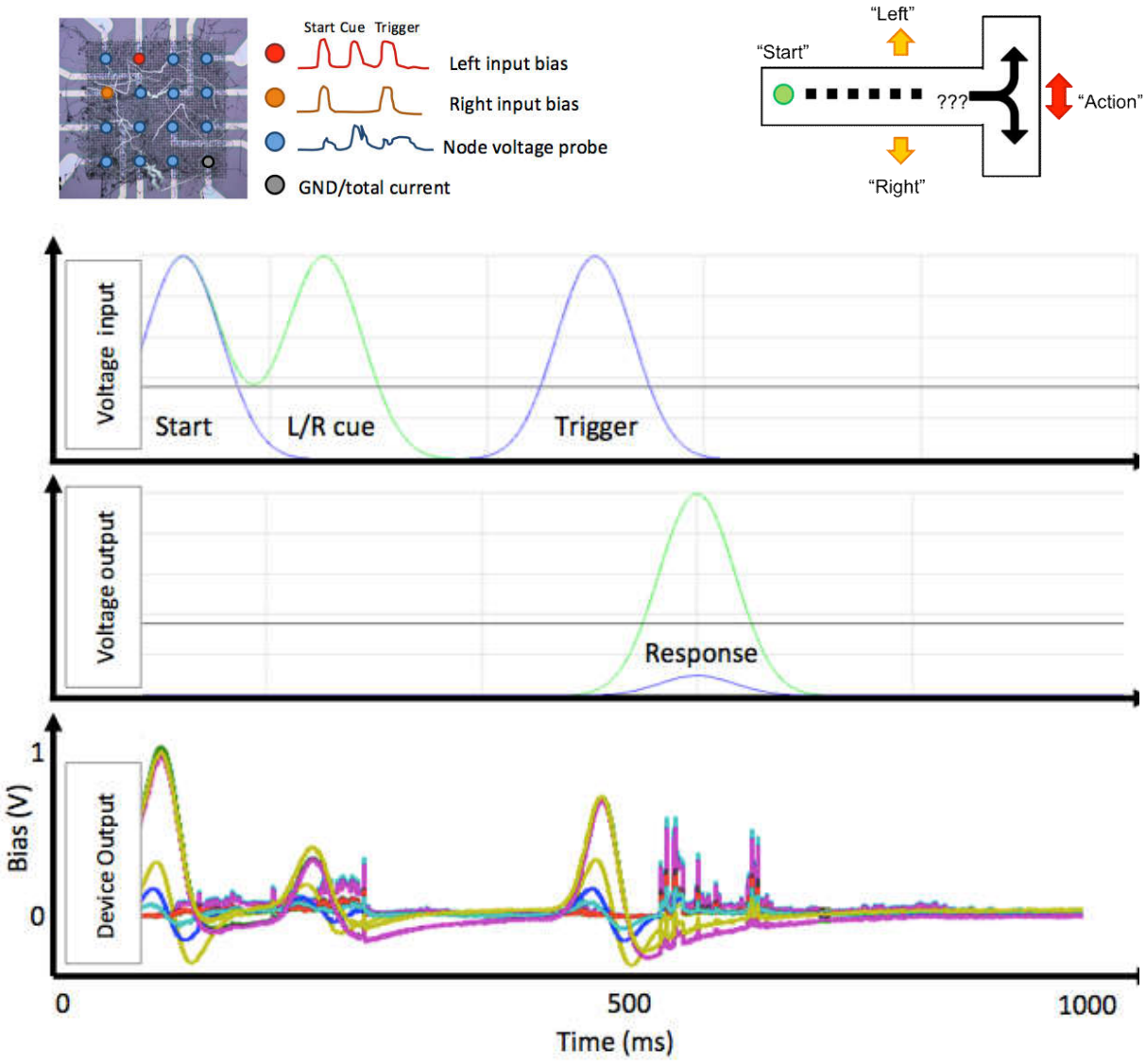

Figure 11.3 T-Maze Task Device Output. ASN device with graphical overlay of electrode channel assignments showing a representative sequence of start, cue, and trigger signal comprising sigmoidal voltage pulses delivered to the network via electrodes (to left) used in implementation of the T-maze task (top left). Representative experimental input (top) target output (middle) and device output (bottom) signals.

Over 500 trials of the T-maze were run using ASN devices, the results of which are summarized in the context of both the individual and combined form of a probabilistic performance metric. Overall, the ASN device performed remarkably well given its form as an un-optimized hardware reservoir and the use of a generic regression algorithm. Upon looking into the details of performance, what can clearly be seen is that when decisions (L/R) are made, they are generally correct (94%). While decisions are only made ~48% of the time, these results do indicate that the distributed reservoir property of the ASN devices can serve as a functional output for this task. Importantly, this reveals that temporal information can be integrated and stored spatially. While further investigation is clearly in order to elucidate the dynamical properties which underlie the ASN's capacity to execute the T-maze in the absence of pre-programming, these results point toward a targeted class of pattern recognition and/or navigation tasks for which the ASN is optimally designed.

11.1 Bibliography

[1] B. S. Eric Antonelo, Dirk Stroobandt, "Mobile robot control in the road sign problem using reservoir computing networks," presented at the IEEE International Conference onRobotics and Automation, 2008.

Chapter 12

Outlook

We concluded that we were able to use network activity and stability via resistance initialization to describe the network state for a thermodynamically driven reservoir, the ASN. Due to the task-specificity inherit in machine learning, it was paramount to characterize and catalogue a reservoir's 'state' that corresponds to task-specific functionalities. Likewise, results in Chapter 9 developed a map for pattern recognition using higher harmonics. Typical reservoir characterization in the literature utilized entropy and Shannon theory, which requires repeated experiments under identical conditions. Current devices utilizing memristor-like reservoirs are difficult to control with such precision, thus, a desire for an alternative characterization of reservoir state has been necessary. In general, characterization of reservoir functionality has proven difficult for real 'edge-of-chaos' systems. Although this requirement has strictly not been within the reservoir computing framework, the development of reservoirs with diverse and rich functionality expands the framework's utility.

Despite limited addressable electrodes, the ASN device was capable of outperforming simulated networks as network complexity, density, and critical dynamics were utilized more effectively in the device. We have presented a clear methodology to implement reservoir computing on a neuromorphic device by developing observable metrics such as power-law behavior, activation of STP/LTP, and resistance state. As outlined in Chapter 3, reservoir performance was theoretically predicted to depend on nonlinear dynamics, network topology, and task design. The commensurate development of simulations aided in implementing theoretical models onto neuromorphic a platform and task evaluation.

Chapter 13

Device Fabrication

With a density controlled network in mind, our group started using electrochemistry to grow a recurrent silver network using copper seeds. Patterned seed networks proved the most versatile fabrication method, and utilized a combination of top-down with bottom-up fabrication, a powerful fabrication method described as nanoarchitectonics. Network growth occurs through an electroless deposition (ELD) reaction through individual atom displacement reactions between Ag^{+} and Cu^{0} based on respective electric potentials. A spontaneous ELD reaction is preferred over an electric one due to the lack of a need for external power and the delicate nature of electrochemical reactions. In this particular case, silver atoms are oxidized while copper is reduced during the galvanic displacement reaction:

$$Cu^{0}(s) + 2Ag^{+}(aq) \rightarrow 2Ag^{0}(s) + Cu^{2+}(aq) \qquad E_{red} = -1.26\ V.$$

Successful implementations of the ELD reaction above allowed us to design a technique using highly patterned top-down photolithography combined with the complex spontaneous growth provided from the reaction above. The ASNs were grown using self-assembly of a rhizomic-dendritic network of highly interconnected silver (Ag) nanowires which were sulfurized to provide distributed nanojunctions comprised of inorganic synthetic synapses. ASNs were interfaced to input-output electrodes fabricated using conventional micro-lithographic processing to create a functional device [1-2] (Figure 13.1a). Electrodes were fabricated by electron beam evaporation following photolithography on the surface of a p-type Si wafer (boron doped, 0-100 $\Omega\ cm^{-1}$) insulated by a 500 nm thick thermal oxide layer. Deposition of 4 to 16 Cr/Pt (15/150

nm) electrodes with diameters of 10 to 50 μm at pitches between 50 and 500 μm was followed by spin-coating and patterning of an insulating layer of SU-8 deep UV resist, which served to expose only point contact regions of the electrodes. Micron diameter cylindrical copper seeds were then deposited at areal densities between $1x10^6$ and $2.5x10^7$ seed sites/cm^2 for the electroless deposition (also referred to as galvanic displacement or cementation) of Ag from Cu on the SU-8 layer. Electroless deposition was performed under diffusion-limited conditions using 50 mM aqueous solutions of $AgNO_3$ [3]. This spontaneous electrochemical reaction produced complex networks of metallic silver nanowires shown in Figure 1b. Previous studies have shown that the geometry and spacing of pre-patterned Cu posts provides control over the global qualities of the network generating structures ranging from extended nanowires to dendrites and fractals [4-5]. The pitch of the Cu posts was found to determine the relative density of the network (Figure 12.1c, d) while seed size was used to control the presence of long-range connections. Typically, smaller Cu seeds (<3.5 μm) produce many long wires and larger seeds (>3.5 μm) produce spatially confined dendritic or fractal structures.

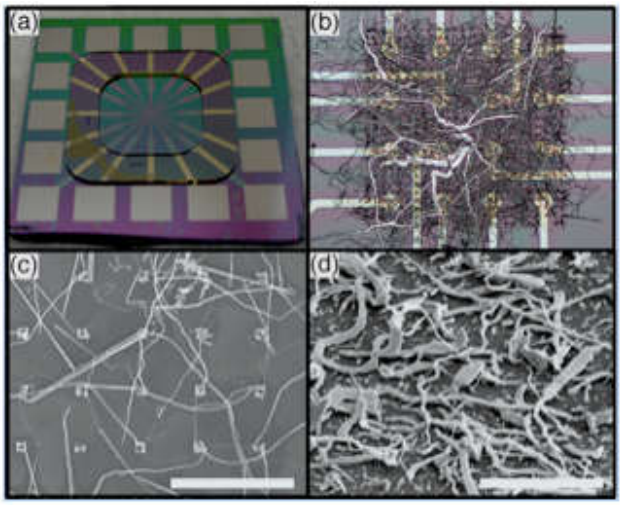

Figure 13.1 Atomic Switch Network Fabrication. a) Atomic switch network devices were fabricated on a SiO_2 substrate with 16 Pt electrodes and an insulating SU-8 layer. Devices are approximately 4 cm^2. b) Resultant Ag wires vary in size (<100 nm to >1 mm) and create self-assembled networks with complex interconnections (10^9 cm^{-2}). Electrodes shown have 10 μm diameter and 50 μm pitch, and range up to 50 μm diameter with 500 μm pitch. c-d) The density of interconnections can be changed by altering the size/pitch of the Cu posts shown c) 1 μm/5 μm d) 1 μm/1 μm. Scale bars = 10 μm.

The self-assembled silver networks intrinsically contain crossbar-like junctions resulting from the three-dimensional nature of the solution deposition process. Upon exposure to sulfur gas [6] (10^{-1} torr at 130 °C for 3 min), the Ag nanowire junctions are functionalized to form thin Ag|Ag_2S|Ag metal-insulator-metal interfaces which, in the presence of post-processing activation with external bias potential, are transformed into "atomic switches". Electrical characterization of the devices was conducted through current-voltage (I-V) spectroscopy using a bipotentiostat (Pine Instruments model AFCBP1) in conjunction with either a data acquisition module (National Instruments USB 6259) or a multiplexed (National Instruments PXI 1073) source-measurement unit (National Instruments PXI 4130). The maximum bandwidth of the measurement systems is 1 MHz and 10 kHz enabling 2 Ms and 20 ks per second with 16-bit resolution. Subsequent data analyses were carried out using MATLAB 2010b (MathWorks) and Origin 8.1 (OriginLab Corporation).

13.1 Reservoir Computing Implementation

All reservoir experiments were conducted on an 8x8 grid containing an estimated 10^8 atomic switch junctions using the 64 electrodes as I/O interface layers. A single electrode was selected to inject the electrical input signal, while another electrode was chosen as the counter electrode as shown in Figure 10.3a. The control signal delivered a feedback voltage to an electrode in proximity to the input electrode. Voltage signals were simultaneously measured from the remaining 61 electrodes using the data acquisition module (National Instruments USB 6259). Reservoir computing was implemented following the mathematics presented in section 2 with the input layer consisting of only the input electrode and the output layer constructed from the 61 measuring electrodes.

When first designing a purpose-built device to emulate mammalian brain activity, dendritic silver structures were desired. However, over time it was realized that the connections provided by these structures were unreliable and difficult to reproduce. Through changing the size of the copper posts, a morphological transition was found showing that a seed site of 1x1 μm^2 up to 3x3 μm^2 leads to fine nanowires. Seeds between 3x3 μm^2 and 10x10 μm^2 yield a mixture of nanowires with branched dendritic structures, while posts larger than 10x10 μm^2 produce only dendrites.

13.2 Bibliography

[1] A. Z. Stieg*, et al.*, "Emergent Criticality in Complex Turing B-Type Atomic Switch Networks," *Adv. Mater.,* vol. 24, pp. 286-293, 2012.

[2] A. V. Avizienis*, et al.*, "Neuromorphic Atomic Switch Networks," *PloS one,* vol. 7, p. e42772, 2012.

[3] A. Kuhn*, et al.*, "Structural Analysis of Electroless Deposits in the Diffusion-Limited Regime," *Phys. Rev. Lett.,* vol. 73, pp. 2998-3001, 1994.

[4] O. Shochet and E. Ben-jacob, "Coexistence of Morphologies in Diffusive Patterning," *Phys. Rev. E,* vol. 48, pp. 4168-R4171, 1993.

[5] A. V. Avizienis*, et al.*, "Morphological Transitions from Dendrites to Nanowires in the Electroless Deposition of Silver," *Crystal Growth and Design,* vol. 13, pp. 465-9, 2013.

[6] M. Kundu*, et al.*, "Effect of sulfurization conditions and post-deposition annealing treatment on structural and electrical properties of silver sulfide films," *J. Appl. Phys.,* vol. 99, pp. 103501-9, 2006.

Chapter 14

Design Optimization of the ASN

Directed nanowire growth to create dendritic structures followed diffusion limited aggregation with Mullins-Sekerka instabilities. For sparse concentrations of $AgNO_3$, diffusion-limited aggregation (DLA) dynamics prevail where Ag^+ cations displace Cu^0 atoms in discrete non-interacting reactions. Reduced silver atoms accumulate on the surface of the copper posts and develop, in a steady-state evolution, metallic nanostructures. Solidification of silver particles undergoing DLA obeys the mathematical formulations of Fick's Law, modified by Mullins-Sekerka instabilities which describe pattern formation of accumulated metal nanostructures. We describe the kinetics of formation using ion clusters to describe the heterogeneity of the solution's concentration. Clusters of ions diffuse through the solution, creating a wave of ions that initiate the ELD process at the seed. Starting with Fick's law to describe the diffusion:

$$D_{Ag}\nabla^2\mu_{Ag} = \frac{\partial\mu_{Ag}}{\partial t};\ D_{Cu}\nabla^2\mu_{Cu} = \frac{\partial\mu_{Cu}}{\partial t}; \tag{14.1}$$

Here we use D_{Ag} and D_{Cu} as the diffusion constants for $AgNO_3$ and pure copper respectively with as the diffusion potential. As the wave front of silver reacts with copper, aggregated silver atoms at the seed sites accumulate, pushing the growth front towards the wave front. The solid-liquid interface perturbs the diffusion field, moving slowly and continuously renormalizing the ion gradient in solution.

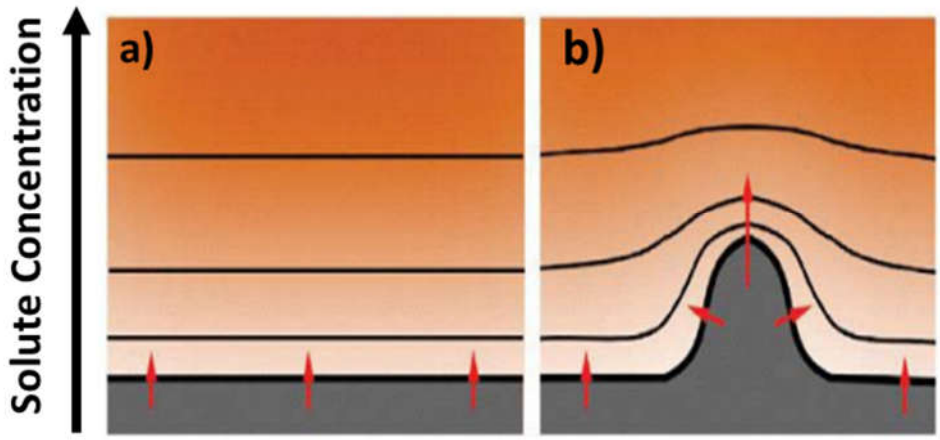

Figure 14.1 Schematic of Diffusion Limited Growth. An initially planar seed site (grey area) is presented in a) where a diffusion gradient initiates unidirectional growth, red arrows, towards areas of higher solute concentration, represented by black horizontal lines. Growth of the seed site extends site towards high solute concentration but are restricted in b) by the diffusion gradient due to localized fluctuations in concentration creating depletion regions. The distended seed site expands multi-directionally according to the continuity equation.

Growth of the solid-liquid interface, via the non-equilibrium process of electroless deposition, is mediated by the continuity equation:

$$Mv_n = \left[\delta\mu_{Ag} D_{Ag} \nabla\mu_{Ag} \quad \delta\mu_{Cu} D_{Cu} \nabla\mu_{Cu}\right] \hat{n}\,. \tag{14.2}$$

The miscibility gap, M, and the normal velocity, v_n, of the interface, determine the population exchange during single displacement reactions with $\delta\mu_{Ag}$ as the fluctuation in chemical potential due to concentration heterogeneity.

Growth of the solid-liquid interface results in the Mullins-Sekerka instability which is due to competing dynamics between steady silver nanostructure growth and dynamical expansion of the growth front. Once the rate of metal nanostructure growth exceeds the diffusion rate, a depletion region emerges that no longer contains enough silver atoms for sustainable displacement. Regions adjacent to the initial growth front contain sufficient ion concentration to participate in ELD, forming side branches. Depending on the rate of formation, the chemical potential at the interface is described by the Gibbs-Thomson boundary condition:

$$\mu(r_0) = \quad d_0 \varepsilon\,. \tag{14.3}$$

Here, the chemical potential at the interface, $\mu(r_0)$, is dependent on the surface curvature, ε, and d_0 the characteristic length of the seed. In the simplest case, the value of equation (14.3) was approximated to be the value of equation (14.2) during equilibrium. The non-equilibrium process at the solid-solution interface determines a characteristic capillary length scale, d_0:

$$d_0 = \frac{\gamma}{M}. \tag{14.4}$$

Where γ is the surface tension. Solutions to equations (14.1) thru (14.4) for a planar interface with small perturbations in ionic concentrations are solved in [1]. Extending this model for multiple perturbations will show dendritic growth that we experimentally demonstrate in controlled fabrication of the ASN. Equations (14.3) and (14.4) show parameters of control over the morphology of seed-directed nanowire growth.

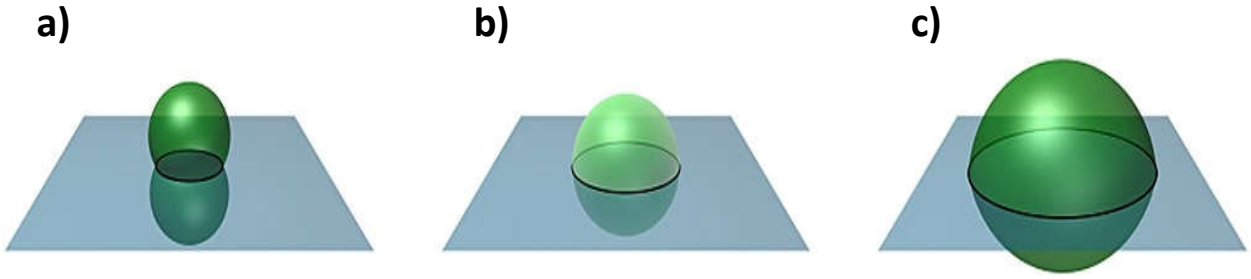

Figure 14.2 Schematic of Depletion Regions due to Varying Chemical Capillary Lengths. High surface tension in **a)** produces a small capillary length and small depletion region between the solution (green) and substrate (blue). Increasing capillary lengths produces in **b)** a larger depletion region than in **a)** and **c)** depicts a hydrophilic substrate where the capillary length is largest.

The reactivity dependence on curvature can been controlled by varying shape, size, and pitch of copper seeds. Surface tension and miscibility gap can be controlled through varying the copper spacing and distribution. Understanding DLA under Mullins-Sekerka instability conditions provides control and reproducibility over self-organizing nanowire networks. Pattern formation due to Mullins-Sekerka instabilities presented here is a linear approximation of the dynamical behavior of dendrite formation. Experimental testing confirmed in Figure 14.3 that when the size

of the copper seed is on the order of 1-5 microns Mullins-Sekerka instabilities are suppressed, and the growth of metallic nanowires continues without nucleation of side branches.

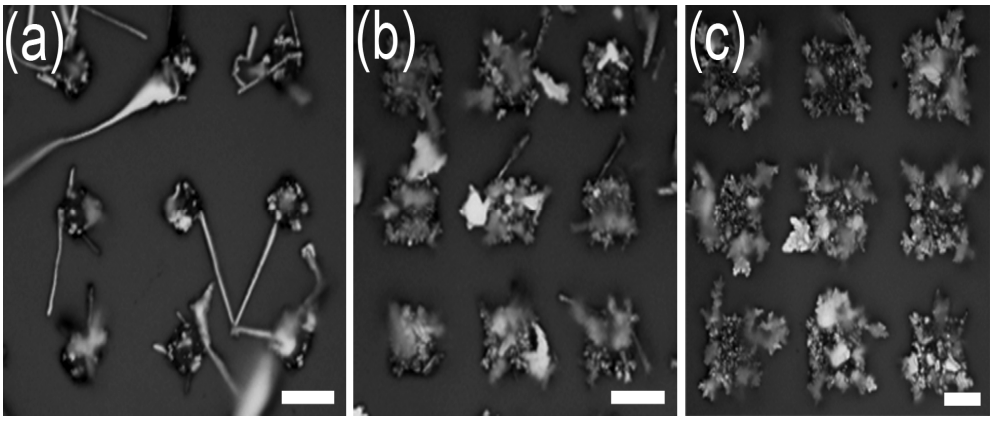

Figure 14.3 Optical Micrographs of Dendrite Growth as a Function of Cu Seed Size. At 7 μm **(a)** wires predominate, with branched structures appearing as **(b)** seed size is increased to 9 μm. **(c)** Wires were not observed for deposits from 15 μm seeds. Scale bars = 10 μm.

In order to explore the concept of fabrication through self-organization, the mathematical principles of diffusion limited aggregation (DLA) and ELD are combined to guide a nanoarchitectonics approach using the electroless deposition of silver. An extensive experimental study of this fabrication method found that the critical parameter for the growth of nanowires was the size of the copper seed post which is theoretically predicted in equation (22) due to the factors of surface curvature and surface tension [2]. The diverse wire lengths included long-range and short-range atomic switches, facilitating both globally and locally distributed patterns of switching activity in the ASN. Due to the variation in nanowire diameters, we infer each junction to have a variable gap size and subsequent atomic switch size, thereby increasing the number of available resistance states to the ASN [3-4]. This fabrication method offers control over network density and structure by introducing two important parameters: seed size and spacing, which nucleate wire growth.

14.1 Bibliography

[1] J. S. Langer, "Instabilities and pattern formation in crystal growth," *Rev Mod Phys,* vol. 52, 1980.

[2] C. M.-O. Audrius V. Avizienis, Henry O. Sillin,Masakazu Aono, James K. Gimzewski, and Adam Z. Stieg, "Morphological Transitions from Dendrites to Nanowires in the Electroless Deposition of Silver," *Crystal Growth & Design,* vol. 13, 2013.

[3] A. V. Avizienis*, et al.*, "Neuromorphic Atomic Switch Networks," *PloS one,* vol. 7, p. e42772, 2012.

[4] A. Z. Stieg*, et al.*, "Emergent Criticality in Complex Turing B-Type Atomic Switch Networks," *Adv. Mater.,* vol. 24, pp. 286-293, 2012.

Chapter 15

Polymer Nanocomposites

Here we aim to develop additional functional nanomaterials which integrate memory and information processing capabilities. Building upon prior work using metal-insulator-metal interface materials for neuromorphic hardware, we constructed and assessed hardware-adaptive computing devices using inorganic, encapsulated, and polymeric nanomaterials. New materials 8 developed by Kaner was integrated with existing device platforms (Chapter 13) to enable characterization to investigate salient properties such as structural, electrical, and functional properties via scanning probe and electron microscopy, conductive probe microscopy, and multielectrode array measurement systems. Characterization efforts support materials optimization based upon: volatility, frequency response, operational voltages/currents, reproducibility, and processing conditions. The goal of this task is to generate a memristive polymer hybrid system categorized in terms of functional materials parameters relevant to the construction of application-specific reservoirs.

15.1 Silver Decorated Polyaniline Synthesis

Polymer hybrid materials are distinguished by their flexibility—literal and figurative. They are mechanically soft, structurally tunable and can be incorporated into devices using back-end encapsulation processes [1]. Polyaniline (PANI) acts similar to a metal, conducting through conjugated π-electrons in its protonated emeraldine oxidation state. Hybridizing PANI with metal nanoparticles allows the memory time to be tuned based on the amount of charge retained by the nanoparticles and their degree of coupling to the polymer backbone [2-3].

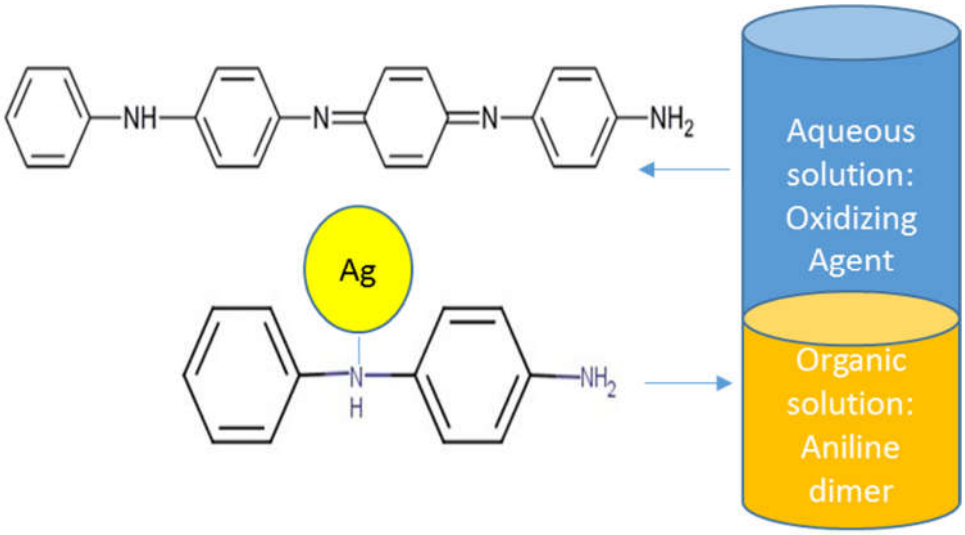

Figure 15.1 Synthesis of Ag decorated polyaniline. An initial organic solution of aniline dimers (yellow) was treated with $AgNO_3$ as an oxidizing agent. Disassociation of $AgNO_3$ to its constituent ions Ag^+ and NO_3^- allowed Ag nanoparticles to form at the N-H bond (schematic). Polymerization of the aniline dimers into its emeraldine redox state prompted the encapsulation of Ag nanoparticles. The resulting nanocomposite is suspended in an aqueous (blue) solution which was extracted using microfiltration.

Synthesis of PANI decorated with metal nanoparticles is prepared by a redox reaction of PANI with the metal anions of the oxidizing agent. For gainful comparison between our work with atomic switches and decorated PANI, $AgNO_3$ was selected as the oxidizing agent and synthesized as a nanocomposite nanofiber following previous work by Kaner [4]. An initial solution of an aniline dimer was produced in 18.2 MΩ ultra pure water and polymerized with a 50 mM solution of $AgNO_3$ to introduced Ag nanoparticles at the N – H bond, producing PANI-Ag. A molar ratio of $AgNO_3$/PANI of ~1.0 in solution was used to ensure production of nanocomposites. Concentrated PANI-Ag was recovered with microfiltration (0.45 μm membrane, Millipore) and washed with NaOH and DI water. Subsequent functionalization using 1.0 M HCl to the PANI solution doped the PANI-Ag to its emeraldine salt. Characterization of the product using X-ray photoelectron spectroscopy (XPS) confirmed the bulk presence of conductive emeraldine state and a shifted N peak coincided with the expected shift of an attached nanoparticle. Topological characterization using scanning electron microscopy confirmed the production of nanofibers with areal dimensions of ~20 nm diameter and lengths of ~1 μm.

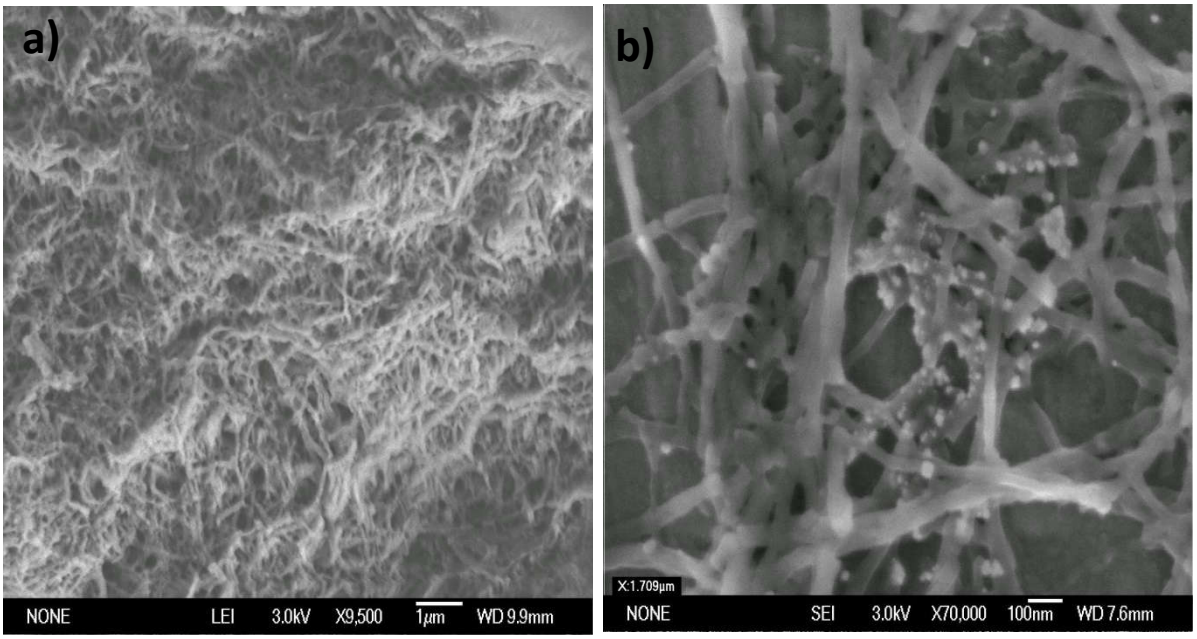

Figure 15.2 Scanning Electron Images of Synthesized PANI-Ag. Drop casted samples of PANI-Ag on Al substrates was imaged in **a)** to reveal high coverage of dispersed nanofibers. Nanofiber dimensions was measured from image **b)**, with the diameter uniformly measuring ~20 nm and lengths up to 1 μm

15.2 Bibliography

[1] D. J. Cardin, "Encapsulated Coducting Polymers," *Adv. Mater.,* vol. 14, 2002.

[2] R. W. K. B. J. Gallon, R.B. Kaner, P.L. Diaconescu "Palladium Nanoparticles Supported on Polyaniline Nanofibers as a Semi-Heterogeneous Catalyst in Water," *Angewandte,* vol. 46, 2007.

[3] J. H. R. J. Tseng, J. Ouyang, R. B. Kaner, Y. Yang, "Polyaniline Nanofiber/Gold Nanoparticle Nonvolatile Memory," *Nano. Lett,* vol. 5, 2005.

[4] C. O. B. R. J. Tseng, B. Shedd, J. Huang, R. B. Kaner, J. Ouyang, Y. Yang, "Charge transfer effect in the polyaniline-gold nanoparticle memory system," *Applied Physics Letters* vol. 90, 2007.

Chapter 16

Electrical Characterization of PANI-Ag

The electrical properties of the nanocomposite was investigated using probe microscopy to determine nanoscale characteristics. Bulk Au decorated PANI was previously shown to achieve conductance switching using a 2-terminal electrode measurement unit [1]. Implementation of PANI-Ag nanofibers as a neuromorphic devices requires the active material to operate on a similar size scale as the ASN. Individual nanofibers at the ~10 nm scale are theoretically predicted to experience quantum confinement similar to nanowires and quantum dots. Conductive atomic force microscopy (cAFM) was capable of characterizing nanoscale characteristics of a PANI-Ag film deposited on a Pt coated Si(111) substrate.

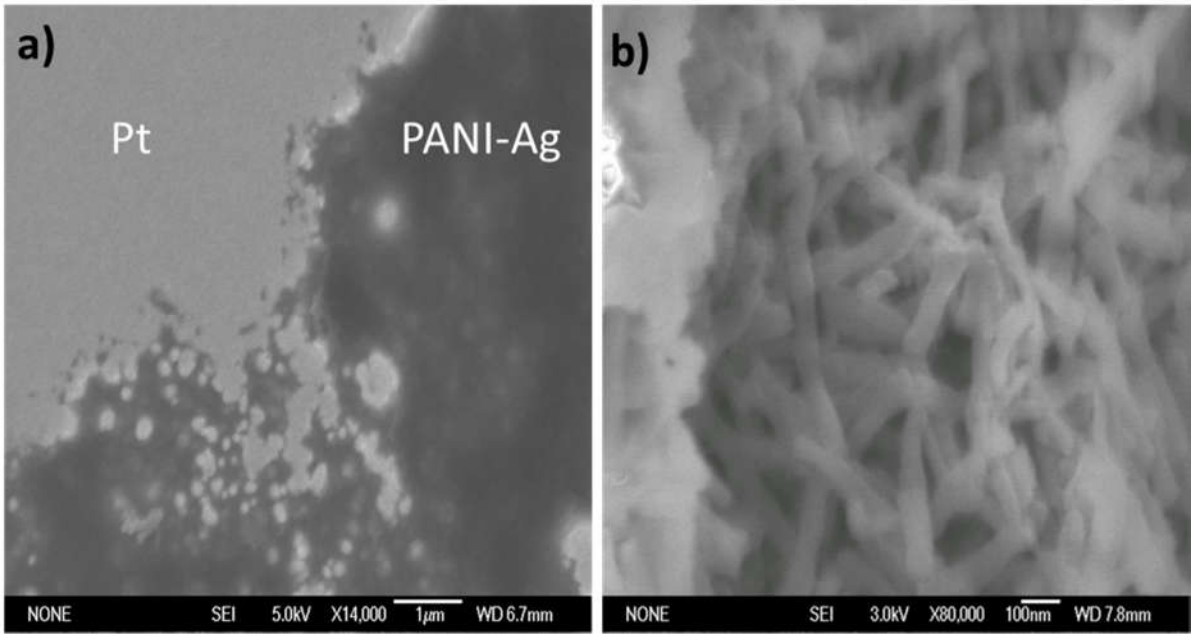

Figure 16.1 SEM Images of Electrospray Deposited PANI-Ag. Deposition of PANI-Ag using an electrospray system resulted in a uniform film of the nanocomposite with a characteristic perforated topology. Magnification in **b)** show condensed bundles of nanofibers and subsequent dimension measurements yielded nanofibers diameters of ~20 nm and lengths ~120 nm.

Preparation of the nanocomposite PANI on a conductive substrate for cAFM was achieved using electrospray deposition technique. The Pt-Si substrate was prepared by electron beam deposition (CHA Mark 40) of an Pt target to fabricate a 100 +/- .2 nm thick layer on a Si(111) substrate. A 10 mL nitrogenated solution of PANI-Ag was electrosprayed onto the substrate with a 3 kV bias and a nozzle rate of 12 uL/min. A separation of ~3 cm was maintained between the nozzle and substrate as the nozzle mechanically scanned across the substrate. Subsequent measurement using a Dektak 3030 profilometer revealed a PANI-Ag film with a ~20 nm thickness and ~120 nm length.

16.1 Characterization of PANI-Ag via cAFM

Topological cAFM imaging revealed ~2 nm bands of highly conductive PANI-Ag within the nanofibers. A positive 1.0 V bias was applied to the sample during image scan using a Bruker Dimension Icon Microscope. Figure 16.2 details the height topography of electrospun PANI-Ag forming bundles of nanofibers with similar size distributions found in SEM images in Figure 16.1b. Maximum distinguishable feature sizes was limited by tip apex deconvolution to ~15 nm and unable to topographically resolve the same features as Figure 16.1a. Cross correlation with the electric density map was able to enhance image contrast and resolve ~2 nm features. Figure 16.2b presents the the electric density topography corrected by cross-correlation using the height topography. High conductive regions were found within the nanofibers distributed as ~2 nm localized spots. Previous work by Kaner [1] show coincidental similar size distribution and topology characteristic of the decorating metal nanoparticle. Identification of the highly conductive ~2 nm regions were inconclusive using current-voltage and force spectroscopy due to highly coupled interactions between the tip apex and surrounding polymer material. Structures resembling islands are composed of highly insulating regions surrounding nanofiber bundles.

Characteristic sharp peaks in the insulating region indicate an overall structural and chemical departure from the PANI-Ag nanofibers. Subsequent reverse sweeps and inverted polarity experiments suggest these region are anomalous large gaps between nanofibers, with the negative current density comparable to Nyquist noise.

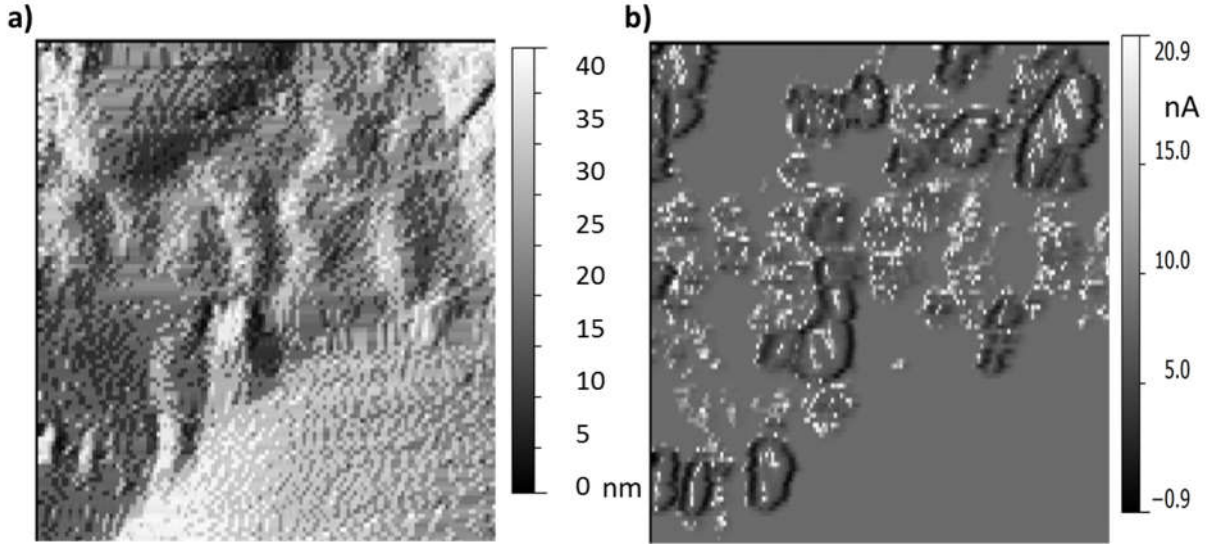

Figure 16.2 Height and Current Topography of PANI-Ag from cAFM. Height measurements in contact AFM in **a)** are unable to resolve the nanofiber structure due to the highly attractive potential in polymer systems. Deconvolution of **a)** from the current density topography is shown in **b)** which outlines the nanofiber structure as perforated white structures. Dark ridges surrounding the nanofibers indicate formation of nanofiber bundles.

The PANI-Ag nanofibers were observed to achieve current densities within the bounds of the leucoemeraldine redox state. Reported literature values of emeraldine PANI sheet resistance ranges within ~10^3 Ω/cm^2 from π-π stacking within the phenyl groups [2]. The introduction of electron rich nanoparticles enhanced charge carrier dynamics between the metal nanoparticle and the conjugated phenyl groups. Observations of decreased sheet resistance ~10^2 Ω/cm^2 while in the emeraldine state and ~10^4 Ω/cm^2 in the leucoemeraldine state. Direct measurement of PANI-Ag nanofibers via cAFM achieved a leucoemeraldine sheet resistance of ~10^4 Ω/cm^2 as calculated from a 21.0 nA collector current and ~15 nm spot size. Subsequent investigation of the emeraldine state via bias induced switching were attained using cAFM. Full contact between

the AFM probe and PANI-Ag nanofiber and increasing sample bias to 2.30 V resulted in increased sheet resistance on the order of ~10^2 Ω/cm^2. Continuous application of bias sweeps up to 2.30 V slowly increased current density until the PANI-Ag was partially oxidized at 2.26 V and transitioned into the emeraldine. Here, the nonconjugated C-N bond in the initial leucoemeraldine switched to a conjugated C=N emeraldine state, facilitating charge donation from the metal nanoparticle and the charge transfer process. Additional voltage sweeping towards the negative polarity (1.70 V) partially reduces the film and inhibited the C=N bond while decreasing the current density. Reverse switching was unattainable due hardware limitations.

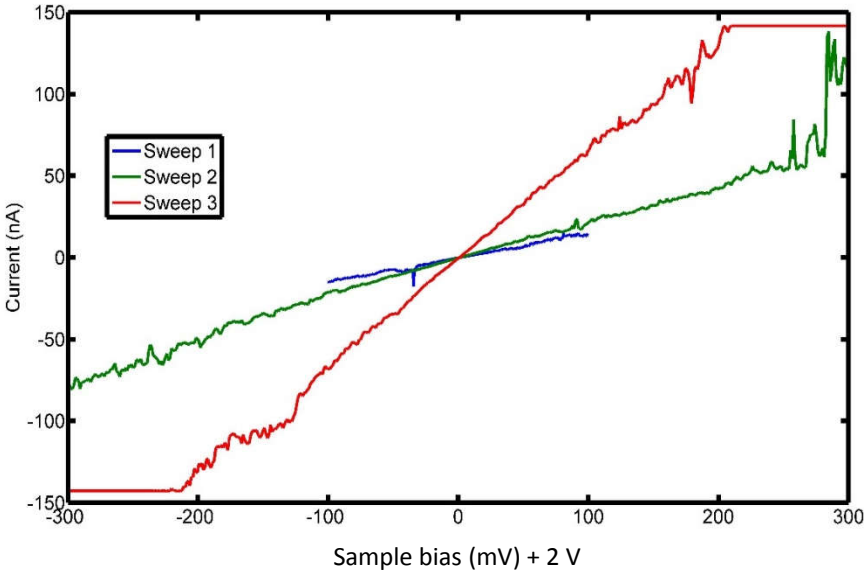

Figure 16.3 Voltage Bias Sweeps in cAFM. The AFM probe was held at full contact at a single location on PANI-Ag film. An offset 2.0 V voltage was applied while incrementally sweeping the voltage an addition +/- 300 mV. Cyclic sweeping slowly increased overall conductance before an abrupt increase at 2.26 V, indicative of the transition into the emeraldine state.

16.2 Conclusion

Polymer nanocomposites were synthesized and characterized to determine the tenability of PANI-Ag nanofibers towards neuromorphic computing. Facile synthesis and similar

topological, and electrical characteristics with the atomic switch network enlist the system as a promising candidate. Additionally, the general tunability of polymer nanocompsites enables the PANI-Ag system to explore alternative stimulation and information transmission options. The redox switching process is inherently sensitive to the chemical environment, specifically volatile organic compounds and pH environment [3]. By using a similar construction of theory and constraints as the ASN, computation through direct transduction of chemical information enable the system to physically compute within redox states, rather than digital “0” and “1” states. However, further studies are required to meticulously map the switching mechanism and determine an equivalent mathematical transfer function. Due to the volatility and exposure required in cAFM studies, alternative techniques must be adopted to characterize localized nanoscale dynamics.

16.3 Bibliography

[1] C. O. B. R. J. Tseng, B. Shedd, J. Huang, R. B. Kaner, J. Ouyang, Y. Yang, "Charge transfer effect in the polyaniline-gold nanoparticle memory system," *Applied Physics Letters* vol. 90, 2007.

[2] X. W. Z. Yang, Y. Yang,Y. Liao, Y Wei, X. Xie, "Synthesis of Electroactive Tetraaniline PEO Tetraaniline Triblock Copolymer and Its Self-Assembled Vesicle with Acidity Response," *Langmuir,* vol. 26, 2010.

[3] S. V. J Huang, BH Weiller, RB Kaner., "Nanostructured polyaniline sensors," *Chem. Eur. J.,* vol. 10, 2004.

Chapter 17

Piezoelectric needle sensor reveals mechanical heterogeneity in thyroid tissue lesion

The utility of nanotechnology afforded us opportunities to directly apply our neuromorphic studies towards common use, specifically medical practices. Identification of principle parameters that characterizes both nanoscale and mesoscale dynamics was facilitated by extending probe microscopy models to biopsy procedures. Here, needle biopsies sample tissue *ex vivo* for cytological analysis. In conjunction with existing bioinformatic models we developed a biopsy transducer which characterizes holistic systems, i.e. *in vivo* tissues, for both bulk and local mechanical properties. Tissue stiffness and stiffness heterogeneity provide cytological indicators for variant tissue strains.

17.1. Background

Increased tissue stiffness is a widely accepted and actively studied biomechanical property of fibrotic tumors and has been linked to several hallmarks of cancer, including growth, metabolism, invasion and metastasis[6-8]. Evaluation of a thyroid nodule remains one the most common and yet one of the most challenging problems for endocrinologists. Thyroid nodules are common with ~ 1% of males and 5% of females having palpable thyroid nodules [1]. Among these, a majority (> 90%) of the thyroid nodules are non-malignant or well-differentiated papillary and follicular carcinomas [2]. Nevertheless, the remaining ~10% of cases may cause significant morbidity and eventually death. Thus, the clinical importance of thyroid nodules rests with the need to exclude thyroid cancer. The standard diagnostic modality of evaluating malignancy in thyroid nodules involves ultrasound coupled with fine needle aspiration cytology

(FNAC) primarily to prevent unnecessary surgeries for benign conditions or avoid missing malignant nodules [3]. However, the overall false negative rates (malignant histology of a nodule with benign cytology) for FNAC ranging from <1 to 12% [4-5], and indeterminate cytological findings, warrant the need for new methodologies to improve diagnostic sensitivity and accuracy of thyroid FNAC.

Biomechanically, thyroid lesions exhibit inhomogeneous elastic behavior as a consequence of collagen in the stroma and frequent calcium deposits[9]. Such regions vary by orders of magnitude in stiffness behavior from healthy cells[10], and hence vary in haptic feel. However, rapid and quantitative methods for measuring tissue stiffness that can be translated into clinical settings have not yet been established. Elastography has yielded promising results in diagnosis of breast [11-15], liver [16] and pancreatic lesions [17-18] though histological confirmation remains the treatment standard.

Needle based sensors provide greater access to specific bio-component contributions in tissue mechanics[19] and bridge the gap between cellular and tissue level measurements at high spatial resolution (e.g., different tissue planes or variations of densities within the tissues). Needle-tissue interactions have been previously attempted to guide tumor navigation, but it is difficult and expensive to micro-fabricate the piezo-sensor (<100μm) used inside a hollow needle[19]. The Hansma group used a reference probe technique to measure mechanical properties of normal and diseased soft and hard tissues in vivo and in vitro[20]. But the technique, mostly employed to measure bone material properties had limited measurement range (<600 μm) and the spatial resolution in the mm scale (0.2-2 mm). A combined micronewton-resolution, tensiometric force probe and micromanipulator was used to measure the variation in tissue stiffness (100 μm to mm scale)[21]. However, the thickness of the samples that can be

accurately measured significantly limits applicability. Previous studies probed the nature of FNA needle penetration during thyroid FNA biopsy for cancer biomarkers [22-23] but yielded only qualitative tactile assessment of nodule stiffness using their fingers resulting in operator bias, and lack of quality control. Thus, there remains an urgent and unmet need for new and quantitative technologies to detect and profile solid tumors such as thyroid lesions, based on their biomechanical characteristics.

Here, we introduce the use of a simplified piezoelectric needle sensor to measure thyroid tissue stiffness at unprecedented cellular scale resolutions. To the best of our knowledge, this is the first quantitative biomechanical report on stiffness heterogeneity of thyroid lesions. Unlike, other commonly used single cell based biomechanical techniques such as the micropipette aspiration[24] and atomic force microscopy[25-26], our 'smart-touch fine needle' (or STFN) is a low cost method that enables quantitative real-time biomechanical analysis of thyroid tissues within the cellular microenvironment. The technology is about ten times finer than diffraction limit of Ultrasound, Magnetic Resonance Imaging or Computer Tomography, bridging size scales from cell, tissue and organ level to reveal distinct nano-mechanics of thyroid tissues from different histo-pathologies. Coupled directly onto the conventional fine biopsy needle (25 Gauge), the smart-touch can be easily adapted to biomechanically evaluate thyroid lesions for risk of malignancy or aggressive cancers, and has potential for use in clinics in outpatient settings in future.

Previously, we demonstrated the ability of a piezoelectric force-sensing needle to differentiate solid and fluid-filled thyroid nodules[27] biomechanically. Significantly higher force variations (1-D force heterogeneity and stiffness heterogeneity) were noted in solid nodules compared to fluid nodules or regions corresponding to healthy thyroid tissue. However, these

observations were limited to ultrasound neck phantom observations. Employing next-generation needle sensor design in the current study, we introduce the prototype design for STFN mounted directly onto conventional needles used during FNAC. Using data obtained via STFN prototype, we show that thyroid lesions with varying fibrotic and malignant potential reveal discrete variations in tissue stiffness/stiffness heterogeneity, and correlate well with final histopathology data. Based on our findings, we believe that STFN provides a solid foundation for development of sensitive and low-cost tools that enable rapid and radiation-free stiffness heterogeneity-based characterization of malignant lesions in vivo, in thyroid and which is applicable to other soft-tissue tumors.

17.2 Bibliography

[1] L. Hegedus, "Clinical practice. The thyroid nodule," *N Engl J Med,* vol. 351, pp. 1764-71, Oct 21 2004.

[2] R. Siegel*, et al.*, "Cancer statistics, 2014," *CA Cancer J Clin,* vol. 64, pp. 9-29, Jan-Feb 2014.

[3] B. R. Haugen, "2015 American Thyroid Association Management Guidelines for Adult Patients with Thyroid Nodules and Differentiated Thyroid Cancer: What is new and what has changed?," *Cancer,* vol. 123, pp. 372-381, Feb 1 2017.

[4] R. Kulstad, "Do All Thyroid Nodules >4 Cm Need to Be Removed? An Evaluation of Thyroid Fine-Needle Aspiration Biopsy in Large Thyroid Nodules," *Endocr Pract,* vol. 22, pp. 791-8, Jul 2016.

[5] J. F. Silverman*, et al.*, "Fine-needle aspiration versus large-needle biopsy or cutting biopsy in evaluation of thyroid nodules," *Diagn Cytopathol,* vol. 2, pp. 25-30, Jan-Mar 1986.

[6] R. K. Jain*, et al.*, "The role of mechanical forces in tumor growth and therapy," *Annu Rev Biomed Eng,* vol. 16, pp. 321-46, Jul 11 2014.

[7] S. Suresh, "Biomechanics and biophysics of cancer cells," *Acta Biomater,* vol. 3, pp. 413-38, Jul 2007.

[8] D. Wirtz*, et al.*, "The physics of cancer: the role of physical interactions and mechanical forces in metastasis," *Nat Rev Cancer,* vol. 11, pp. 512-22, Jun 24 2011.

[9] R. Smith-Bindman*, et al.*, "Risk of thyroid cancer based on thyroid ultrasound imaging characteristics: results of a population-based study," *JAMA Intern Med,* vol. 173, pp. 1788-96, Oct 28 2013.

[10] D. G. Na*, et al.*, "Thyroid nodules with isolated macrocalcification: malignancy risk and diagnostic efficacy of fine-needle aspiration and core needle biopsy," *Ultrasonography,* vol. 35, pp. 212-9, Jul 2016.

[11] W. A. Berg*, et al.*, "Quantitative Maximum Shear-Wave Stiffness of Breast Masses as a Predictor of Histopathologic Severity," *AJR Am J Roentgenol,* vol. 205, pp. 448-55, Aug 2015.

[12] R. Guo*, et al.*, "Ultrasound Imaging Technologies for Breast Cancer Detection and Management: A Review," *Ultrasound Med Biol,* vol. 44, pp. 37-70, Jan 2018.

[13] J. Carlsen*, et al.*, "Ultrasound Elastography in Breast Cancer Diagnosis," *Ultraschall Med,* vol. 36, pp. 550-62; quiz 563-5, Dec 2015.

[14] S. H. Lee*, et al.*, "Differentiation of benign from malignant solid breast masses: comparison of two-dimensional and three-dimensional shear-wave elastography," *European Radiology,* vol. 23, pp. 1015-26, Apr 2013.

[15] J. H. Youk*, et al.*, "Comparison of strain and shear wave elastography for the differentiation of benign from malignant breast lesions, combined with B-mode ultrasonography: qualitative and quantitative assessments," *Ultrasound Med Biol,* vol. 40, pp. 2336-44, Oct 2014.

[16] Y. Jiao*, et al.*, "Shear wave elastography imaging for detecting malignant lesions of the liver: a systematic review and pooled meta-analysis," *Med Ultrason,* vol. 19, pp. 16-22, Jan 31 2017.

[17] M. M. Xu and A. Sethi, "Imaging of the Pancreas," *Gastroenterol Clin North Am,* vol. 45, pp. 101-16, Mar 2016.

[18] X. Hu, *et al.*, "Diagnostic potential of real-time elastography (RTE) and shear wave elastography (SWE) to differentiate benign and malignant thyroid nodules: A systematic review and meta-analysis," *Medicine (Baltimore),* vol. 96, p. e8282, Oct 2017.

[19] X. Yu, *et al.*, "Needle-shaped ultrathin piezoelectric microsystem for guided tissue targeting via mechanical sensing," *Nature Biomedical Engineering,* vol. 2, pp. 165-172, 2018/03/01 2018.

[20] P. Hansma, *et al.*, "The tissue diagnostic instrument," *Rev Sci Instrum,* vol. 80, p. 054303, May 2009.

[21] I. Levental, *et al.*, "A simple indentation device for measuring micrometer-scale tissue stiffness," *J Phys Condens Matter,* vol. 22, p. 194120, May 19 2010.

[22] N. Ragavendra, *et al.*, "In vivo analysis of fracture toughness of thyroid gland tumors," *J Biol Eng,* vol. 2, p. 12, 2008.

[23] J. Luo, *et al.*, "Risk of malignancy in thyroid nodules: predictive value of puncture feeling of grittiness in the process of fine-needle aspiration," *Sci Rep,* vol. 7, p. 13109, Oct 12 2017.

[24] V. K. Chivukula, *et al.*, "Alterations in cancer cell mechanical properties after fluid shear stress exposure: a micropipette aspiration study," *Cell Health Cytoskelet,* vol. 7, pp. 25-35, Jan 9 2015.

[25] S. E. Cross, *et al.*, "Nanomechanical analysis of cells from cancer patients," *Nat Nanotechnol,* vol. 2, pp. 780-3, Dec 2007.

[26] M. Plodinec, *et al.*, "The nanomechanical signature of breast cancer," *Nat Nanotechnol,* vol. 7, pp. 757-65, Nov 2012.

[27] D. Wickramaratne, *et al.*, "Fine Needle Elastography (FNE) device for biomechanically determining local variations of tissue mechanical properties," *J Biomech,* vol. 48, pp. 81-8, Jan 2 2015.

Chapter 18

STFN Design and Development

The STFN device was constructed using additive manufacturing technology (3D printing) to allow for inexpensive and flexible exploratory design. A lead zirconate titanate (PZT) ceramic piezo cylinder (0.125" (OD), 0.085" (ID), and 0.500" length) from Boston Piezo-Optics, Inc. served as a force transducer for measuring biomechanical properties. An ergonomic custom CAD designed (SolidWorks 2013) housing unit is prepared using a MakerBot 2 3D printer (Figure 18.1a-c). The housing design incorporated several cutouts sized for each device element with the appropriate dimensions. Double twined 25 AWG Lakeshore Teflon insulated copper wires were attached using conductive silver epoxy for all connections and electrically isolated throughout the holder. The printed parts were assembled using fast drying cyanoacrylate. Standard Becton Dickinson (BD) 25 Gauge 3.50" fine needle was attached to the piezo via a Luer lock as a measurement probe. Vibrational isolation was achieved by using a freestanding apparatus where all mechanical contact was pneumatically damped using an inexpensive custom vibrational liquid filter. Vibrational damping through liquid media produces a 3 dB filter within the low-frequency band <200 Hz. Measurement automation was controlled mechanically using a single axis Misumi LX26 actuator, where contact between the STFN device and actuator was damped using our vibrational filter. The experimental setup used a custom biocompatible sample holder alongside a compact analysis platform (as shown in Figure 19.1a).

18.1 Instrumentation

Measurements were taken using National Instruments USB-6259 data acquisition module routed from a Stanford Research Systems Low-Noise Current Amplifier. The mechanically

induced electric current from the PZT piezo was converted to a voltage signal via a charge amplifier and its time trace recorded. The force trace was calculated in real-time through standard d_{31} Piezo tube equation. Needle actuation was controlled through using a linear motion actuator. We calculated the position trace of the needle from the Musimi LX26 motor's known stepper size and rate. The optimum actuation speed was calibrated to 8 mm/sec to emulate clinical operation. Since needle and sample deformations during the operation were minimal, the force trace in combination with the position trace was converted from F(t) to F(x). All data were stored in an ASCII format and analyzed using LabView 2015 software.

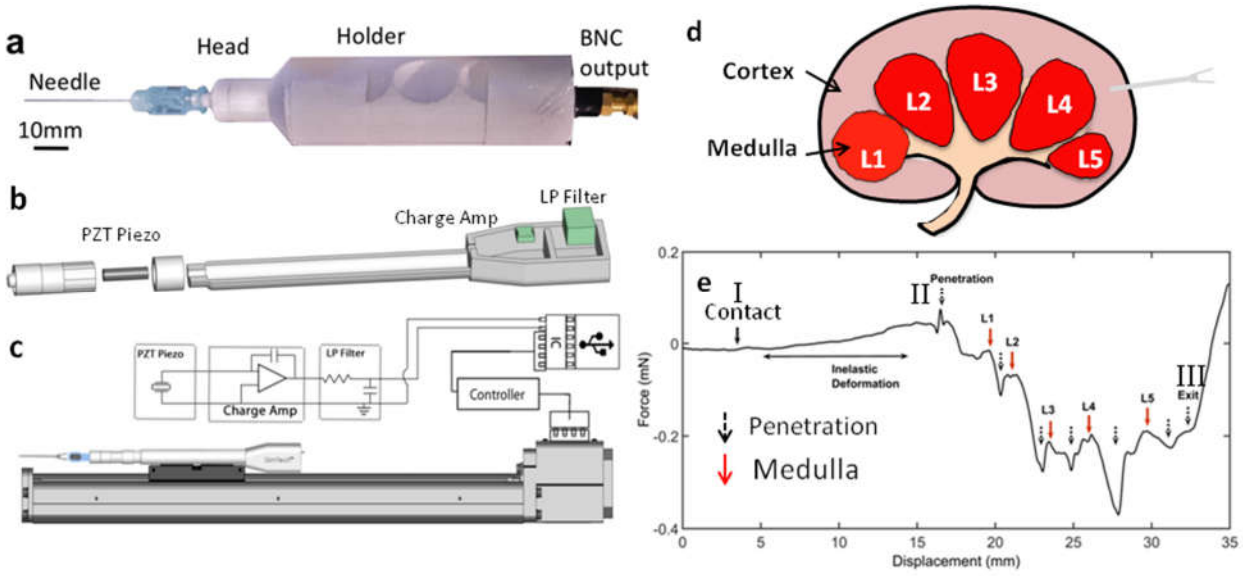

Figure 18.1 Experimental set-up for the smart-touch fine needle (STFN) a, Experimental set-up for the smart-touch fine needle (STFN) a, Optical image of the STFN device composed of a 25G fine needle, PLA polymer housing and connected to RG-58/U coaxial BNC cable. **b,** Design schematic of housing attaches the needle to piezoelectric tube transducer and piezo-response measured through 20 AWG twisted pair Cu wire. The twisted pair is frayed to connect to the BNC. **c,** An illustration shows the experimental connection diagram of STFN. **d,** Schematic diagram of a cross-section of porcine kidney samples showing fibrous capsule, cortex and medulla regions. **e,** An example of force versus needle displacement profile from STFN penetrating through the tubules of the kidney sample. Before the estimated point of contact (marked with a solid black arrow) between the needle and kidney tissue, the force observed was minimal. After the point of contact (solid black arrow), there is an elastic deformation due to fibrous capsule until an abrupt Hertzian penetration (broken black arrow) occurs. Subsequent deformation peaks occur (labeled L1 to 5) before full penetration at the point marked as exit (broken black arrow).

We chose gravitational force loading because of the elegant simplicity of the approach. Masses between m = 25 g and m = 55 g were weighed using a digital balance, and the resulting gravitational force, F_g, was computed using $F_g = m\ g$, where g = 9.81 m/s^2 is the gravitational constant. The FNE device was mounted vertically and then smoothly loaded and unloaded with the calibrated masses. The change in piezoelectric charge on gravitational force loading was measured for each of the calibrated masses in Figure 18.2. Force (mg) vs. piezoelectric charge was plotted and first order polynomial (linear) fit slope was taken as the calibration constant (N/C). Force calibration measurements were done at a preamp gain of 2 nA/V and at band pass filter 0.03 Hz-100 kHz. After the calibration procedure, the calibrated masses were again loaded, and the force measured by the FNE device was verified to be in agreement with the force computed via $F_g = m\ g$.

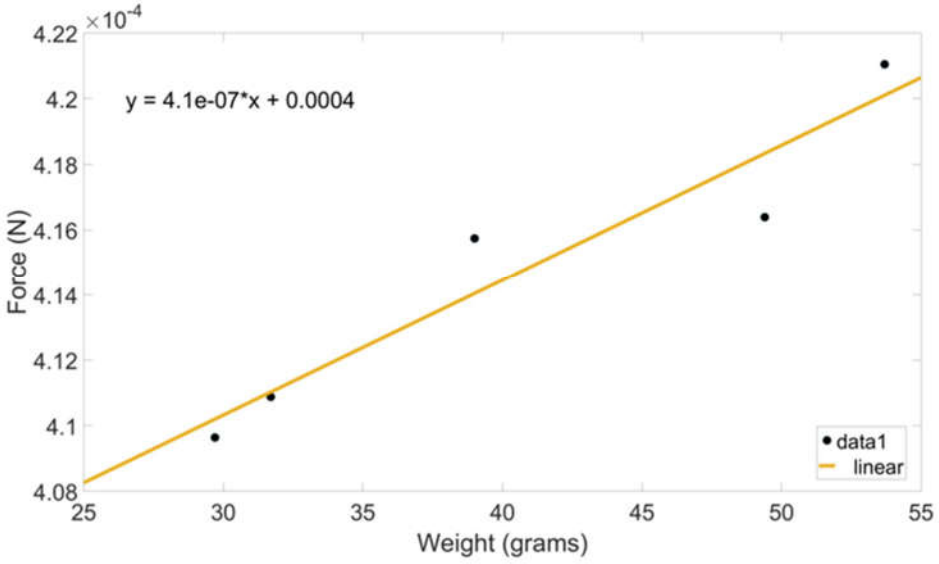

Figure 18.2. Piezoelectric Coefficient Calibration. Calibration of the piezoelectric element was performed using standardized weights loaded on a custom built apparatus to determine the d_{31} coefficient. A statistical number of measurements were taken and a least square linear regression algorithm was used to determine the d_{31} coefficient (4.1 x 10^{-7} C / N) for the device.

18.2 Quantitative control experiment of ex vivo tissues

To better recapitulate the native tissue microenvironments within thyroid samples, here, we chose first to calibrate the device while including the effects of biological environments via an ex vivo animal tissue model. A control experiment using porcine kidney samples aided to develop a working model of spatial variations versus biomechanical variations in different optically identifiable regimes. We obtained a preliminary characterization of the axial forces that arise during needle insertion into a freshly excised porcine kidney, in terms of needle-tissue penetration, insertion peak force and apparent stiffness, and to attribute observed force peaks to specific tissue structure components.

Excised kidney organs were procured from traditional vendors and prepared using the standard procedures highlighted in the Standard Operation section while omitting any clinical reference. Figure 18.1d shows a schematic overview of the kidney, where biologically relevant features are labeled. A simplified structure of the organ comprises of medulla lobes (1-2 mm), various blood vessels (0.5 -1 mm), and connective tissues within the renal region (>5 mm). Automation and experimental parameters for needle-tissue interactions were chosen to measure the biomechanical characteristics of the medulla and blood vessels due to their similarity in scale to typical human tumor nodules. Nominal parameters of needle speed and needle type (diameter expressed in wire gauge G; length, and shape) were chosen to simulate clinical methods typical for standard fine needle biopsy of thyroid lesions, and to minimize tissue displacement [1].

In a typical force-displacement profile (Figure 18.1e), an initial approach of the needle towards the sample is characterized by a zero load force on the needle traversing through the free air before the estimated point of contact. The region following contact (I), exhibits positive force on the needle with initial elastic deformation (I, II) as modeled by the Hertzian formulation[2]. Later, a penetrative peak (broken arrow, Figure 18.1e) was observed with characteristic spring-

like compression and decompression force loads (II, III), shown as a relatively negative peak followed by a relatively positive peak. The spring-like cortex region between penetration and L1 show uniform negative (repulsive) response, except for the transient response due to spring relaxation. Subsequent peaks labeled L1-L5 were positive and attractive areas presumably corresponding to the vesicle-like structure of the medulla. The negative regions between peaks likely corresponded to hard repulsive tissue such as the major and minor calyx. An atypical hard region between L4-L5 corresponded to a region of calcified vessels, verified visually in a subsequent dissection (Figure 18.3) of the specimen. We estimated the dimensions of the medulla lobe by calculating the width from the full-width-half-maximum of each peak labeled L1-L5. The number of force peaks depends of the tissue structures that are encountered. Visual inspection of the sample reveals the width of the peaks to be ~2 mm which corroborate with the predicted literature value dimensions for kidney tubules. Secondary peaks found in each lobe were attributed to connecting blood vessels and similarly analyzed. The calculated width was ~1.87 mm and ~0.53 mm for the medulla lobe and blood vessels respectively. Based on anatomical considerations (Figure 18.1d), results obtained from explanted samples of kidney in a non-diseased state, accurately predicted the expected kidney architecture and biomechanical properties of the different regions, corroborating with literature values within < 5% [3]. The developed analytical model for classifying biomechanical responses based on the identification of characteristic points on the needle force-displacement curves was employed for subsequent ex vivo patient thyroid sample analysis.

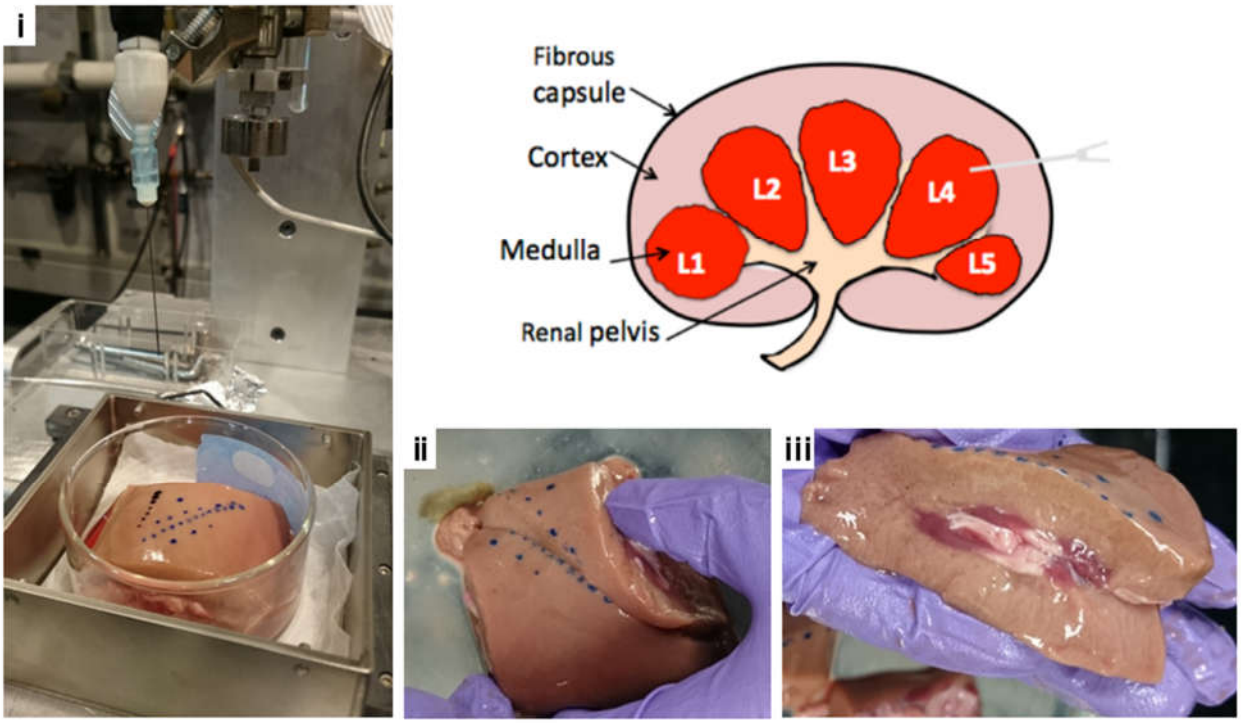

Figure 18.3. Porcine Kidney Dissection and Analysis. A post-measurement dissection of the porcine kidney sample was conducted to elucidate the mechanical profile of the porcine kidney. Measured areas are marked with blue ink (**i**) and conducted in ascending order. Dissection normal to the penetration (**ii**) reveals a hard renal structure (**iii**) near the incident of penetration and exit**.**

18.3 Bibliography

[1] D. J. van Gerwen*, et al.*, "Needle-tissue interaction forces--a survey of experimental data," *Med Eng Phys,* vol. 34, pp. 665-80, Jul 2012.

[2] A. M. Okamura*, et al.*, "Force modeling for needle insertion into soft tissue," *IEEE Trans Biomed Eng,* vol. 51, pp. 1707-16, Oct 2004.

[3] D. J. van Gerwen*, et al.*, "Measurement and stochastic modeling of kidney puncture forces," *Ann Biomed Eng,* vol. 42, pp. 685-95, Mar 2014.

Chapter 19

Protocol development and Measurement ex vivo patient thyroids

19.1 Ex vivo thyroid sample procurement

We followed a standard procedural protocol for every attained thyroid sample and measurement. Explanted human thyroids samples were procured from the Ronald Reagan UCLA Medical Pathology Department in accordance with the IRB protocol.

19.2 Sample Mounting

First, the possible areas of interests for biomechanical profiling with the STFN were identified, in consultation with the attending physician, for each specimen studied. The initial diagnosis and relevant medical data were kept in a blinded secured database for reference. Measurements were taken approximately 1 hour after surgical removal while held in an environmentally controlled storage unit at 4 C to prevent sample degradation as reported previously[1]. Typically, thyroid samples were then placed on our custom sample holder (Figure 19.1) where the sample was mapped into topographic sections using the holder and a mesh grid. Assigned reference ID and a digitally scanned image for each sample were recorded in a secured database for future reference. The sample holder with the thyroid specimen was then placed in a normal position with the path of the STFN measurement apparatus, allowing for approximately 1 cm of free translation before contact of the needle with the sample. The initial 1 cm data was used for zero-force calibration and determining signal-to-noise ratio.

For sample orientation, precisely oriented maps were prepared for each specimen to indicate the area(s) investigated for biomechanical analysis (Figure 19.1b). We used color ink on the specimen (Figure 19.2c) to highlight the specific area(s) that have been measured/sampled, as follows: Green (Area 1) - Nodule of primary interest (as defined clinically, main factor for thyroidectomy); Red (Area 2) – Non-diseased area immediately adjacent to the main nodule (area 1); Black (Area 3) – Non-diseased area at least 0.5 cm away from the main nodule (area 1); Yellow (Area 4) – Contra lateral thyroid without disease; Purple (Area 5) – Other nodule, if present. No more than five nodules/areas were analyzed for each specimen. Tissue sections were taken from the corresponding areas that have been measured and indicated as such on the gross description. STFN data analysis was performed independently without knowledge of histological diagnoses.

19.3 Histology Analysis

After STFN measurements, inked samples were formalin-fixed and paraffin-embedded according to standard histological procedures. The subsequent histo-pathological examination included assessing the type of lesion and standard histo-pathological markers (extent of tumor infiltration, fibrosis, necrosis, and lymphocytic infiltration).

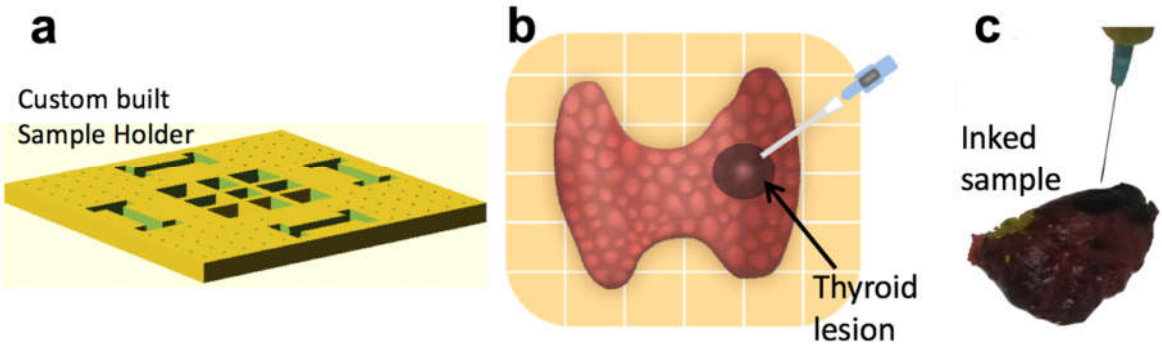

Figure 19.1 Experimental workflow during the typical STFN measurements and distribution of tissue stiffness heterogeneity observed for thyroid carcinoma and the healthy thyroid. a-b, Following a standard operating procedure, samples were first prepared by attachment and orientation into quadrants, using biocompatible sample holders with calibrated grids as illustrated schematically. **c,** An inked patient sample measured using STFN. Samples were later processed for standard tissue histology.

19.4 Identification of characteristic points on STFN based needle force-displacement curves

First, we measured the non-nodule regions of the thyroid tissue specimens as determined by haptic palpations. Real-time force versus needle displacement data from the STFN was observed and analyzed to determine the validity of each measurement (Figure 19.2a). We developed standard direct-indicators of successful characterization through multiple heuristic trials. The Hertzian deformation response (Figure 19.2a, red and black) indicated penetration of the needle into the tissue. Simultaneously the STFN response in stiffness deflection (Figure 19.2a, red and black) characterized tissue granularity, indicating the presence of nodules or other extracellular material. Each measurement was repeated 5-10 times on different parts of the same nodule for statistical convergence. Subsequent STFN measurements targeted other areas of interests such as tumor nodules, cystic nodules, and lymph nodes following identical procedures. We inked each measured area for subsequent histological assessment of the thyroid tissue

specimens. The order of the procedure was chosen to prevent region-to-region cross-contamination in histological studies.

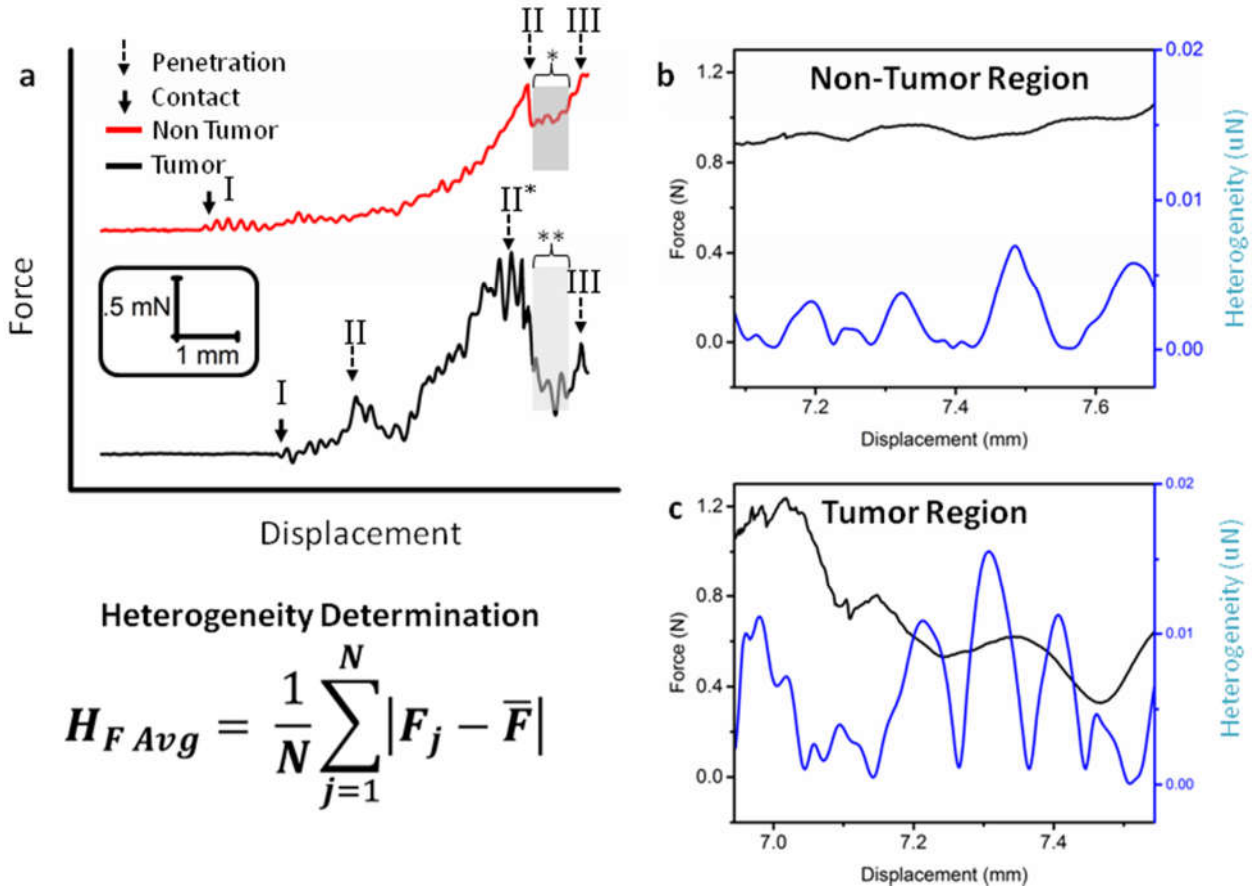

Figure 19.2 Method for determining the presence and location of the nodules in ex vivo human thyroid samples- based on needle biomechanical response. a i, Shows the characteristic STFN response for the initial point of contact between the needle and the tissue sample (solid black arrows), followed by penetration (marked by broken arrows) into non-tumor and tumor tissues shown in red and black curves respectively. Malignant specimens (black) show several broken arrows corresponding to secondary interfaces caused by tumors as corroborated by histology. Within the identified regions of interest (marked with * and ** for non-tumor and tumor samples respectively), heterogeneity of tissue stiffness is analyzed based on Equation 1 given in **a (ii). b-c,** Show corresponding force-displacement curves from ROI (for non-tumor and tumor samples respectively). Representative ex vivo measurements of human thyroid following SOP, show distinct responses between malignant and benign samples.

19.5 Analysis of tissue stiffness and stiffness heterogeneity in patient thyroids

Using STFN prototype, we analyzed the tissue stiffness and stiffness heterogeneity of ex vivo patient thyroid samples including various thyroid histo-pathologies. Our goal was to quantify any significant differences in the biomechanical profiles for papillary carcinoma, cystic carcinoma, aggressive tall-cell carcinoma, and Hashimoto syndrome carcinoma compared to

non-tumor tissue thyroid tissue and adenomatoid cyst-like nodules. Our findings provide the initial steps towards a mechanoprofile catalog of variant carcinoma based on localized tissue biomechanics. Table 19.1 shows patient characteristics from all ex vivo thyroid samples analyzed in the current study. All measurements were done on site to simulate the clinical use of the device and reduce possible sources of contamination. Figure 19.2a shows typical force versus displacement profiles obtained using STFN.

19.5.1 Determining the presence and location of the nodules in ex vivo thyroid- based on needle biomechanical response: Similar to our control experiment (Figure 18.1e), the initial approach regions prior to estimated contact between the needle and the tissue show a near-zero loading force (Figure 19.2a) whereas the contact regions show typical Hertzian behavior. The point of initial contact between the needle tip and the sample is marked with solid black arrow. As seen in Figure 19.2a, the length of the Hertzian region inherently differs from sample-to-sample, due to variations in size of the thyroid samples. However, our analysis is thyroid size independent, as we normalize the data size in our catalog. The points of needle penetration (broken arrow, Figure 19.2a) at differing interfaces exhibit spring-like behavior and high stiffness. In case of a representative benign sample (Figure 19.2a, red), only a single penetration event is noted (broken arrow Figure 19.2a), followed by translation into a relatively homogenous non-nodule region. In contrast, the representative malignant sample shows three such events (Figure 19.2a, black). The initial penetration corresponds to the transition from non-contact to initial contact with the thyroid tissue, while the subsequent penetration peaks correspond to the interface from non-nodule to nodule and out of the nodule, as the needle traverses through the specimen. A qualitative analysis of the real-time force versus needle displacement profiles obtained via STFN readily distinguished between benign and malignant thyroids (Figure 19.2a).

Needle-tissue penetration points were readily identifiable for all samples and were used to validate the presence or absence of nodules, as well as their positions. Further analysis on localized region-of-interest (ROI) determined the intrinsic biomechanical properties of malignant (Figure 19.2a*; 19.2b) and benign (Fig 19.2a**; 19.2c) human thyroids. Equally binned subsections of data from Fig 19.2a are selected, representing non-tumor and tumor tissue labeled with solid arrows. Heterogeneity provides a quantitative description to calculate their force heterogeneity. For user validation, the heterogeneity equation is truncated to analyze 40 um windows and applied as a sliding function across the ROI in Figure 19.2b-c. Our classification analysis uses the full 350 um range of the sectioned data to render quantitative insight presented later in Figure 19.4.

For quantitative analysis of biomechanical variations between malignant and benign human thyroids, we measured stiffness heterogeneity as shown in Figure 19.2b-c. The force heterogeneity profiles of the benign case show several areas of relatively high heterogeneity (illustrated in the representative profile shown in Figure 19.2a, red). This characteristic was determined to be the typical composition of normal thyroid tissue due to normal variation in the density of hormone glands and blood vessels. In contrast, areas displaying about twice the amplitude in heterogeneity characterized the malignant case (in Figure 19.2a, black). We attribute the increase in heterogeneity to the likelihood of tissue fibrosis and frequent calcifications in thyroid tissues, and which corroborate with histological analysis of the samples used in our study (Figure 19.3). Specifically, to examine differences between benign and malignant thyroid lesions, we used a non-parametric Wilcoxon rank sum test to compare the median tissue stiffness and stiffness heterogeneity differences measured between the two groups, with $\alpha = 0.05$. Our results suggest large and statistically significant differences between median

stiffness values obtained for benign (0.05 ± .02 mN/mm) versus malignant thyroid lesions (0.18 ± 0.15 mN/mm) ($P = 1.55x10^{-4}$) in 12 patient nodules measured. Furthermore, stiffness heterogeneity was also found to be statistically higher in malignant compared to benign thyroid lesions (3.23 ± 2.49 µN**;** 1.41 ± 0.43 µN; $P = 2.22 \times 10^{-5}$).

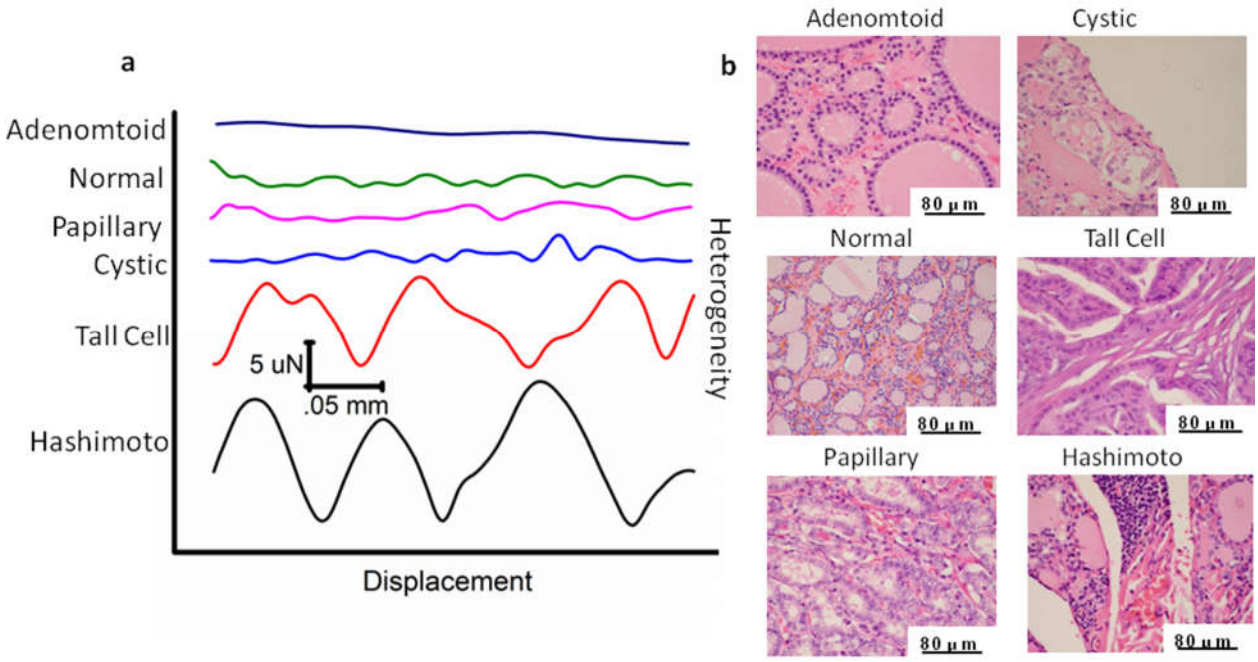

Figure 19.3. Heterogeneity Increase due to Fibrosis/Calcifications. Ex vivo STFN measurements of human thyroids showing the distribution of tissue heterogeneity responses **a** observed for thyroid carcinoma and healthy thyroids. Increased tissue stiffness heterogeneity observed for malignant thyroid samples compared to non-tumor thyroid samples, corresponds well with malignant tissue histology, shown in **b** displaying increased stroma density shows histology for a non-tumor sample with little intervening stroma for comparison.

19.6 Biomechanical identification of variant human thyroid carcinoma

Next, we analyzed STFN based stiffness and stiffness heterogeneity measured in several thyroid carcinomas prevalent in different populations. A statistical summary of our findings is presented in Figure 19.4 (a, b) indicating stiffness heterogeneity (µN) and stiffness (mN/mm) respectively, evaluated for multiple non-nodule and nodule regions from all thirteen patient samples included in our study. These included the papillary carcinoma, cystic carcinoma,

aggressive tall-cell carcinoma, Hashimoto syndrome carcinoma, and adenomatoid (Table 19.1). Information on the specific variant cell-type was acquired using histological reports and cross-examined with the post-analysis results from STFN measurements.

Table 19.2 Statistical Analysis of Tumor Variants. STFN data for 76 measurements are statistically analyzed according to their corresponding histology reports. Variants of benign samples (Adenomtoid and Normal) show similar qualities while malignant samples (others) show drastic variability. Classification of each variant can be observed through their hetergeneity response using principle component analysis.

No	Age/sex	Clinical History	Cytological/Histology
1	45/M	Papillary Thyroid Carcinoma 2.6 cm tumor	Positive for metastatic malignant cells
2	52/M	Papillary Thyroid Carcinoma 1.2 cm pT3 pN0	Positive for metastatic malignant cells
3	64/M	Cystic Papillary Thyroid Carcinoma 0.8 cm	Positive for metastatic malignant cells
4	47/F	Hyperthyroidism and Thyroid Goiter	Negative for malignancy, cyst lined follicular cells
5	73/M	Papillary Thyroid Carcinoma 1.7 cm pT3 N1b	Positive for metastatic malignant cells
6	29/F	Hashimoto Papillary Thyroid Carcinoma 1.5 cm pT3 N1a	Positive for metastatic malignant cells
7	64/M	Cystic Thyroid Goiter with Gout	Negative for malignancy, multinodular goiter
8	23/F	Hyperparathyroidism post parathyroidectomy	Positive for metastatic malignant tall cells, papillary thyroid microcarcinoma pT3Nx
9	33/M	Papillary Thyroid Carcinoma 1.1 cm	Positive for metastatic malignant tall cells
10	68/M	Papillary Thyroid Carcinoma 4.5 cm	Positive for metastatic malignant cells
11	49/F	Papillary Thyroid Carcinoma 1.6 cm	Positive for metastatic malignant cells
12	69/M	Hashimoto Papillary Thyroid Carcinoma 0.2 cm	Positive for metastatic malignant cells

Compared to normal thyroid tissue (1.39 ± .47 μN, 31 regions measured from patients with non-disease), adenomatoid samples showed low heterogeneity (1.34 ± .28 μN; n= 9). Cystic carcinomas were identifiable through characteristically low stiffness and heterogeneity (0.79 ± .05 μN; n = 5). In contrast, aggressive tall cell carcinoma showed significantly higher heterogeneity (6.29 ± 1.10 μN). A similar profile is shown for Hashimoto (5.75 ± 0.81 μN) syndrome in heterogeneity but can be differentiated using stiffness.

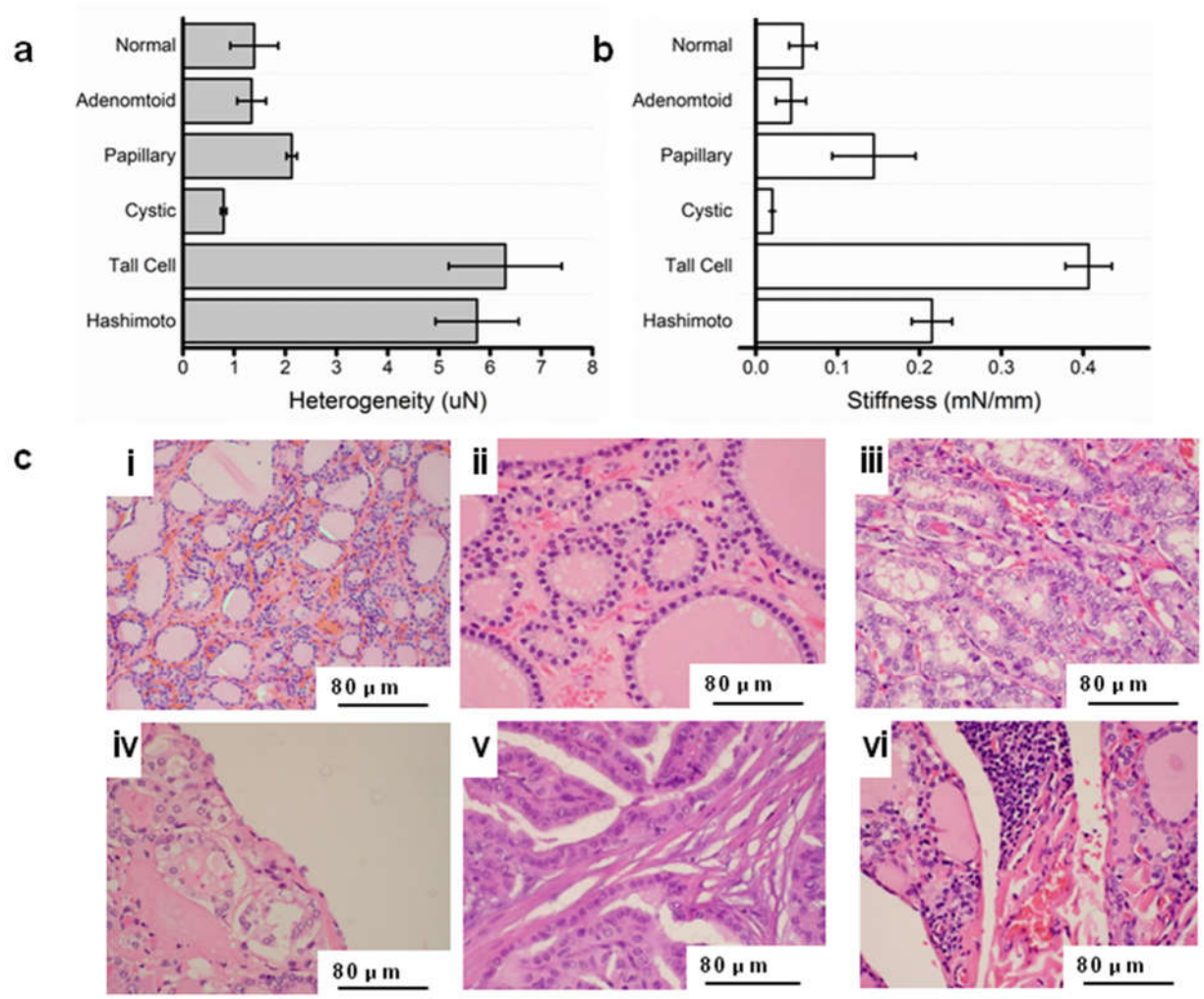

Figure 19.4 STFN based quantitative biomechanical analysis of patient thyroid tissue samples with corresponding representative histology. a, Tissue stiffness heterogeneity (uM) and **b,** tissue stiffness (mN/mm) evaluated for all 13 patient samples studied. Data are stratified based on tissue variant types. Variants of benign thyroid samples (normal and adenomatoid) show similar biomechanical characteristics compared to malignant samples (others). **c,** Histology data corresponding to each thyroid tissue variant represent normal, adenomatoid, papillary, cystic, tall cell and Hashimoto disease respectively (from **i-vi**).

19.6.1 Correlation between thyroid histology and biomechanical characteristics:

Corresponding structural variations within the different thyroid tissue histology were correlated with STFN biomechanical analysis for different thyroid tissue variants (normal, adenomatoid, papillary, cystic, tall cell or Hashimoto disease) are shown in Figure 19.4c. Healthy thyroid tissue displayed follicular cells uniformly distributed with purple epithelial cells traversed within the collagen fibers (as represented in Figure 19.4c-i). Both the collagen fibers and follicular cells stained pink, but the cells can be readily identified- forming rotund colloids and surrounded by a

layer of epithelial cells. Adenomatoid samples consisted of the same structure as a healthy thyroid except for follicular cells consistently forming enlarged colloids. In contrast, papillary carcinoma samples show uncontrolled growth of epithelial cells (Figure 19.4c-ii). In case of papillary carcinoma, the histological images represent cells undergoing replication with the presence of enlarged nuclei and nucleoli. The absence of follicular colloids and increased presence of collagen fibers to support growing epithelial are vital features of the ubiquitous papillary carcinoma (Figure 19.4c-iii). Cystic carcinoma samples are difficult to image as the broken cyst tend to only create large voids in the sample histological images (Figure 19.4c-iv). The high abundance of cell nucleoli is highly indicative of the presence of carcinoma. In the case of tall-cell carcinoma (Figure 19.4c-v), the majority of epithelial cells are elongated allowing for rapid progression throughout the thyroid and drastically increases the number of collagen fibers. Finally, the rare case of Hashimoto carcinoma shown in Figure 19.4c-vi depicts a very staggered and heterogeneous structure in the sample but otherwise similar to papillary carcinoma.

As expected, compared to normal thyroid samples (.06 ± 0.02 mN/mm), adenomatoid samples showed low stiffness (.04 mN/mm) likely due to the enlarged hormone glands dominating the ROI analysis and a monotonically decreasing trend due to high liquid content. Cystic carcinomas were identifiable through characteristically low stiffness and heterogeneity (.02 ± 0.00 mN/mm) likely due to a distributed structure of fluid nodules and the reduction of transport vessels upon needle insertion into the cyst. Conversely, aggressive tall cell carcinoma showed significantly higher heterogeneity (6.30 ± 1.10 μN) due to increased fibrosis and calcification from rapid metastasis. A similar profile is shown for Hashimoto syndrome (5.75 ± 0.81 μN) in heterogeneity but can be differentiated using stiffness (Hashimoto .22 ± 0.02 mN/mm, Tall Cell 0.41 ± 0.03 mN/mm) due to reduced development of fibrosis while high

heterogeneity from Hashimoto syndrome's inhomogeneous cell distribution. Overall, despite several confounding factors including sex, age, development, and the state of health of their thyroids, STFN measurements of stiffness and stiffness heterogeneity readily identified malignant cases from benign cases based on either extremely high or low heterogeneity and stiffness (Figure 19.5).

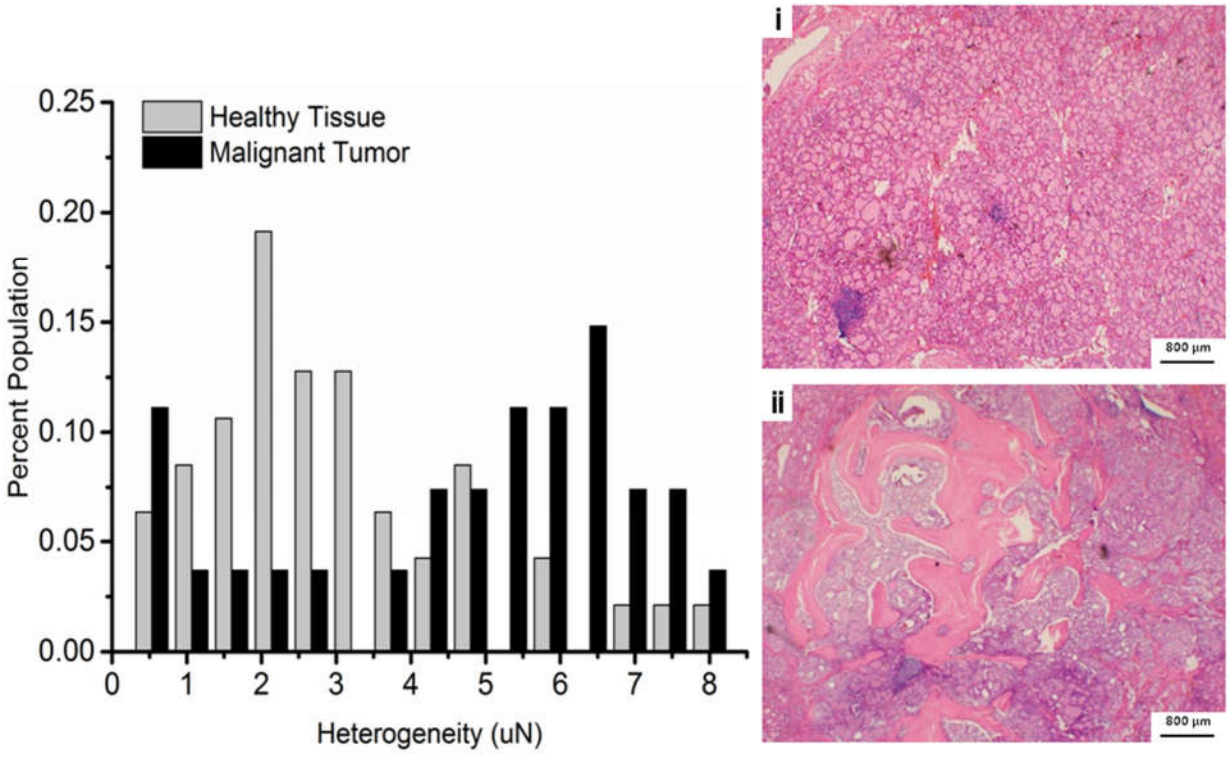

Figure 19.5. Varied STFN Responses of Thyroid Carcinoma and Healthy Thyroid. Representative ex vivo measurements of human thyroid show clear distinctive response between malignant and benign samples. Benign measurements from adenomtoid and normal (healthy) thyroid depict low heterogeneity within the tissue **i**, where the heterogeneity is measured at a random location on the tissue. Measurements on malignant samples (Papillary to Hashimoto) depict high heterogeneity likely due to calcification around the nodule **ii**.

Moreover, the heterogeneity of healthy and adenomatoid samples was observed to differ by a factor of 2 from each of the malignant cases. Distinguishing between the variant types of carcinoma also show similar ratios between each type but requires the auxiliary use of stiffness for some degenerate cases such as tall-cell and Hashimoto, where their heterogeneity profiles are

similar. Using heterogeneity and stiffness in concert, the analysis yielded stiffness with differences by a factor of two thereby enabling biomechanics based identification between the two cases. Our study provides the direct evidence for diagnostic potential for fine needle force sensing approaches to obtain quantitative biomechanical analysis of tissues. Our work provides direct evidence for the applicability of tissue biomechanics in assessing benign versus malignant thyroid lesions. More importantly, it also indicates the usefulness of biomechanical analysis in evaluating the aggressiveness of malignant lesions as a complementary approach for early diagnosis. STFN based stiffness and/or heterogeneity together reliably identified the different variants using heterogeneity (Figure 19.5b) as validated by gold standard histological findings.

19.7 Conclusions and outlook

Biomechanics plays an important role in normal and pathological tissue function. Tissue stiffness has been studied extensively within the field of cancer for diagnostic purposes using various imaging modalities. However, none of the currently available imaging modalities or biomechanical approach allows depth-independent yet direct quantitative assessment of biomechanical variations within the tissue microenvironments for early detection and management of thyroid cancers. Our ex vivo thyroid study illustrates the capabilities of STFN as a mechano-profiling tool for tissue diagnosis. STFN provides an exclusive and novel approach to assess localized high resolution (cellular level) and quantitative biomechanical variations in thyroid tissues. The findings presented in the current ex vivo thyroid study, suggest the high potential for the STFN approach to be translated into an in vivo diagnostic device. Despite limited patient population size, the results provide a solid foundation for further diagnostic assessment of quantitative tissue biomechanics in vivo to evaluate the risk of malignancy in

thyroid lesions in a larger validation study in future. The technique can also be applied to lung, liver, pancreatic, or prostate cancer. This label-free technique enables complementary tumor tissue sampling required for genomic profiling and treatment planning, as needed. As a hand-held, low cost technology, STFN could be ideal for diagnostic screening of solid tumors in medically underserved communities in USA and low resource settings worldwide, with minimal or no access to pathology labs or experts.

19.8 Bibliography

[1] M. Plodinec*, et al.*, "The nanomechanical signature of breast cancer," *Nat Nanotechnol,* vol. 7, pp. 757-65, Nov 2012.

Chapter 20

Final Remarks

Implementation of nanotechnological techniques towards neuromorphic devices and bioinformatics provided novel platforms in “artificial life”. Although a somewhat maniacal term, the concept of “artificial life” is a simple extension of machine learning. While machine learning attempts to biomimetically achieve information processing, artificial life applies biological models towards non-biological physical systems[1-2]. Directed research in artificial life adopts methodologies similar to an evolutionary process where problems are posed by setting evolutionary constraints rather than using a wholly reductionist physical model. Applications of artificial life typically utilizes machine learning algorithms to classify behaviors and control parameters for material design of self-assembly [3-4], inception of mathematical [5], or linguistics[6]. The research I completed during my doctorate program inevitably converged unto this ubiquitous concept and developed into a concept our collaborators currently refer to as “thermodynamic computing.”

The concept of thermodynamic computing was conceived with close collaboration with Dr. Todd Hylton (University of California, San Diego), Dr. Stanley Williams (Hewlett-Packard Labs), my advisor (Dr. James K. Gimzewski), and my research group (Gimzewski Lab) [7]. The concept stems from the application of machine learning paradigms towards physical systems to facilitate material manipulation through transduction of information directly into the system. Similar to artificial life, thermodynamic computing constrains a physical system to pose a problem. A simple example is the travelling salesman problem, where, given a list of cities, the

salesman attempts to find the shortest possible route between each city and returns to their origin. Here the problem may be posed as a circuit by constraining impedance values to represent the intercity distance while electrical nodes represent the city identification. Application of a bias voltage at a specific node poses a specific iteration of the problem and measurement of the electric current at various nodes solves the problem. Although the solution is realizable as a digital algorithm, a similar solution can be achieved using non-electronic systems such as microfluidics, DNA transcription, or quantum entanglement. The process yields a material encoded with a simple algorithm represented by channels, base pairings, or triplet states using the previous examples. Similarly, a problem may be posed to reduce traffic flow, control gene expression, or excite specific energy states provided environmental forces constrain the system to approach those solution trajectories.

Investigations in this dissertation are preliminary results towards realization of thermodynamic computing, where we have designed systems that physically deform or adapt to environmental constraints and developed the mathematical axioms to determine their trajectories. Specifically: The relationship between the dynamical properties of a complex system and its computational capabilities and characteristics; Control parameters for computation dynamics which emerge in macroscopic tools – as detailed within Chapter 2. In addition to these very preliminary results, artificial life algorithms [5] enable a generalized criteria to determine the above points for a novel scientific method.

20.1 Bibliography

[1] C. G. Langton, "Computation at the Edge of Chaos: Phase Transitions and Emergent Computation," *Physica D,* vol. 42, pp. 12-37, 1990.

[2] C. G. Langton, *Artificial Life: Proceedings of an Interdisciplinary Workshop on the Synthesis and Simulation of Living Systems*. Boston, MA: Addison-Wesley Longman Publishing Co., Inc., 1989.

[3] E. B. D. Long, and L. Cronin, "Polyoxometalate clusters, nanostructures and materials: From self assembly to designer materials and devices," *Chem. Soc. Rev.,* vol. 36, 2007.

[4] J. Y. H. N. Miras, D. Long, and L. Cronin, "Engineering polyoxometalates with emergent properties," *Chem. Soc. Rev.,* vol. 41, 2012.

[5] J. l. L. a. K. O. Stanley, "Exploiting Open-Endedness to Solve Problems Through the Search for Novelty," in *Eleventh International Conference on Artificial Life (ALIFE XI)*, Cambridge, MA, 2008.

[6] P. D. T. a. M. L. Littman, "Unsupervised Learning of Semantic Orientation from a Hundred-Billion-Word Corpus," *arXiv,* 2003.

[7] e. a. T. Conte., "Thermodynamic Computing," Computing Community Consortium 2019.